WEAR BEHAVIOR OF SPARK PLASMA SINTERED NANOSTRUCTURED MODIFIED 9Cr-1Mo STEEL

By

ADITYA D. DEKHANE

Bachelor of Mechanical Engineering

Pune University

Pune, Maharashtra

2010

Submitted to the Faculty of the
Graduate College of the
Oklahoma State University
in partial fulfillment of
the requirements for
the Degree of
MASTER OF SCIENCE
July, 2013

WEAR BEHAVIOR OF SPARK PLASMA SINTERED NANOSTRUCTURED MODIFIED 9Cr-1Mo STEEL

Thesis Approved:

Dr. Sandip P. Harimkar

Thesis Adviser

Dr. Kaan Kalkan

Dr. Raman P. Singh

ACKNOWLEDGEMENTS

I would like to thank my advisor Dr. Sandip P. Harimkar for his valuable guidance and directions that brought the best out of me. His positive attitude and motivation since two years have made me capable to stand here. I would like to thank Dr. Kaan Kalkan for being on my thesis committee. I appreciate his continuous motivation, support, and patience towards me. I thank Dr. Raman P. Singh for being on my committee and spending his valuable time. I wish to extend my regards to Ms. Lindsey Clark for helping me correct my thesis report.

I can't imagine myself here without the endless support and encouragement of my Mother Mrs. Charusheela Dekhane and the blessings of my Father Mr. Deepak Dekhane. This work is dedicated to my parents, dear Sister Ruchita, and my Grandmother Mrs. Rajani Dekhane. I want to express my gratitude towards my dearest friend Pranita Patil, Sisters Akshaya Satpute, Garima Sahney, and my Brother Vishal Bhatewara, for all the care and help that made my dream come true. I can't imagine a single odd in my life without them. This achievement wouldn't have been possible without the unconditional support of my friend Priti Kulkarni. I am privileged to have her encouragement during my difficult days. I am thankful to Ashish Singh and Amir Alavi for their undying help and support for the past 1.5 years. I am also grateful Farhad, Redwan, Nidul, Govind and my all research group for guiding me towards my aim. I am thankful to

Swanand, Siddharth, Arjun, Kunal, Dhanashree, Vrushali, and Snehal for making my life great for the past 2 years.

Name: ADITYA DEKHANE

Date of Degree: JULY, 2013

Title of Study: WEAR BEHAVIOR OF SPARK PLASMA SINTERED NANOSTRUCTURED MODIFIED 9Cr-1Mo STEEL

Major Field: MECHANICAL ENGINEERING

Abstract:

Ferritic-martensitic (FM) steels are well known for the combination of properties such as high strength and good ductility. Modified 9Cr-1Mo is a popular FM steel widely used as a high temperature (250-400ºC) tubing material in power generation industry. This modified 9Cr-1Mo steel can be effectively used as a material for rings and races of hybrid bearings operating at 350-500ºC. Refining the grain size to nanometer scale substantially improves the mechanical properties of steel. The nanostructured modified 9Cr-1Mo steel is expected to retain high hardness and wear resistance at elevated temperatures. In this work nanostructured modified 9Cr-1Mo steel is processed by spark plasma sintering of nanocrystalline steel powder. The nanocrystalline powder is produced by ball milling of as-received modified 9Cr-1Mo steel plate. A detailed x-ray diffraction analysis of a ball milled powder is performed to measure the crystallite size. The powder is spark plasma sintered at 500ºC, 800ºC and 1100ºC for 5 min. and 10 min. holding time.

The relative density more than 97% and the grain size < 1 μm are observed for the samples sintered at 800 and 1100ºC temperature. An increase of about 200% in microhardness is achieved for the sample sintered at 1100ºC as compared to the as-received modified 9Cr-1Mo steel plate. A systematic wear analysis of the sintered samples and as-received plate is performed with alumina and silicon nitride balls. A detailed microscopic analysis of the wear mechanisms is performed. The order of magnitude lower wear rate is observed in the samples sintered at 800 and 1100ºC as compared to as-received plate. The improvement in wear behavior can be attributed to the reduction in grain size of the sintered samples.

TABLE OF CONTENTS

Chapter Page

Chapter Page

LIST OF TABLES

LIST OF FIGURES

CHAPTER I

INTRODUCTION

1.1 Alloy steels and applications

For centuries, steel has been known for combination of properties such as high strength, good ductility, and remarkable toughness. Alloying plain carbon steels with Cr, Mo, and V make them corrosion and wear resistant. Alloy steels possess high temperature strength as well as creep resistance which make it a preferred choice for structural materials. Mechanical as well as wear properties of alloy steels can be substantially improved by refining the grain size to nano-meter length scale. This improvement is expected to raise the existing working temperature and strength limits and will broaden the application window of the alloy steels. In this chapter, the applications of nanostructured FM steels are discussed followed by a review of nanostructured structured steels properties and compositions. The manufacturing methods for processing nanostructured steels are discussed with effects of processing parameters. At the end of the chapter, the objectives of this study are outlined.

Conventional steel bearings suffer from the disadvantages of narrow operating temperature limits, high thermal expansion and low fatigue life [1]. The use of ceramic balls packed in steel races appears to be a promising solution for these problems. The roller contact bearings with ceramic balls rotating in steel races are termed as hybrid bearings. The hybrid bearings contain silicon nitride or a similar low density ceramic as rolling ball material with steel

rings and races. By virtue of a lower density than steel, the centrifugal force exerted on the steel races is lower resulting into less outward thrust. Hence, in high speed turbines, jet engines, and rocket propellant pump, the huge centrifugal thrust generating due to high speed can be reduced. These bearings show increased fatigue life as well as better wear behavior than the all steel conventional bearings [2, 3]. Ceramics have lower coefficient of thermal expansion, and high stiffness as compared to steel. Being insulators, the ceramic balls also provide electrical insulation between the machines. The working temperature range for ceramics is around 1000ºC. Hence, the steel that can retain the mechanical properties at highest possible temperature is an area of a study. High corrosion resistance against the lubricants at elevated temperatures is also an important criterion for the ceramic as well steel selection.

There are different types of steels that are used as a material for bearing balls and rings. AISI 52100 1.5% Cr is the most common steel used as a bearing material and possesses high strength and wear resistance [4]. Zhou *et al.* [5] carried out a wear analysis of a nanostructured AISI 52100 prepared by surface mechanical attrition treatment. For better corrosion resistance, the stainless steel containing Cr > 15% is used. AISI 440C is a popular martensitic stainless steel used as a bearing material where high corrosion resistance and high temperature (up to 250ºC) resistance are important [6]. Wang *et al.* [7] carried out tribological testing of nanostructured AISI 304 stainless steel against a ceramic tip. Dong *et al.* [8] carried out a systematic wear analysis of 1Cr-Mo steel against alumina ball at different load and velocity combination. Zum Gahr [9] published a review on ceramic-ceramic and ceramic-steel contact pairs, but the importance was given to the wear of a ceramic surface. Li *et al.* [10] performed sliding wear analysis of 316 austenitic stainless steel against WC/Co ball at 10N load.

1.2 Nanostructured steels: A review

Mechanical as well as wear properties of a material can be improved substantially by refining the grain size. The grain size-property correlation is explained by Hall-Petch equation in some recent works [11, 12]:

$$\sigma = \sigma_0 + \frac{k}{\sqrt{d}}, \dots\dots\dots\dots\dots\dots\dots\dots\dots\dots\dots\dots\dots\dots\dots\dots. \dots\dots\dots\dots\dots (1.1)$$

where σ is property of the material which can be strength or hardness, σ_0 is a value of a property of a single crystal, k is a Hall- Petch constant and d is a grain size of the material. Also refining the grain size increases the area of grain boundaries which act as barriers for dislocation motion.

1.2.1 Ferritic nanostructured steels

Cr is a key alloying element in steel that stabilizes ferrite phase as well as makes steel corrosion resistant. Steel containing more than 12% Cr (% wt.) is considered ferritic steel. In the last decade, several promising nanostructured ferritic steels having a high strength and hardness at elevated temperatures were developed. 304 stainess steel, 12Y1, 14WT, and 430L are the few promising candidates among them. The compositions of these steels are listed in Table 1.1.

12Y1 and 14WT steels contain 12% and 14% Cr respectively. 14WT steel is generally produced by hot extrusion of elemental powders. Mclintock *et al.* ball milled the elemental powders for 40 h and then hot extruded at 850ºC [13] to produce 14WT. 12Y1 steel is manufactured by the same path as of 14% Cr steels. Ukai *et al.* ball milled elemental powders followed by extrusion for 12% Cr steels at 1150ºC to produce 12Y1 [14].

Table 1.1 Elemental composition of ferritic nanostructured steels [7, 13]

Element*	12Y1	304	14WT	430L
C	0.045	0.080	0.240	0.080
Cr	12.850	19.000	13.930	16.290
V	0.007	-	-	-
Mo	0.030	-	0.006	0.060
Nb	-	-	0.006	-
Mn	0.040	2.000	0.040	0.280
P	<0.001	0.040	0.008	0.031
S	0.002	0.030	-	0.020
Si	0.030	1.000	0.160	0.940
Ni	0.240	9.000	0.028	0.530
N	0.017	-	0.150	-
Al	0.007	-	0.040	-
Co	0.005	-	-	-
Cu	0.010	-	0.001	-
B	0.004	-	-	-
W	<0.010	-	0.160	-
Zr	0.003	-	-	-
Ti	0.003	-	0.240	0.003

***Fe balance**

Hong-wei *et al* [15] consolidated 430L stainless steel nanocrystalline powder with spark plasma sintering to produce a nanostructured 430L steel. The sintering was performed at different temperatures in the range of 700ºC to 1000ºC and holding time ranging from 5 to 15 minutes to achieve the maximum density. The work showed the dependence of hardness and strength on relative density as a function of temperature. The relative density of the sample is a direct function of a sintering temperature. Fig. 1.1 shows the improvement in hardness for a steel

430L as a function of sintering temperature at a constant holding time of 5 min. Fig. 1.2 shows the TEM image of spark plasma sintered 430L nanostructured steel. The average grain size increased from 179 nm to 335 nm when holding time was changed from 5 min to 10 min at 900ºC [15].

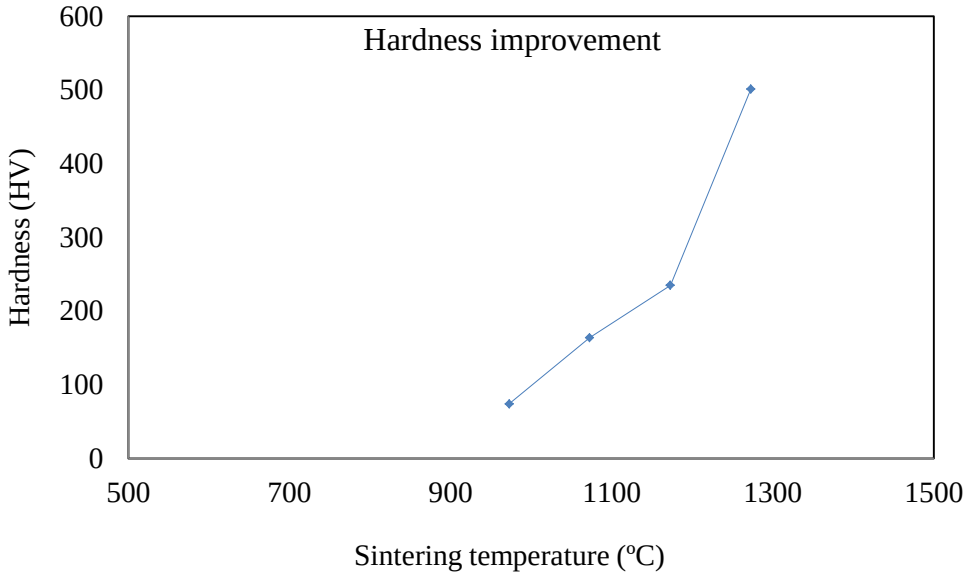

Figure 1.1 Hardness versus sintering temperature of 430L steel (Reprinted from [15] with the permission of the publisher).

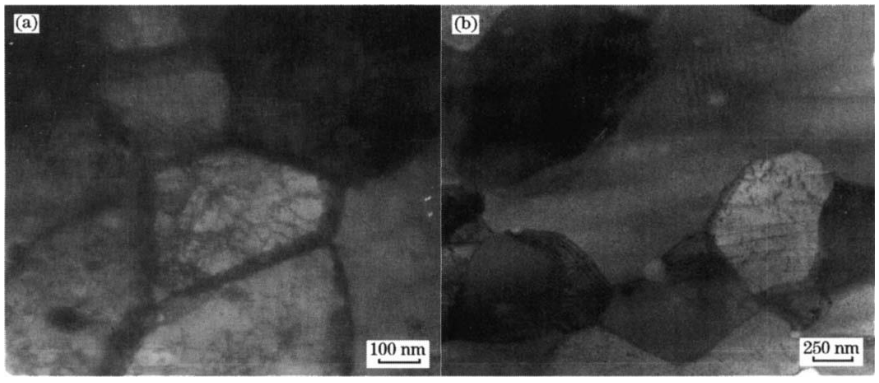

Figure 1.2 TEM images of spark plasma sintered 430L: (a) 900ºC (5 min.), and (b) 900ºC (10 min.) (Reprinted from [15] with permission of the publisher).

1.2.2 Ferritic-martensitic (FM) nanostructured steels

FM steels contain 7-11% Cr as a key alloying element. Since last decade, a range of steels containing 9% wt. Cr (9Cr steels) are being investigated systematically for mechanical and physical property improvement. By virtue of existing high creep and corrosion resistance at 600-650ºC, 9Cr steels are widely used as a tubing material for steam power plant components [16]. Modified 9Cr-1Mo, P91, and HT9 are the popular compositions to list a few (Table 1.2) [17]. These steels possess low stress crack corrosion susceptibility and high thermal conductivity compared to their austenitic counterparts. The Fe-Cr oxide layer helps in restricting the oxidation of these alloys at high temperatures. These alloys are also in development as a structural material for nuclear reactors. The development is facilitated by industrial awareness and developed manufacturing processes for FM steel.

These FM steels have both ferrite and martensite phases existing together at room temperature. The Proportion of ferrite and martensite can be controlled by adjusting the rate of cooling from an austenite range to room temperature. This unique combination of soft ferrite and hard martensite phase together gives these steels a composite effect. FM steels are known for a combination of toughness and hardness at high strength. HT9 and modified 9Cr-1Mo are the most promising FM steels used in the power generation industry over past two decades.

1.2.2.1 Modified 9Cr-1Mo steel

1.2.2.1.1 Properties and microstructure

The modified 9Cr-1Mo is a specialized alloy in a group of FM steels also known as ‘ASME T91’. As shown in Fig. 1.3, the microstructure of modified 9Cr-1Mo steel contains martensite

laths distributed in ferrite matrix. In an as tempered condition, all martensite is converted into large $M_{23}C_6$ carbides (M= Fe, Cr) which precipitate out during cooling.

Table 1.2 Elemental compositions of ferritic-martensitic steels.

Element*	HT9	Modified 9Cr-1Mo
C	0.200	0.100
Cr	11.630	8.370
V	0.300	0.216
Mo	1.000	0.900
Nb	-	0.076
Mn	0.450	0.450
P	0.020	0.009
S	0.006	0.003
Si	0.220	0.280
Ni	0.500	0.210
N	-	0.048
Al	0.010	0.022
Co	-	-
Cu	-	0.170
B	-	-
W	0.520	-
Zr	-	-
Ti	-	-

*Fe balance

These large precipitates form at the prior austenite grain boundaries and sub-grain boundaries. Addition of vanadium (V) and niobium (Nb) promotes additional carbide formation in 9Cr-1Mo. This modification results in formation of ultra-fine M_2C and M_6C (M= V or Nb). These precipitates are characterized to be typically in the range of 1-5 nm [18].

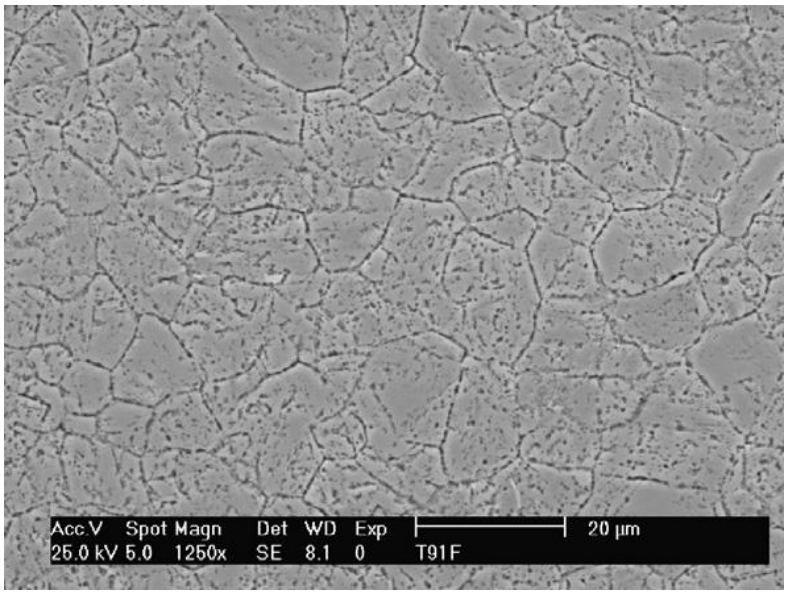

Figure 1.3 Microstructure of normalized and tempered 9Cr-1Mo steel (Reprinted from [17] with the permission of the publisher).

Because of this unique combination of hard phase distributed into soft matrix, modified 9Cr-1Mo steel possesses both high strength and ductility. Filemonowicz *et al.* [16] presented a detailed investigation of microstructure and properties of modified 9Cr-1Mo steel in their work. Many recent works are published on oxidation and corrosion behavior of modified 9Cr-1Mo steels in different working conditions [17, 19-21]. Falat *et al.* [22] studied the creep characteristics and microstructural behavior of modified 9Cr-1Mo steel welded with austenite steel. Ukai [23] carried out the high temperature strength experiments of spark plasma sintered modified 9Cr-1Mo steel. The nanostructured as well as its ODS version of modified 9Cr-1Mo was spark plasma sintered at 1150ºC. Heintze *et al.* [24] performed nanoscale characterization of oxides dispersed in modified 9Cr-1Mo steel produced by spark plasma sintering and hot isosatic pressing. Saroja *et al.* [25] carried out a microstructural characterization of 9Cr steel manufactured by hot extrusion of ball milled elemental powder. The composition of the alloy

used in their work is similar to modified 9Cr-1Mo except the absence of molybdenum in it. Fan *et al* [26] manufactured a nanostructured modified 9Cr-1Mo steel with a novel method, equal channel angular pressing (ECAP). In their work, the changes occurred in microstructure during the process as well as mechanical properties are explained at each processing step.

As shown in Fig. 1.4 (a) 9% Cr steels, there is an appearance of first melt at ~1690 K (1417ºC). The required weight proportion of martensite and ferrite phase can be achieved by adjusting the cooling rate of steel from austenite region. The typical heat treatment consists of normalizing steel from 1300ºC and tempering it to 600ºC for balancing the strain caused during normalizing and transformation of martensite into carbides. Fig. 1.4 (b) shows Time-Temperature-Transformation (T-T-T) curve of 9Cr-1Mo steel. This diagram gives exact idea about cooling rate to be maintained while heat treating the steel.

1.2.2.1.2 Applications

The modified 9Cr-1Mo steel is widely used in the power generation industry over the past two decades. In the current scenario, owing to its high temperature creep resistance, this steel is used for a temperature range of 450 to 700ºC with high pressure up to 22 MPa [27]. This steel is also used as a material for tubing, and pressure and safety valves in the gas and oil industry by virtue of its corrosion resistance.

1.3 Manufacturing of nanocrystalline materials

Numerous processes have been developed in the past two decades for manufacturing of nanocrystalline powders and their further compaction to a nanocrystalline bulk material. This approach is termed as a ‘bottom up approach’.

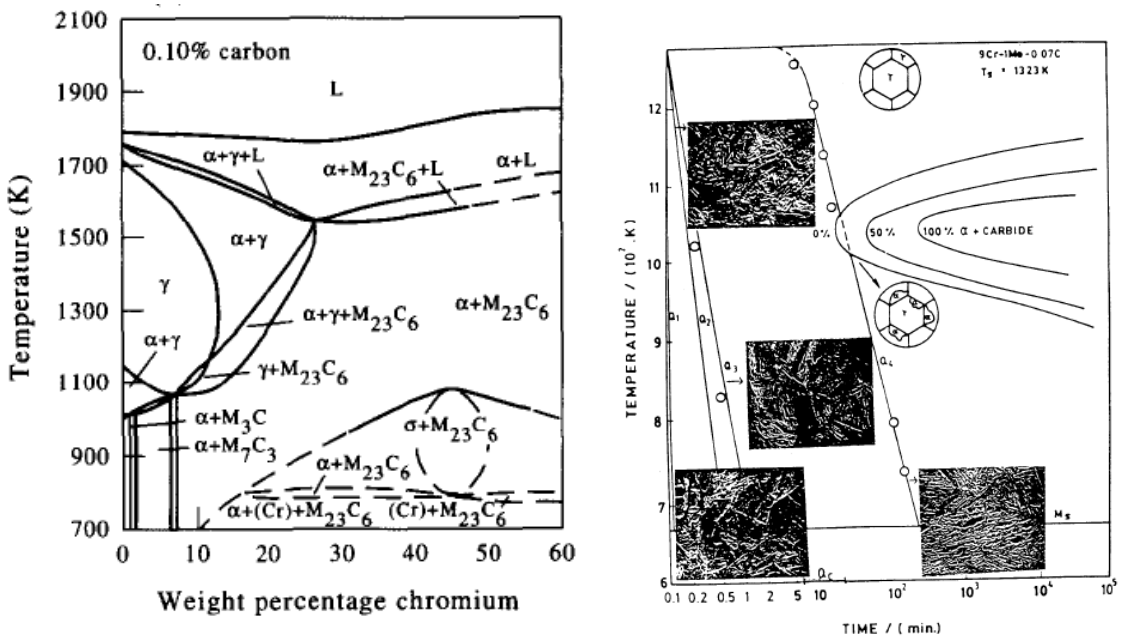

Figure 1.4 (a) Ternary phase diagram of Fe-Cr-C at 0.1% C, and (b) T-T-T diagram of modified 9Cr-1Mo steel (Reprinted from [28] with the permission of the publisher).

Few methods are capable of refining the grain size of an existing bulk material termed as a 'top down approach'. In this section advanced methods are discussed including both approaches for manufacturing a nanocrystalline bulk.

1.3.1 Top-down approach

In this approach, the nanoscale parameters are generated in the existing bulk material. The nanoscale grains are produced by severe plastic deformation. The popular techniques involving top-down approach are discussed below.

1.3.1.1 Surface mechanical attrition (SMA)

The surface mechanical attrition treatment involves severe plastic deformation of a surface layer to produce a nanocrystalline microstructure. Hardened stainless steel balls with high velocity (1-20 m/s) are bombarded on the surface of the sample. This impact creates strain induced dislocations forming a regular dislocation grid. At the later stage, with higher strain, the newly generated twins in different planes intersect each other and subdivide the grains into smaller blocks. As the strain is highest near the surface, the further interaction of twins creates nano size grains adjacent to the surface layer.

The SMA process and experimental set up and are discussed in detail by Lu *et al.* [29]. Lin *et al.* [30] created 10 μm deep layer of nanocrystalline grains on AISI 321 steel with SMA. The main disadvantage of the method is the thickness of subsurface nanocrystalline layer is small and there is a gradient of grain size from surface to bulk. SMA cannot produce bulk nanocrystalline samples.

1.3.1.2 Equal channel angular pressing (ECAP)

In this method, the sample is forced through two channels, joined to each other at 90º. The sample experiences severe plastic deformation at the joint. The high strain resulting due to deformation causes the microstructure refinement [31]. Final grain size depends upon the number of times the sample is passed through the channel and also on the rotation of the sample in between the passes. The experiments are carried out at the room temperature.

Huang *et al.* [32] manufactured nanocrystalline austenitic steel with an average grain size of 74 nm with 8 passes by ECAP method. The sample was rotated by 90º counterclockwise before each pass. Bing *et al.* [33] processed low carbon steel with 0.08% C to achieve a grain

size of 200-400 nm after 8 passes by ECAP method. The sample was rotated by 90º counterclockwise before each pass. Foley [34] performed ECAP of modified 9Cr-1Mo steel to get a nanocrystalline microstructure.

1.3.2 Bottom-up approach

In this approach the nanoscale features are assembled together to create a nanocrystalline bulk. In this section the methods for production of nanoscale particles are discussed. Later the assembly methods of these particles for creating a nanocrystalline bulk are discussed.

1.3.2.1 Methods for producing nano particles

1.3.2.1.1 Inert gas condensation

This method is used for production of nanoparticles of the size range 1-10 nm. As explained by Gleiter [35], a metal is evaporated by the best available heating technique in a high vacuum (10^{-10} MPa). The chamber is then slowly filled with low pressure inert gas. The evaporated metal atoms after colliding with inert gas atoms lose kinetic energy and condense down to nano size particles. The metal powders produced with this method can be alloyed together using mechanical milling. Subsequent compacting of alloyed fine powder produces nanocrystalline bulk. Djekoun *et al.* [36] manufactured Fe and $Fe_{50}Ni_{50}$ nanocrystalline powder of a size 4-70 nm in a pure He atmosphere. This powder can be ball milled with the other elemental powders mechanically to produce a required composition.

1.3.2.1.2 Gas atomization

Gas atomization is a technique used to produce ultrafine powders of metals. In this technique a metal is melted in a vacuum in an induction crucible. In the next step, the melt is allowed to cool

in a low pressure high purity inert gas atmosphere to produce a fine powder. The exact flow mechanisms and set up details are discussed by Anderson *et al.* [37] in their work. Min *et al.* [38] manufactured Fe-25 Cr powders of size smaller than 38 μm by gas atomization. Mclintock [39] used the gas atomized powders of 14 YWT, 12 YWT for manufacturing ODS nanostructured steel. Oksiuta *et al.* [40] alloyed the gas atomized 14WT powders with yttria to produce a 14YWT powders. The further extrusion of powder at 1100ºC produced the bulk 14YWT steel. The main disadvantage of this method is that high set up and maintenance cost is involved in powder production.

1.3.2.1.3 Ball milling of coarse particles

Ball milling of coarse powder particles to produce fine particles is the easiest approach for producing a nanocrystalline powder. In 1930's Stern [41] came up with an idea of treating waste aluminum scrap and producing ingots by hot extrusion. It was further noticed that decreasing the particle size before extrusion results in high density bulk. Enayati *et al*.[42] ball milled stainless steel scrap for 48 h to produce a nanocrystalline powder. The exact mechanism and the role of parameters in ball milling are discussed in the next section.

1.4 Ball milling

1.4.1 Mechanism of ball milling

Ball milling process involves repeated break down and cold welding of powder particles due to the impact of high energy balls in a ball mill. This process is ideal for producing nano size powders of high yield. During the milling process, the particles of powder trapped between two hard balls experience an impact of high energy. This impact force can result in flattening, cold welding or fracturing of powder particles.

Being a ductile material, at the initial stage of ball milling, steel particles can handle plastic deformations and get welded to other particles, simultaneously getting flattened. This result in formation of a layered structure of fine particles welded together. At the later stage, the strain developed in crystallites crosses the yield limit and results in work hardening of particles. With continued ball milling, these welded particles fracture into small fragments. Again the cycle continues with rewelding of small fragmented particles and formation of a layered structure. At the stage, the equilibrium between fracturing and rewelding is achieved and the process is called balanced. At this stage, the average number of rewelding particles is equal to the average number of fracturing particles [43].

1.4.2 Process variables

Ball milling process is governed by combination of many parameters. These parameters are discussed below with their role in the process.

1.4.2.1 Type of mill

There are numerous types of ball mills available based on their operation speed, powder handling capacity and control on milling atmosphere. The Table 1.3 enlists ball mill type according to capacity of powder handling. Planetary ball mill is preferred for laboratory level, as it has medium powder handling capacity and cost effectiveness.

1.4.2.2 Milling speed

At higher speeds, the temperatures in a ball mil jar can increase up to the level where unwanted phase transformations can occur in a sample powder. This transformation result in contamination

of the powder. Hence the maximum speed of the process should be chosen such that it does not result in a generation of high temperatures that can cause contamination.

Table 1.3 Typical capacities of ball mills [43].

Type of mill	Capacity
Mixer mill	40 gm
Planetary mill	1000 gm
Attritor mill	0.5-100 kg
Universal ball mill	Up to 2000 kg

Although in some cases, where diffusion of one phase is required to happen in second phase, higher temperatures can give the best results. Kuhrt C *et al.* [44] in their studies reported that, due to dynamical recrystallization at higher temperatures, the size of nanocrystals increases and the internal strain in particle decreases. Ramar *et al.* [45] in their work on EUROFER alloy, used ball milling speed as 875 rpm to achieve the crystallite size below 20 nm. Ukai [46] used speed of 420 rpm for balling of 9Cr yttria dispersed steel powder to nanometer size. While producing nanocrystalline powder from scrap stainless steel chips, Enayati *et al.* [42] performed ball milling operation at 435 rpm.

1.4.2.3 Milling time

Milling time for the process should be chosen such that a balance between fracturing and welding of powder particles is achieved. Suryanarayana [43] in his study about intermetallics mentioned the possibility of powder contamination if milled for more than the required time period. Ramar *et al.* [45] ball milled the EUROFER alloy for 14 h to achieve nanocrystalline

powder. Enayati *et al.* [42] ball milled stainless steel scraps for 48 h as the hardness of milling balls was 800 HV in comparison with 2000 HV of silicon carbide balls used by Ramar *et al.* [45].

1.4.2.4 Ball to powder weight ratio (BPR)

Ball to powder weight ratio varies from 1:1 to 200:1 depending upon the material used as well as the time of ball milling. The ratio 10:1 is the most popular and commonly used BPR for planetary ball mills. At high BPR, the numbers of collisions per unit time are more resulting in faster milling. On the other hand, at high BPR, energy transferred per unit time to powder particles also increases resulting into higher temperatures. Enayati *et al.* [42] and Ukai [46] performed ball milling with 10:1 BPR. Referring these works, we chose 10:1 as BPR for our ball milling process.

1.4.2.5 Ball diameter

For a smaller ball diameter, number of the collisions per unit time increases. However, the energy of impact decreases. 5-6 mm is the most common ball diameter used for planetary ball mills.

1.5 Compaction of nanocrystalline powder

A number of methods have been developed in the last two decades, to consolidate the ball milled powder into the bulk. However, a process needs to be capable of maintaining the nanocrystallinity in bulk material after consolidation. The process should have precise control on process parameters as well as high yield to produce bulk samples in a shorter time. In this section, powder consolidation techniques relevant to our work are discussed.

1.5.1 Hot isostatic pressing (HIP)

Hot isostatic pressing is a method that involves application of uniaxial pressure at high temperature to produce a bulk from powder. The mechanism governing hot isostatic pressing and detailed process analysis are explained by various authors [47, 48]. For consolidation of steel, a temperature of typical range 800-1200ºC is used depending upon the composition. A 20 to 200 MPa uniaxial pressure is applied until 100% dense bulk is achieved. The typical holding time for steel samples is 30 to 120 minutes. This long holding time at elevated temperatures causes grain growth and recrystallization resulting into the loss of nanocrystallinity in bulk sample.

1.5.2 Spark plasma sintering (SPS)

SPS is an advanced technique developed for consolidation of powders. SPS is a rapid sintering method which enables full densification of powder at lower temperature and in shorter sintering time. The SPS system simultaneously applies a uniaxial pressure and pulsed DC current on a powder filled in die-punch assembly made up of a conductive material. The ON-OFF pulse DC current generates plasma at the contact point of powder particles. This plasma creates an impact pressure which helps breaking the oxide layer at the surface of powder particles before bonding [49]. The Joule heating momentarily generates high temperature at the contact point of particles and results in the formation of a bond. However, there are no practical evidences found about formation of plasma [50]. The SPS system offers numerous advantages over the conventional systems using hot isostatic pressing (HIP), hot extrusion and shock wave compaction including high reproducibility, reliability, safety as well as accurate parametric control and ease of operation. As the lower sintering temperature and shorter sintering time are the crucial factors in maintaining nanocrystallinity, the SPS system is the ideal for fabrication of nanocrystalline

materials [51]. The exact SPS mechanism along with the role of parameters and the process set up is discussed in the section 1.7.

1.5.3 Hot extrusion

Hot extrusion is the most commonly used method for consolidation of steel powder into bulk. The first step in the process is filling steel powder in a metal can called canning. The can is then extruded through a die at a pressure of a range 250 tonnes and temperature ~1000ºC. Post extrusion the can is preheated for 1 h and then degassed. McClintock [39] performed hot extrusion of ball milled 14 YWT powder at 1100ºC to produce a nanocrystalline bulk.

1.5.4 Shock wave compaction

Shock wave compaction method is recently used for consolidation of nanocrystalline bulk. Schwarz *et al.* [52] explained a theory of shock wave compaction of powders in their work. In this method, the shock wave is generated by blast of condensed explosions. As adiabatic expansion of powders accompany the dynamic compression, a high rate of cooling is certainly possible. Chikhradze *et al.* achieved compaction of nanocrystalline Al powder dispersed with ultrafine Ti particles with shock wave compaction [53]. Alba-Baena et al. [54] successfully compacted Al/CNT two phase system with shock wave compaction method.

1.6 Spark plasma sintering (SPS)

1.6.1 SPS mechanisms

The spark plasma sintering densification mechanisms consist of two important steps [55];

1.6.1.1 Particle rearrangement

In the first step, the inter-particle and intra-particle pores are eliminated by particle rearrangement. This particle rearrangement step is activated by application of initial uniaxial pressure on the powder. This step is important for removing the porosity in the powder before next step.

1.6.1.2 Plastic deformation and neck formation

In the second step, the particles are plastically deformed and the curvature is reduced due to the increasing applied pressure and the simultaneous increasing temperature. The whole SPS mechanism is driven by the reduction in surface energy of powder particles. In this step, the pulse DC current creates a spark between two particles and also causes the Joule heating. The spark results in the generation of localized high temperature that causes localized melting of particles at contact points. This localized melting creates neck between two particles and further growth of the neck takes place with increasing temperature and time.

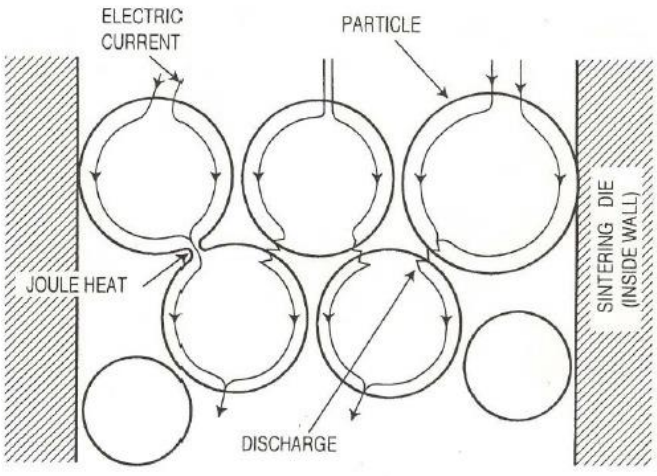

Figure 1.5 Schematic representation of a generation of Joule heat at the contact of the particles due to pulse DC current [49].

Each particle creates several necks with adjacent particles and the growth of these necks depends upon the pressure and the size of particles in contact. The localized heating of particles ensures the densification of the powder at low temperature and short time period. Hence, the SPS process is capable of inhibiting the grain growth and maintaining the nanocrystallinity in bulk.

1.6.2 Effect of parameters on densification

1.6.2.1 Effect of temperature

As the neck formation between the powder particles is driven by Joule heating, the densification process is expected to be dependent on temperature. Garay [55] concluded that the processing temperature (T) to achieve near fully dense samples should be 0.5-0.8 times of the melting temperature (T_m) of the sample. By plotting relative density with (T_m/ T), the equation of a straight line is given by:

$$\rho = s\left(\frac{T}{T_m}\right) + b, \dots \dots \dots \dots \dots \dots \dots \dots \dots \dots \dots \dots \dots \dots \dots \dots \dots \dots \dots \dots (1.2)$$

where ρ is the relative density of sample, s is the slope of a straight line, and b is the intercept of the straight line on relative density axis. The term s is also referred as a temperature sensitivity of a material, and typical values of various materials are listed in [55].

1.6.2.2 Effect of pressure

As the particle rearrangement and plastic deformation is assisted by applied pressure, the densification process is also dependent on the applied uniaxial pressure. The relative density of the sample is increases with the increase in applied pressure [55]. The limiting factor for

maximum applied pressure is the strength of die material. The relationship between pressure and relative density is given by:

$$\frac{\partial \rho}{(1-\rho)\partial t} = B\left(g\,\frac{\gamma}{x} + P\right), \ldots\ldots\ldots\ldots\ldots\ldots\ldots\ldots\ldots\ldots\ldots\ldots\ldots\ldots\ldots\ldots (1.3)$$

where ρ is a relative density, t is a time, B is a constant dependent on diffusion coefficient and temperature, γ is a surface energy, x is a particle size, and P is an applied pressure.

1.6.2.3 Effect of heating/cooling rate

High heating rate is one of the important advantages of SPS system as it significantly reduces the processing time. Typical heating rates of the SPS system are between 100ºC/min to 600ºC/min against 20ºC/min to 50ºC/min for hot isostatic pressing [55]. This high heating rate not only shortens the time of densification but also helps in inhibiting the grain growth. As the sample is quickly taken to maximum temperature, the time spent at each temperature decreases and the possibility of grain growth is reduced. Hence high heating rates help in maintaining the nanocrystallinity of bulk.

1.6.2.4 Effect of pulsed DC current

The role of pulsed current and the exact sintering mechanism resulting due to it is still under debate. However, the role of pulsed current in producing Joule heating at particle contacts and enabling the densification in short time interval is universally accepted. Several studies have been conducted to study the effect of pulse current which concluded that the pulsing of the current has no significant effect on densification [56, 57].

1.7 Objectives of study

The objectives of this study include,

- Investigate processing of the nanostructured 9Cr-1Mo steel by spark plasma sintering of a ball milled steel powder.
- Investigate the effect of spark plasma sintering parameters on densification and microhardness of modified 9Cr-1Mo steel.
- Investigate the wear behavior of spark plasma sintered modified 9Cr-1Mo steel with alumina and silicon nitride balls and compare it with the as-received 9Cr-1Mo steel.

CHAPTER II

EXPERIMENTAL DETAILS

2.1 Materials

2.1.1 Composition

The modified 9Cr-1Mo steel used in this work was purchased from American Alloy Steel, Bixby, OK in the form of a 203 mm × 203 mm square plate with 12.7 mm thickness. The elemental composition was measured by a chemical analysis by the manufacturer and is listed in Table 2.1. The steel was received in normalized and tempered condition with carbides distributed in the ferrite matrix.

2.1.2 Properties

The mechanical properties of as-received modified 9Cr-1Mo steel are mentioned in Table 2.2 as provided by American Alloy Elements. The tensile strength of the as-received steel was in the range of 585-760 MPa. The melting point of the FM steel was found to be around 1800°C and the microhardness of the as-received steel plate was measured to be around 212 HV.

Table 2.1 Composition of the as-received modified 9Cr-1Mo plate.

Element	% wt.
Fe	87.5-90
Cr	8-9.5
Mo	0.85-1.05
V	0.18-0.25
C	0.08-0.12
Mn	0.3-0.6
P	0.02 max
S	0.01 max
Ni	0.4 max
Nb	0.06-0.1
N	0.03-0.07
Al	0.04 max
Si	0.2-0.5

Table 2.2 Mechanical properties of as-received modified 9Cr-1Mo steel.

Property	Value
Tensile strength (MPa)	585-760
0.2% yield strength (Mpa)	415
% Elongation in 50 mm diameter sample	18
Melting point (°C)	1800°C [28]
Hardness (HV) at 100gf	212

2.2 Experimental procedure

2.2.1 Preparation of starting powder for ball milling

Drilling operation was used to produce chips from an as-received modified 9Cr-1Mo steel plate. The plate was mounted on a vertical spindle milling machine as shown in Fig. 2.1 The tool steel drill bit used was 5 mm in diameter. The drilling operation was performed at the spindle speed of 750 rpm. A water based coolant was continuously poured during machining to avoid any unwanted phase transformation resulting from high temperatures. The average thickness of chip

Figure 2.1 Vertical spindle milling machine.

was 50 μm with length 5 mm and breadth 1 mm. Post machining, the chips were cleaned in an ultrasonic bath with acetone for 10 min to remove the traces of coolant, dirt etc., followed by heating at 150ºC. The chips were scanned with a magnet to remove any unwanted metal piece.

The as cleaned modified 9Cr-1Mo steel chips were ball milled with, high energy ball mill (Pulverisette 7, Fritsch) (Fig. 2.2), to produce nanosize powder particles. 50 g of steel chips were filled in equal amounts in two tungsten carbide jars along with 6 mm diameter silicon carbide balls. The handling of powder in the jar was performed inside high purity argon glove box in order to avoid any contamination. The ball to powder weight ratio was maintained at 10:1. The ball milling operation was performed at 500 rpm with 15 minutes pause after every 1 minute of milling. The intermittent pause was taken to avoid any unnecessary rise in temperature in ball mill jars. The dry ball milling was performed without any process control agent.

Figure 2.2 High energy planetary ball mill.

The ball milling operation was performed for total of 4 h. After every 0.5 h of ball milling, 2 g powder was separated for SEM and XRD analysis. After 2 h of ball milling, the powder was

sieved by 100 micron mesh size brass sieve to get rid of coarse particles and to expedite the process. Powder handling and sieving was carried out in argon atmosphere glove box (Fig. 2.3). The air pressure inside the glove box was -0.3 mbar (-0.00003 MPa) and O_2 concentration was 0.5 ppm.

2.2.2 Spark plasma sintering

The ball milled powder was packed in a graphite die of an internal diameter of 10 mm. Two graphite punches of length 25 mm and diameter 10 mm were cut on a Techcut 4 diamond saw cutter. The die-punch assembly is shown in Fig. 2.4. As shown in Fig. 2.4 a small blind hole on the die was made for inserting a thermocouple during the sintering process.

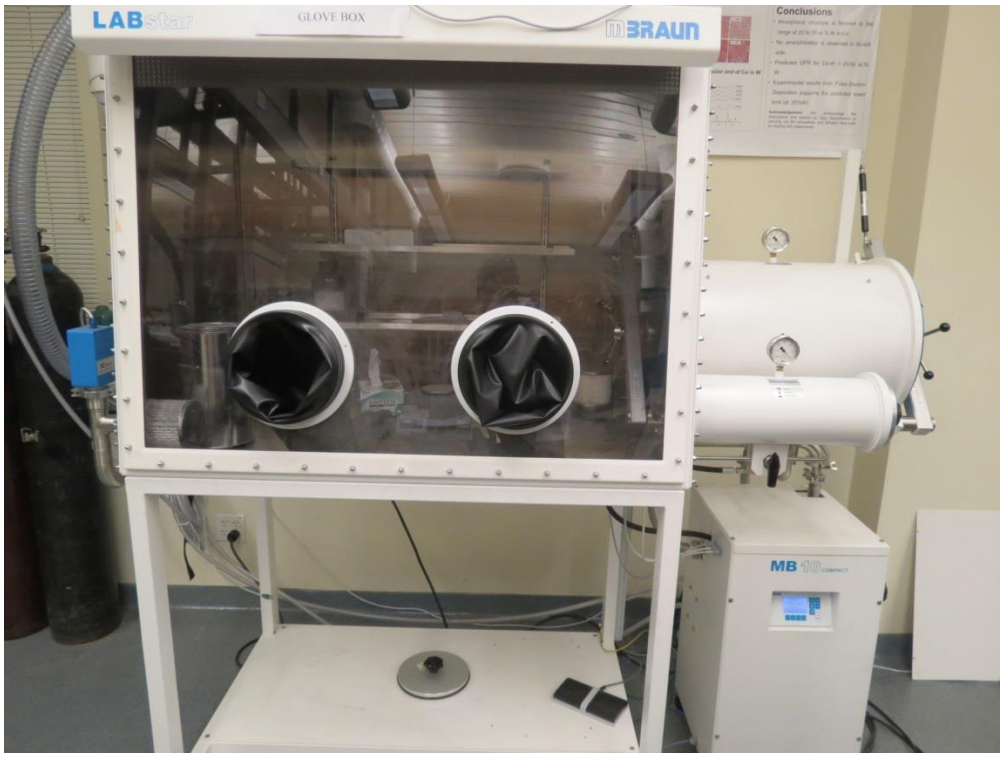

Figure 2.3 High purity argon glove box.

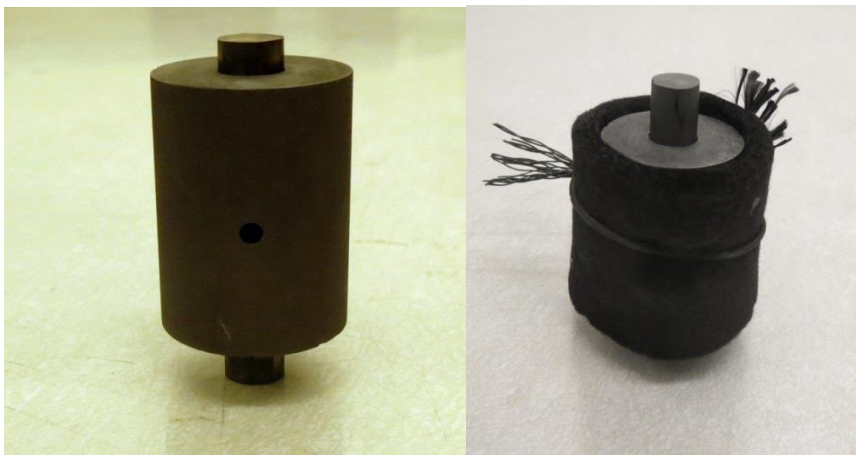

Figure 2.4 (a) Graphite die punch assembly, and (b) assembly covered with graphite blanket.

A graphite blanket was wrapped around the assembly to minimize the heat loss due to high radiation during sintering process. The temperature measurement was performed by the K- type thermocouple.

SPS of as milled modified 9Cr-1Mo nanopowder was performed using commercial machine (SPS 10-3, Thermal Technologies LLC, Santa Rosa, CA) (Fig. 2.5). The sintering of powder was performed at parameters which are listed in Table 2.3. For each sintering process; a preload of 6 MPa is applied to hold the die-punch assembly in SPS machine. Each sample was sintered at the constant heating rate of 100ºC/ min. Post-sintering the sample was removed from the die punch assembly with the help of vertical bench press.

Table 2.3 Spark plasma sintering parameters.

Processing no.	Sintering temperature (°C)	Sintering pressure (MPa)	Holding time (Min)
Processing 1	500	70	5
Processing 2	500	70	10
Processing 3	800	70	5
Processing 4	800	70	10
Processing 5	1100	70	5
Processing 6	1100	70	10

Figure 2.5 Spark plasma sintering set up.

2.3 Material characterization

2.3.1 Relative density

The density of as-sintered sample was measured using Archimedes' principle with distilled water as an auxiliary fluid. The theoretical density of the modified 9Cr-1Mo steel was taken as 7.67 g/cc [34]. The equation governing Archimedes' principle is:

$$\rho = \frac{x}{x-y}\,(\rho_0 - \rho_a) + \rho_a, \dots\dots\dots\dots\dots\dots\dots..\dots\dots\dots\dots..\dots\dots\dots \quad (2.1)$$

where ρ is an actual density, ρ_0 is density of water taken as 0.99804 g/cc, ρ_a is density of air taken here as 0.0012 gm/cc, x is the weight of sample in air and y is the weight of sample in water or auxiliary fluid. In this work, the density was measured by a density measurement kit (Delta Range XD204, Mettler Toledo). Further, the relative density of sintered sample was calculated by formula:

$$Relative\ density = \frac{Measured\ density}{Theoretical\ density} \times 100 \dots\dots\dots.. \quad (2.2)$$

2.4 Microstructural and phase analysis

2.4.1 Scanning electron microscopy (SEM)

For SEM analysis, as-received steel plate was cut in a rectangular shaped small plate of size 2 mm in thickness with 10 mm breadth and 30 mm length. The low speed cutting fluid is used as a coolant to avoid any unwanted temperature rise. The sample surface was ground on rotary grinder polisher (160 E, MoPao) (Fig. 2.7) with 240, 400, 600, 1200 grit silicon carbide papers in increasing order of fineness.

Figure 2.6 Diamond saw cutter.

Figure 2.7 Grinder polisher.

The grinding was accompanied by constant flow of water to wash away the loose particles. The grinding operation was followed by polishing with the 5 μm silica colloidal suspension on a fine polishing cloth. For final inspection, the sample surface was cleaned by acetone before etching

with 2% nital for 45 seconds. Similar grinding and polishing steps were followed for surface preparation of SPS samples. The SEM images were collected on microscope (600F, FEI Quanta) (Fig. 2.8).

2.4.2 X-ray diffraction (XRD)

The XRD analysis was performed to check if any new phase transformation has occurred during process and also to determine the crystallite size of powder particle and bulk samples. The dimension of as-received steel sample used for XRD was similar to that of SEM sample. Similar grinding and polishing steps were followed for surface preparation of as-received and sintered samples.

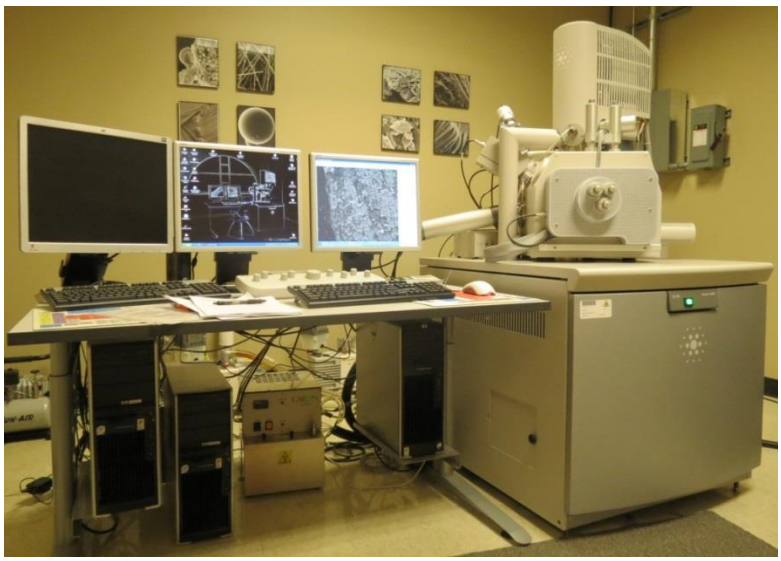

Figure 2.8 Scanning electron microscope.

After grinding and polishing, the sample surface was cleaned with acetone followed by methanol washing.The x-ray diffraction analysis was performed on Philips Norelco x-ray diffractometer with CuKα radiation of wavelength 1.54178 Å. The x-ray diffraction results obtained were plotted with a software package Origin Pro 8.6 64 bit for further analysis.

2.4.3 Transmission electron microscopy (TEM)

The transmission electron microscopy analysis was performed on the ball milled powder sample to determine the size of an individual particle. 0.1 gm of powder was separated from one of the ball mill jar after 4 h of operation. The powder was suspended in 100 ml of methanol followed by ultrasonication for 5 minutes to avoid agglomeration of particles. A droplet of sample was put on a copper grid of mesh 10 microns. Bright field TEM images of the powder were obtained on the JEOL (Japan Electron Optics Laboratory) JSM 6360 microscope with an accelerating voltage of 200 kV (Fig. 2.9).

Figure 2.9 Transmission electron microscope.

2.4.4 Energy dispersive x-ray spectroscopy (EDS)

EDS analysis was performed for the analysis of worn surfaces of the sintered samples and ceramic balls. The energy dispersive x-ray spectroscope (Evex) coupled with the SEM set up was used to scan the sample surface (Fig. 2.10). The associated software package was used to analyze and map the elements in the scanned images. The EDS set-up was only capable of detecting the elements heavier than sodium (atomic weight= 22.98 amu). Hence, the mapping of carbon, nitrogen and oxygen is not performed in the present work.

Figure 2.10 Energy dispersive x-ray spectroscope.

2.5 Mechanical testing

2.5.1 Microhardness

Microhardness measurements were performed on microhardness tester (CM-700-AT, Clark) (Fig. 2.11). The polished samples were used for microhardness testing. Vicker's diamond pyramid indenter was used with an applied load of 9.8 N and holding time of 15 seconds.

Figure 2.11 Microhardness tester.

2.5.2 Wear testing

Wear testing was performed on polished samples using ball on disc wear tester (Nanovea tribometer). The nanovea tribometer has a rotating sample holder stage along with a steady vertical ball holder. The ball is fixed in the holder with no possible rotation during wear. Two different abrasive balls (Al_2O_3 and Si_3N_4) were used. The ball diameter was 6 mm. Each sample was tested with loads of 5 N, 10 N, and 15 N at uniform rotating speed of 150 rpm. The radius of wear track was maintained as 2 mm. Only 3 processing conditions (processing 4, 5, and 6) out of six were selected for the wear testing. The physical and mechanical properties of alumina and silicon nitride balls are listed in the Table 2.4. The similar wear testing was performed on an as-received plate to compare the results.

Table 2.4 Mechanical and physical properties of balls used for wear testing.

Ball material	Hardness (HV)	Density (g/cc)	Young's modulus (GPa)
Alumina (Al_2O_3)	1913	3.92	340
Silicon Nitride (Si_3N_4)	1668	3.23	300

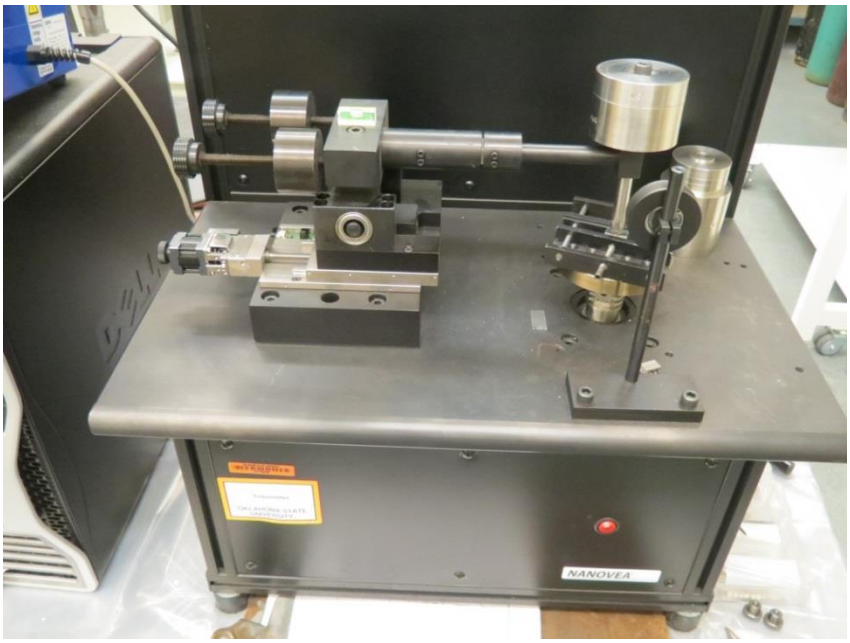

Figure 2.12 Tribometer.

The wear of a sample was carried out continuously for 60 min and the coefficient of friction data was recorded during the entire test. The test was repeated three times for each processing condition at 5N, 10N, and 15N loads, and the average value at each load is mentioned. For the wear rate calculation, after each coefficient of friction test the worn sample surface along with the wear track was scanned with the Nanovea laser profilometer. The 2-dimensional image of the sample wear track was extracted with the help of professional software package (3-D, Nanovea). The area of the wear track is calculated with the 2-D profile analysis tool and wear rate is

calculated by feeding the area value to Nanovea tribometer software. The ball was analyzed under SEM after every wear test. For volume loss data, the weight of the sample was recorded after every 10 minutes of wear testing using precision (Delta Range XD204, Mettler Toledo). The test was not restarted after halt. For the next reading the sample surface was polished, and the test was run for additional 10 minutes with a new ball.

For the detailed analysis of the wear mechanisms, SEM analysis was performed on the wear track and balls. EDS mapping was also performed on the wear track and worn surface of the ball to understand the wear mechanisms.

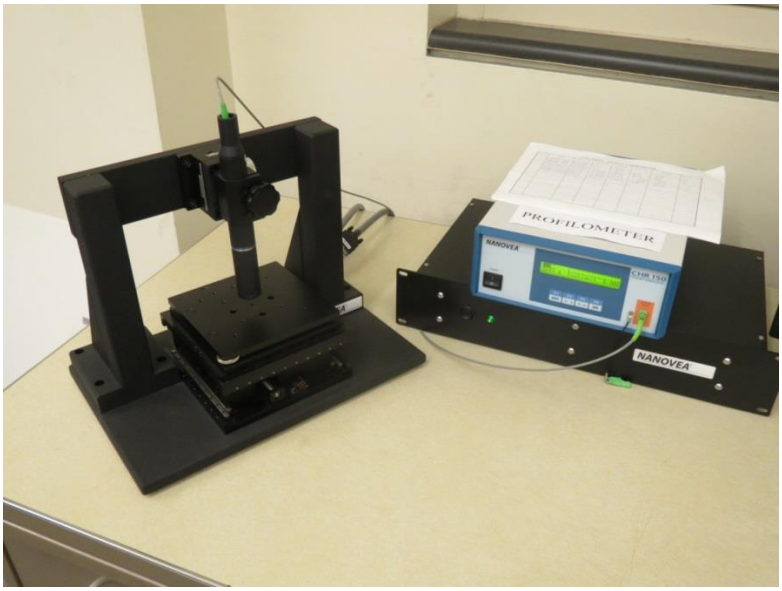

Figure 2.13 Laser profilometer.

CHAPTER III

RESULTS AND DISCUSSION

3.1 Microstructural characterization of as-received modified 9Cr-1Mo plate

The SEM image of an as-received modified 9Cr-1Mo steel plate is as shown in Fig. 3.1. The microstructure of an as-received modified 9Cr-1Mo steel plate contains carbides (white) distributed in the ferrite matrix (grey). According to the line intercept method, the average grain size of the modified 9Cr-1Mo steel plate is ~25 μm. Prior austenite grain boundaries are also evident in the microstructure. As the plate is received in the tempered condition, the retained martensite is transformed into ferrite and fine carbides. As explained by Gupta *et al.* [18], the prior austenite grain boundaries and the boundaries of prior martensite laths are the preferred sites for the precipitation of carbides.

Fig. 3.2 shows the distribution of carbides in the modified 9Cr-1Mo steel microstructure. There are two different types of carbides observed in the microstructure. The carbides precipitated at the prior austenite grain boundaries are coarse in size and are of the type $M_{23}C_6$, where M can be Fe or Cr. The carbides precipitated at the prior boundaries of the martensite laths and throughout in the microstructure are fine and are of the type M_2C and M_6C, where M can be V or Nb [34, 58, 59]. These distributed carbides form sub grain structures. As discussed earlier,

the coarse and fine carbides are evident in the microstructure. Hence the addition of V and Nb in the steel promotes the formation of fine carbides and strengthens the steel. Fig. 3.3 shows the x-ray diffraction analysis of an as-received modified 9Cr-1Mo plate.

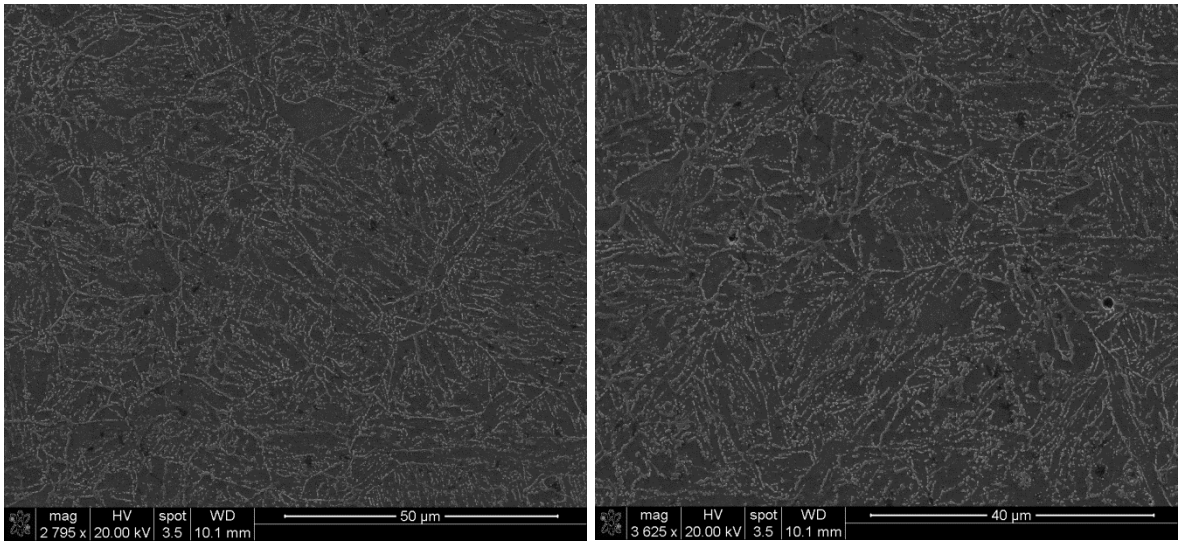

Figure 3.1 SEM image of as-received modified 9Cr-1Mo steel plate etched with 2% nital.

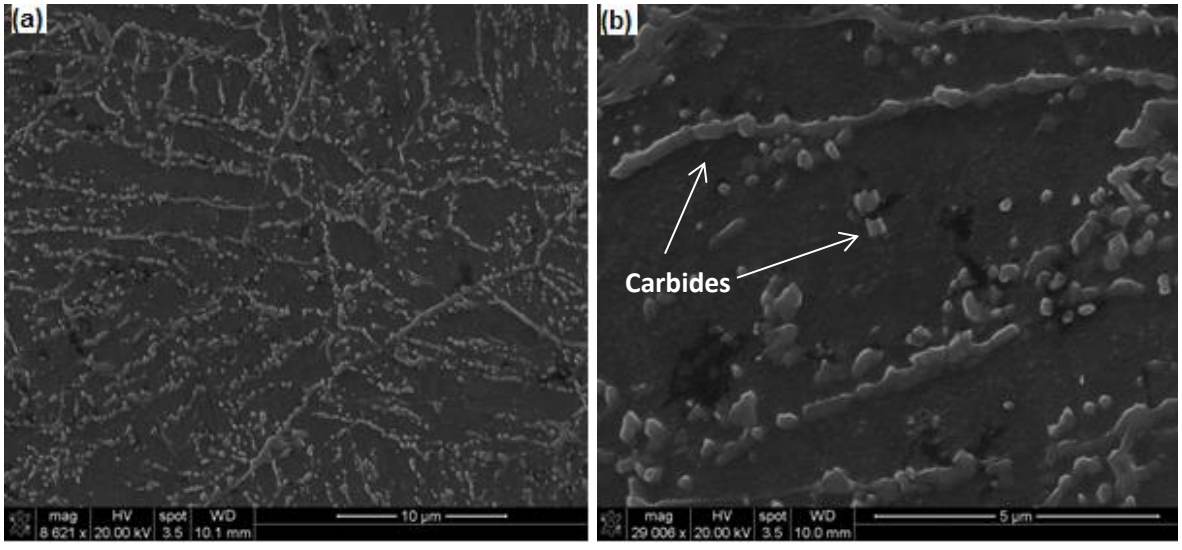

Figure 3.2 Distribution of carbides in as-received modified 9Cr-1Mo steel plate.

The peaks are identified and labeled after comparison with the standard x-ray diffraction software database file as α-iron and Fe-Cr solid solution. The x-ray diffraction peak positions exactly match with the peak positions obtained in the literature studied on modified 9Cr-1Mo steel [27, 34]. As reported by Foley [34], the carbides are not detected in our XRD analysis as the amount of carbides seems to be very low to be detected under XRD scanning.

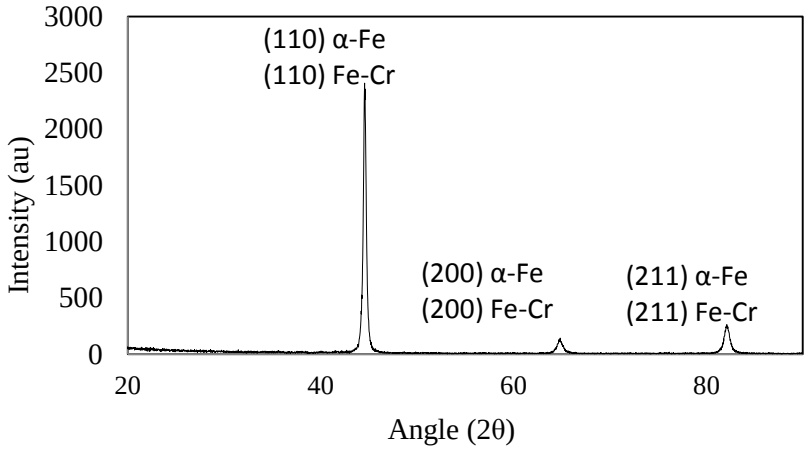

Figure 3.3 X-ray diffraction analysis of modified 9Cr-1Mo steel plate.

3.2 Characterization of ball milled powder

The SEM of the drilled chips and ball milled powder was performed. Fig. 3.4 shows the morphology of as-cleaned modified 9Cr-1Mo chips before the ball milling. The individual chips were discontinuous, short and non fibrous. The chips were 3-4 mm long with 1-2 mm in breadth. The scale like machining marks are evident on the surface of each chip.

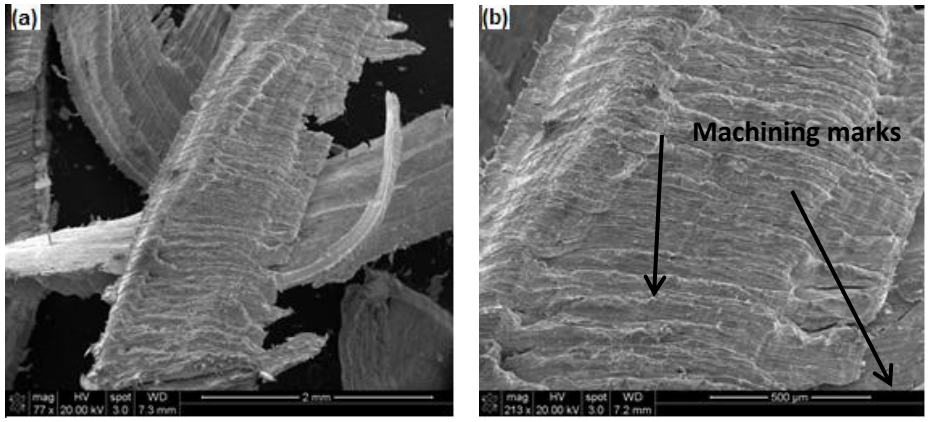

Figure 3.4 SEM images of modified 9Cr-1Mo steel chips.

As discussed in previous sections, the morphologies of the mied powder particles showed the typical characteristics of a ductile material. Fig. 3.5 shows the SEM images of powder particles ball milled for 1 h. In the initial phase, the particles get flattened by impact of the balls and cold weld to each other. In this stage, the particles are able to withstand high deformation which results in the increase in strain. Fig. 3.5 (a) and (b) show the large powder particles made up of cold welded flat layers. Fig 3.5 (c) and (d) are the high magnification images of cold welded particles. Fig. 3.6 shows the SEM images of powder particles after 2 h of ball milling. The figure shows that the powder particles are flat in shape resulting from increasing plastic deformation. With the increasing plastic deformation, the particles get hardened and can not withstand further impact. Fig. 3.6 (d) shows the occurrence of cracking because of the hardening of the particles.

Fig. 3.7 shows the SEM images of powder particles ball milled for 4 h. The figure shows the substantial reduction in particle size (Fig. 3.7 (a)). Figure shows the flat and small spherical particles. This indicates that with increasing ball milling time the bigger flat particles break down into smaller fragments. Fig. 3.7 (d) shows a flat particle of the size 10 μm with a crack

propagating through it. Similar to the initial stage of ball milling, the particles are cold welded to each other, but this time at a smaller scale. At the stage when a particle breaks down into the smaller fragments, the microstrain in the particle is relieved. These smaller particles again get cold welded to other smaller particles and a new ball milling cycle starts.

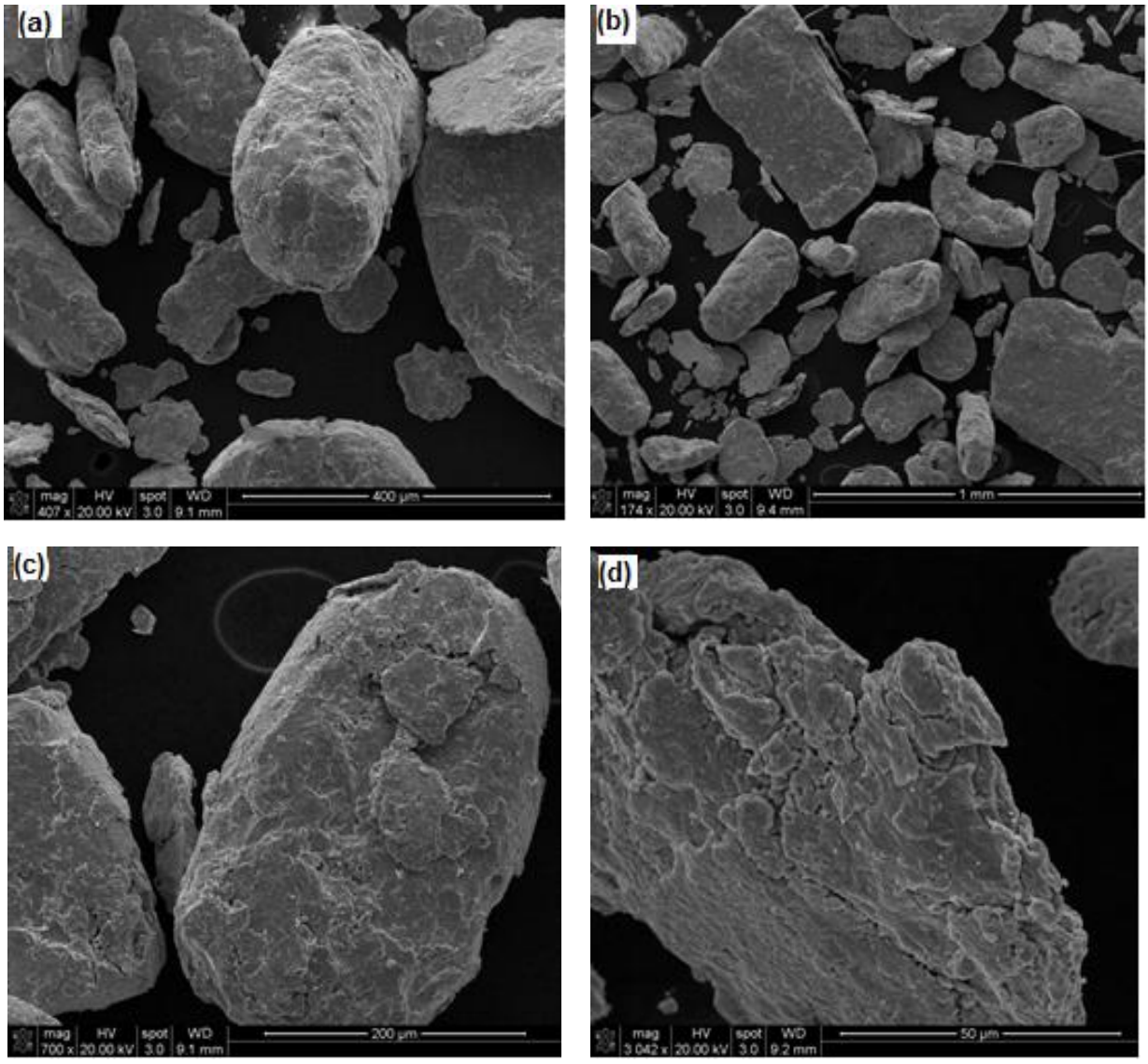

Figure 3.5 SEM images of powder ball milled for 1 h.

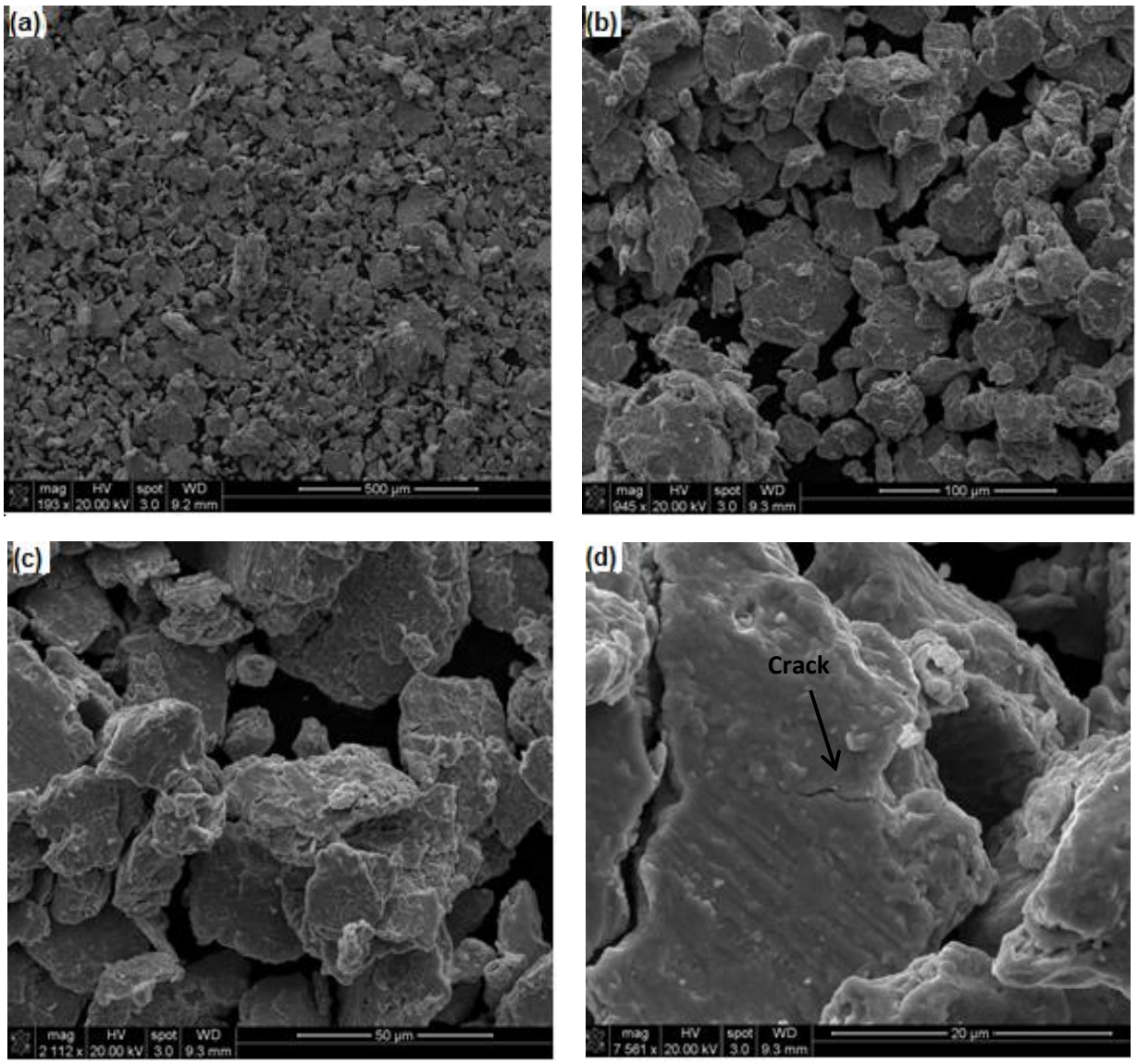

Figure 3.6 SEM images of powder ball milled for 2 h.

The XRD analysis of modified 9Cr-1Mo steel powder produced by ball milling is shown in Fig. 3.8. The broadening of the XRD peaks with increasing ball milling time is evident from the analysis. The intensity of the peaks continuously decreases with ball milling time as it depends depends upon the number of overlapping crystal planes of the same orientation.

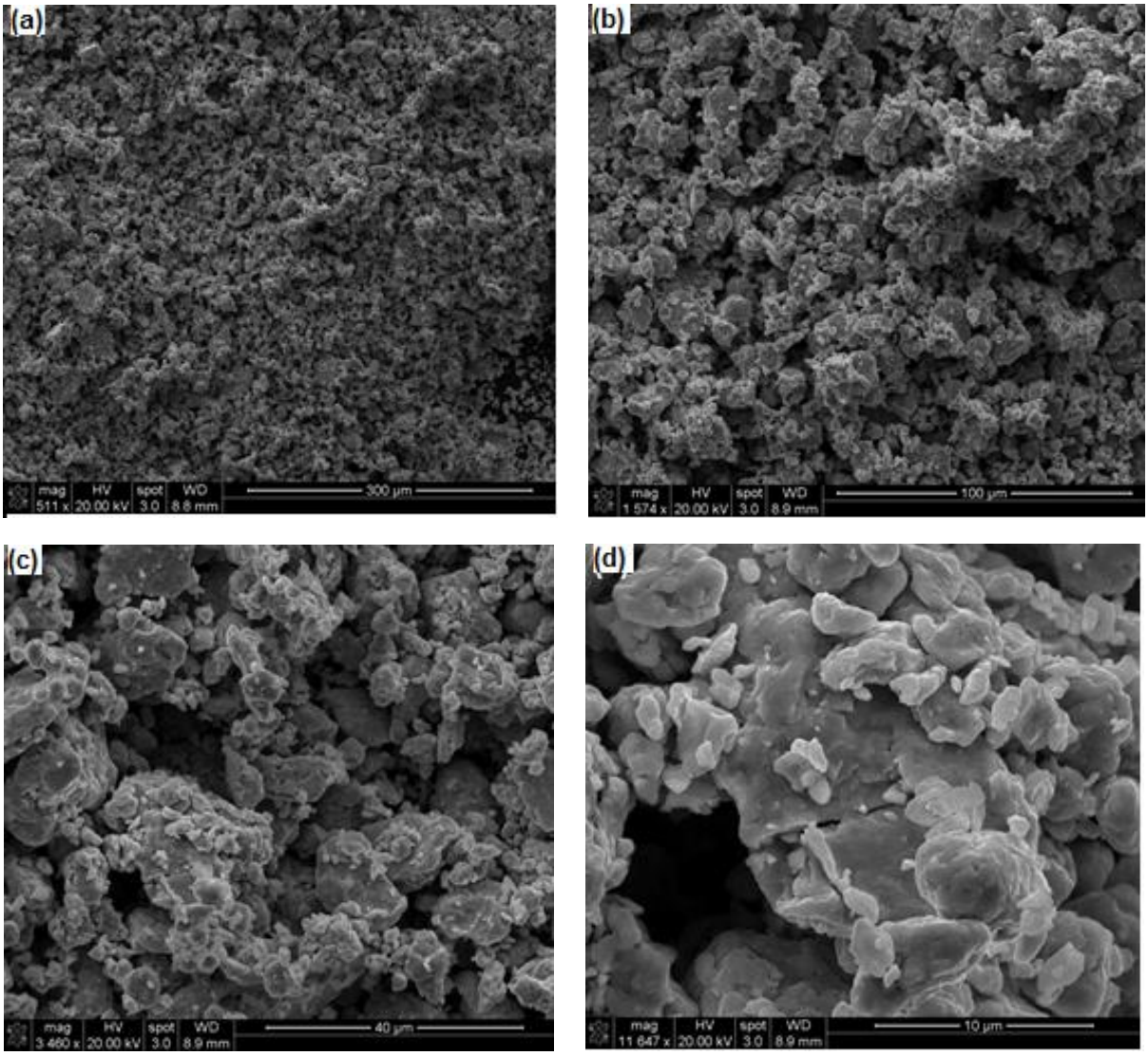

Figure 3.7 SEM images of powder ball milled for 4 h.

As the ball milling time increases the order of a preferred plane orientation in crystallites is disturbed which is indicated by the decrease in the intensities of XRD peaks. This also means that the powder will have crystallite planes with many orientations. As explained by Mitchell *et al.* [60] the broadening of an XRD peak is caused by the decrease in the crystallite size or increase in the microstrain in crystallites.

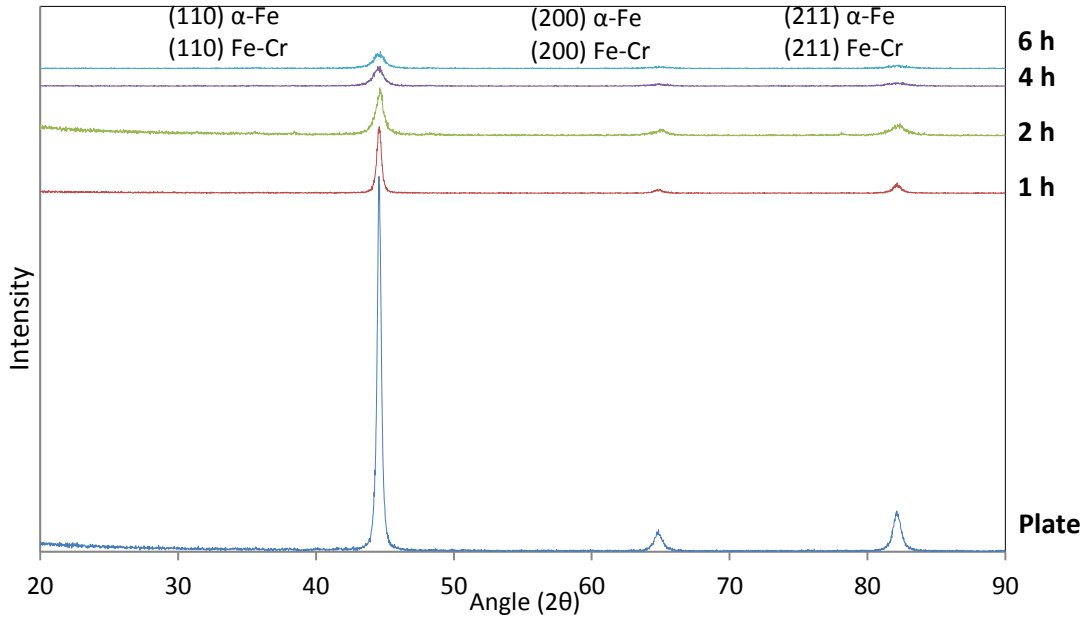

Figure 3.8 X-ray diffraction analysis of ball milled powder.

3.2.1 Line integral breadth analysis

As explained by Guo *et al.* in their work [60] the line integral breadth analysis proposed by Scherrer is capable of calculating both the crystallite size and microstrain. In this analysis, the peak profiles in the XRD pattern, are assumed to be of Gaussian type. Then the full width half maximum (FWHM) of the profile β is given by:

$$\beta^2 = \left(\frac{k\,\lambda}{D\,cos\,\theta}\right)^2 + (4\,e\tan\theta)^2, \quad \text{.....(3.1)}$$

where k is a Scherrer factor ~ 1, λ is a wavelength of CuK_α radiation 1.54178 Å, θ is a half the angular position of a peak, D is the crystallite size, and e is the microstrain developed in the crystallite. The equation (3.1) can be rearranged as,

$$\frac{\beta^2 cos^2\theta}{\lambda^2} = \frac{1}{D^2} + \left(\frac{sin^2\theta}{\lambda^2}\right) 16e^2 \quad \text{..... (3.2)}$$

The equation (3.2) is similar to the equation of straight line $y = mx + c$. Hence if $\left(\frac{\beta^2 cos^2\theta}{\lambda^2}\right)$ is plotted with $\left(\frac{sin^2\theta}{\lambda^2}\right)$, the term $\left(\frac{1}{D^2}\right)$ is the intercept of the line on y-axis and $(16e^2)$ is the slope of the straight line. Hence after plotting the straight line for each pattern we can get the value of crystallite size and microstrain in the crystallite.

Example calculation: An example calculation of a line breadth integral analysis of an x-ray diffraction pattern of a powder ball milled for 1 h is discussed here. The FWHM for each peak was calculated by fitting a Gaussian curve for each peak. The curve fitting was performed with the help of OriginPro 8.6 64 bit software. The FWHM values calculated for each peak are listed in Table 3.1.

Table 3.1 Full width half maximum (FWHM) of peaks for 1 h ball milled powder.

Peak position (2θ)/(Indices)	**45 (110)**	**65 (200)**	**82 (211)**
FWHM	0.46429	0.97073	0.01694

From the information the parameters required for plotting the straight line are calculated and listed in Table 3.2. From the parameters listed in the Table 3.2 the points are plotted and a best fit straight line is fitted through the scatter. The plot of $\left(\frac{\beta^2 cos^2\theta}{\lambda^2}\right)$ is plotted with $\left(\frac{sin^2\theta}{\lambda^2}\right)$, appears to be as shown in Fig. 3.9.

Table 3.2 Parameters for line breadth integral analysis for 1 h ball milled powder.

Peak position	**Wavelength**	**FWHM (β)**		$\left(\frac{\beta^2 cos^2\theta}{\lambda^2}\right)$	$\left(\frac{sin^2\theta}{\lambda^2}\right)$
(θ)	**(λ)**	**(Degrees)**	**(Radians)**		
22.5	0.15406	0.46429	0.0081	0.002361	6.170204
32.5	0.15406	0.97073	0.01694	0.008603	12.16335
41	0.15406	0.89327	0.01559	0.005833	18.13452

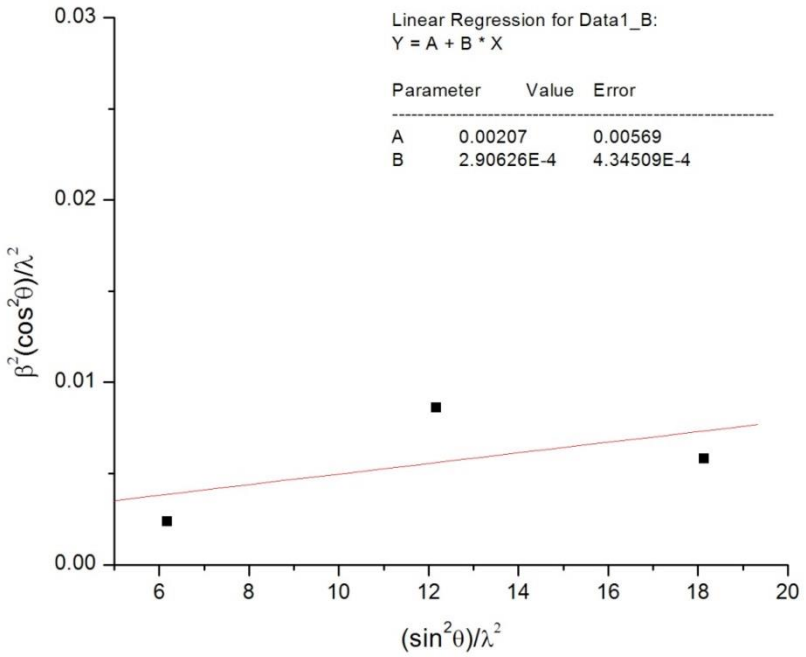

Figure 3.9 Line breadth integral analysis of powder ball milled for 1 h.

From the equation of straigth line the slope of the straight line $(16e^2)$ is 0.0003 and intercept on the y-axis $\left(\frac{1}{D^2}\right)$ is 0.0021. Hence, the crystallite size (D) is 21.82179 nm and microstrain in the crystallite (e) is 0.00433. Similarly, the crystallite size and microstrain values are calculated for x-ray diffration pattern of 2, 4 and 6 h ball milling. The Tables 3.3 to 3.8 enlist the parameters for 2, 4 and 6 h pattern.

Table 3.3 Full width half maximum (FWHM) of peaks for 2 h ball milled powder.

Peak position (2θ)/(Indices)	**45 (110)**	**65 (200)**	**82 (211)**
FWHM	0.67919	1.1452	1.23186

Table 3.4 Parameters for line breadth integral analysis for 2 h ball milled powder.

Peak position (θ)	**Wavelength (λ)**	**FWHM (β)**		$\left(\frac{\beta^2 cos^2\theta}{\lambda^2}\right)$	$\left(\frac{sin^2\theta}{\lambda^2}\right)$
		(Degrees)	**(Radians)**		
22.5	0.15406	0.67919	0.011854	0.005053	6.170204
32.5	0.15406	1.1452	0.019988	0.011973	12.016335
41	0.15406	1.23186	0.0215	0.011093	18.13452

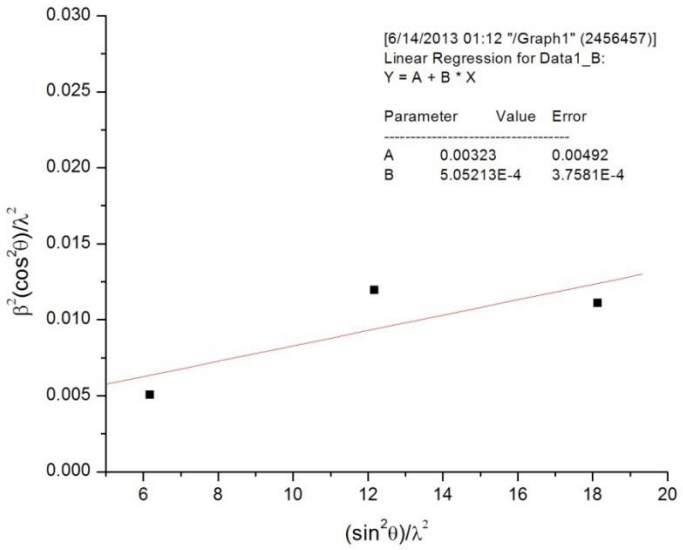

Figure 3.10 Line breadth integral analysis of powder ball milled for 2 h.

Table 3.5 Full width half maximum (FWHM) of peaks for 4 h ball milled powder.

Peak position (2θ)/(Indices)	**45 (110)**	**65 (200)**	**82 (211)**
FWHM	0.87219	1.93482	1.81272

Table 3.6 Parameters for line breadth integral analysis for 4 h ball milled powder.

Peak position (θ)	**Wavelength (λ)**	**FWHM (β) (Degrees)**	**FWHM (β) (Radians)**	$\left(\frac{\beta^2 cos^2\theta}{\lambda^2}\right)$	$\left(\frac{sin^2\theta}{\lambda^2}\right)$
22.5	0.15406	0.87219	0.015223	0.008334	6.170204
32.5	0.15406	1.93482	0.033769	0.034175	12.16335
41	0.15406	1.81272	0.031638	0.024021	18.13452

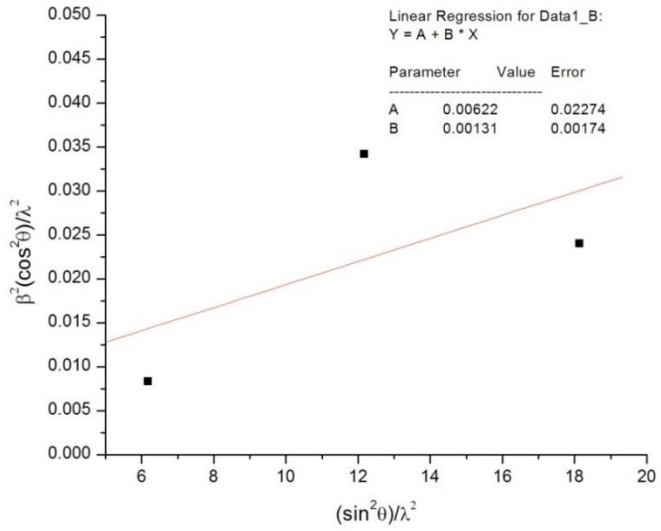

Figure 3.11 Line breadth integral analysis of powder ball milled for 4 h.

Table 3.7 Full width half maximum (FWHM) of peaks for 6 h ball milled powder.

Peak position (2θ)/(Indices)	**45 (110)**	**65 (200)**	**82 (211)**
FWHM	0.87919	1.59432	1.53478

Table 3.8 Line integral breadth analysis parameters for 6 h of ball milling.

Peak position (θ)	**Wavelength (λ)**	**FWHM (β)**		$\left(\frac{\beta^2 cos^2\theta}{\lambda^2}\right)$	$\left(\frac{sin^2\theta}{\lambda^2}\right)$
		(Degrees)	**(Radians)**		
22.5	0.15406	0.87919	0.015345	0.008468	6.170204
32.5	0.15406	1.59432	0.027826	0.023205	12.16335
41	0.15406	1.53478	0.026787	0.01722	18.13452

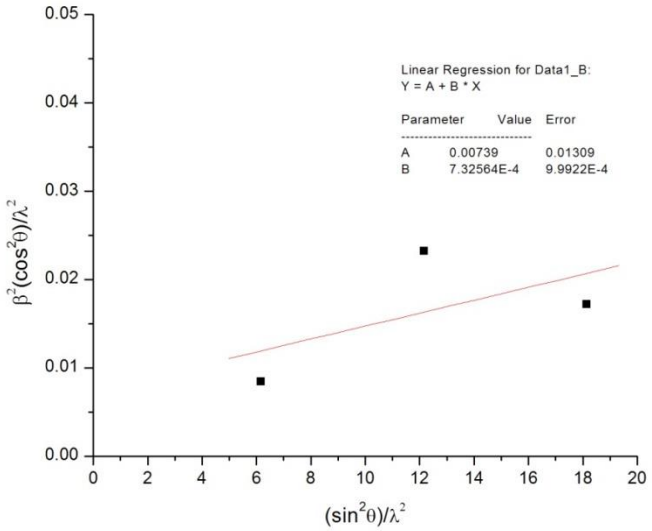

Figure 3.12 Line breadth integral analysis of powder ball milled for 6 h.

Fig. 3.13 shows the variation of a crystalite size and a microstrain developed in the ball milled samples as a function of ball milling time. The analysis shows that the crystallite size decreased rapidly from 23 nm to 13 nm with increasing ball milling time upto first 4 h of the ball milling process. The slope of the curve almost becomes flat after the 4 h of ball milling. Not much change occurred in the crystallite size with further increase in ball milling time. In contrast, the microstrain in the samples increased rapidly from 0.0005 to 0.0010 for the first 4 h of ball milling followed by a sudden decrease.

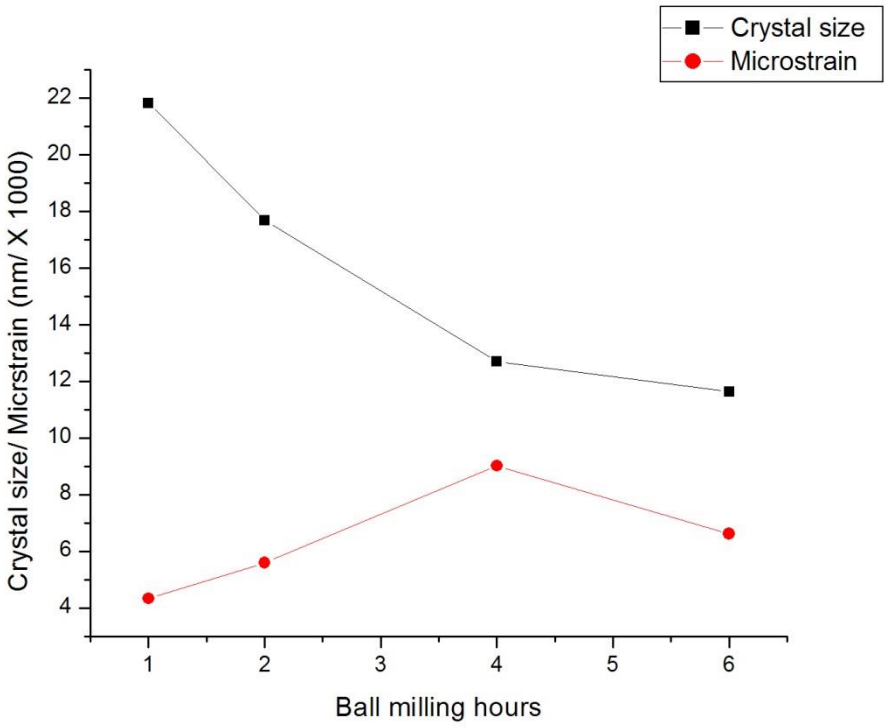

Figure 3.13 XRD data analysis.

The steel particles are ductile in the initial stage of ball milling and capable of accumulating large amount of strain by plastic deformation. This explains the increase in microstrain upto 4 h of ball milling. Eventually as the strain increases and the ultimate strength limit of the material is crossed, the particle breaks down into the small fragments releasing the developed strain. This indicates the start of a new ball milling cycle [43]. As there is no significant decrease observed in the crystallite size after 4 h of ball milling and the decrease in microstrain indicates the start of new ball mill cycle, we used a powder after 4 h of ball milling for our work.

3.2.2 Transmission electron microscopy (TEM)

To verify the crystallite size predicted by the XRD analysis, the TEM analysis of the ball milled powder was performed. Fig. 3.14 shows the TEM images of powder particles resting on the copper grid. Fig 3.14 (a) shows the image of particles clustered together during ball milling to form a cluster 100 nm in size. Individual particles are 20-25 nm in size. Fig. 3.14 (b) shows the image of individual powder particles.

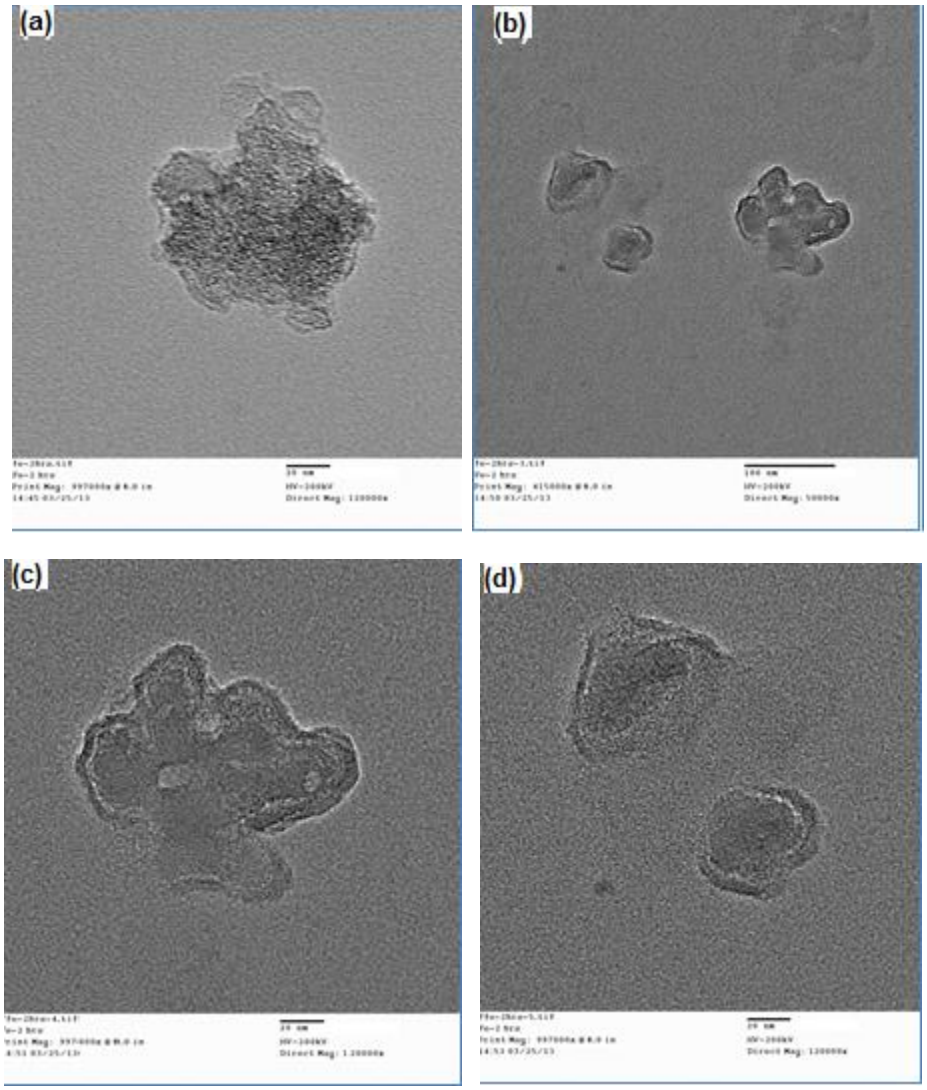

Figure 3.14 TEM images of powder particles ball milled for 4 h.

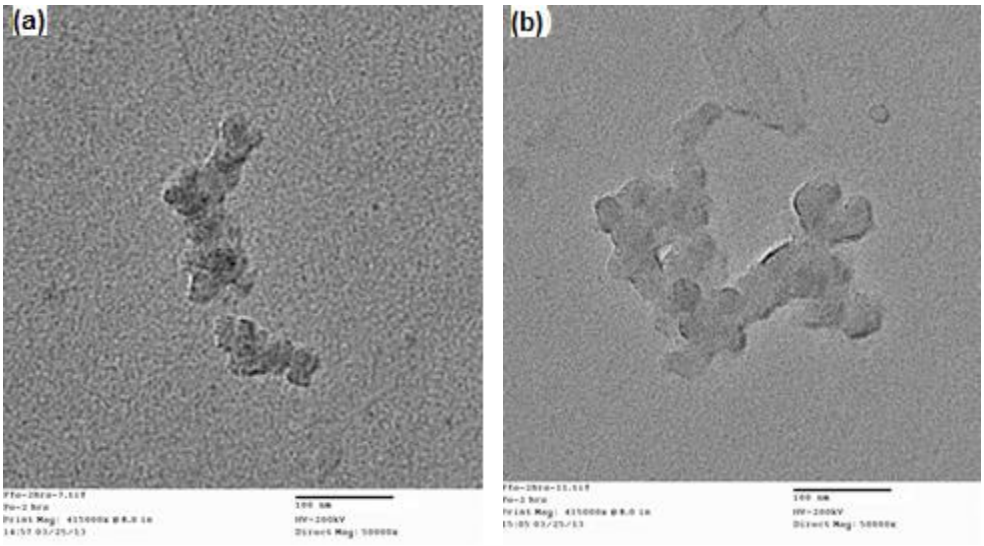

Figure 3.15 TEM image of powder cluster.

Fig. 3.14 (c), (d) are the high magnification images of image 3.14 (b). It clearly shows the presence of the 20-40 nm size particles on the copper grid.Fig. 3.15 shows the images of nanoparticles clustered together. These clusters are 100-150 nm in size with an individual particle ranging from 20-25 nm in size. These TEM images verify the crystallite size predicted from x-ray diffraction analysis.

3.3 Relative density and microstructures of the spark plasma sintered samples

The relative density of modified 9Cr-1Mo steel powder sintered at different temperatures and holding time is shown in Fig. 3.16. The figure clearly indicates that the relative density of the sintered sample is dependant on sintering temperature and holding time. The effect of sintering temperature seems to be more pronounced than the holding time.

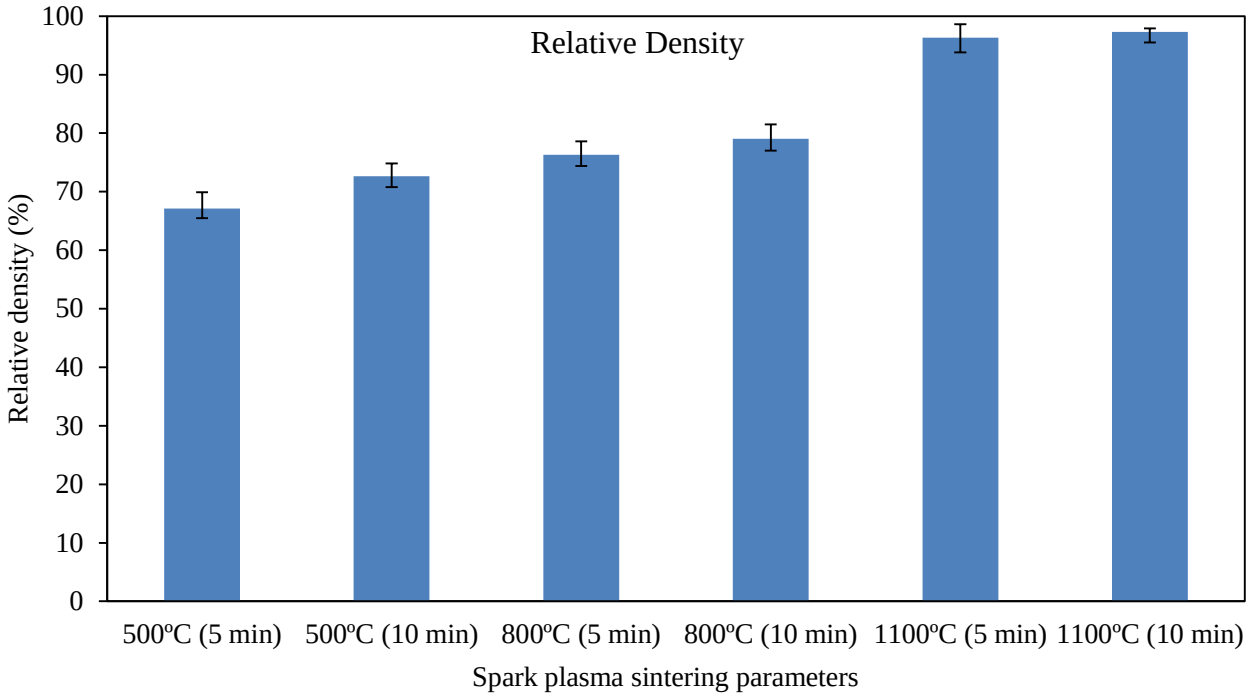

Figure 3.16 Relative density of spark plasma sintered samples.

3.3.2.1 Samples sintered at 500ºC

The relative densities of the samples sintered at 500ºC for 5 min. and 10 min. are 67.1% and 72.65%, respectively. There is about 5.5% increase in the relative density observed by doubling the holding time. At 500ºC, the densification seems to occur only because of the cold welding and plastic deformation of the powder particles at a sintering pressure. Fig. 3.17 shows the microstrcture of the samples sintered at 500ºC for 5 min. As the temperature is lower than haf the melting temperature of steel, the necks at the contact points of particles are not evident. Fig. 3.18 shows the microstructure of the sample sintered at 500ºC for 10 min. As compared to the sample sintered for 5 min. at 500ºC, the porosity in this sample appears to be reduced. Because of the increase in holding time there was more time available for particles to rearrange and cold weld to each other at a moderate temperature.

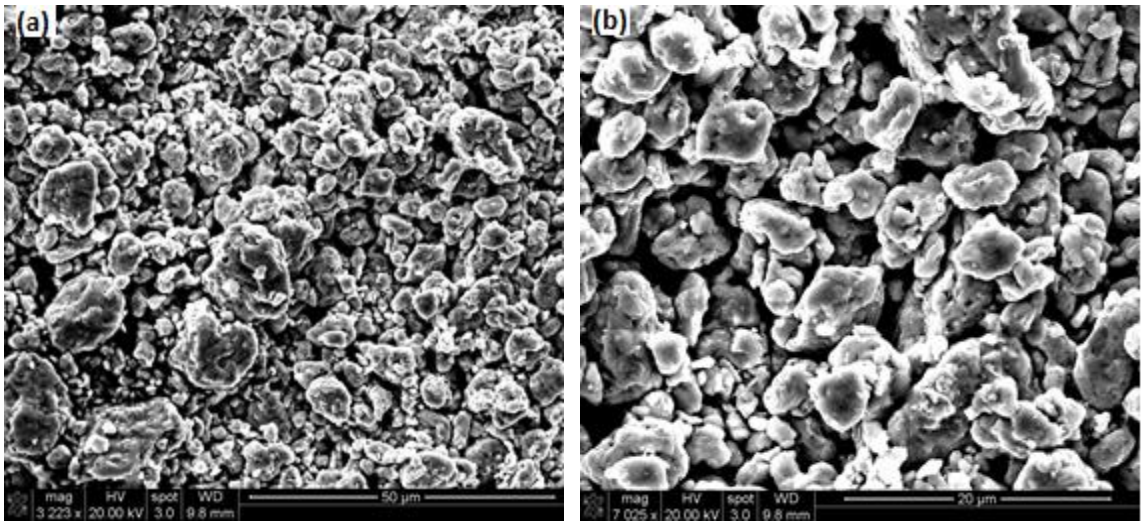

Figure 3.17 SEM images of the samples sintered at 500ºC for 5 min.

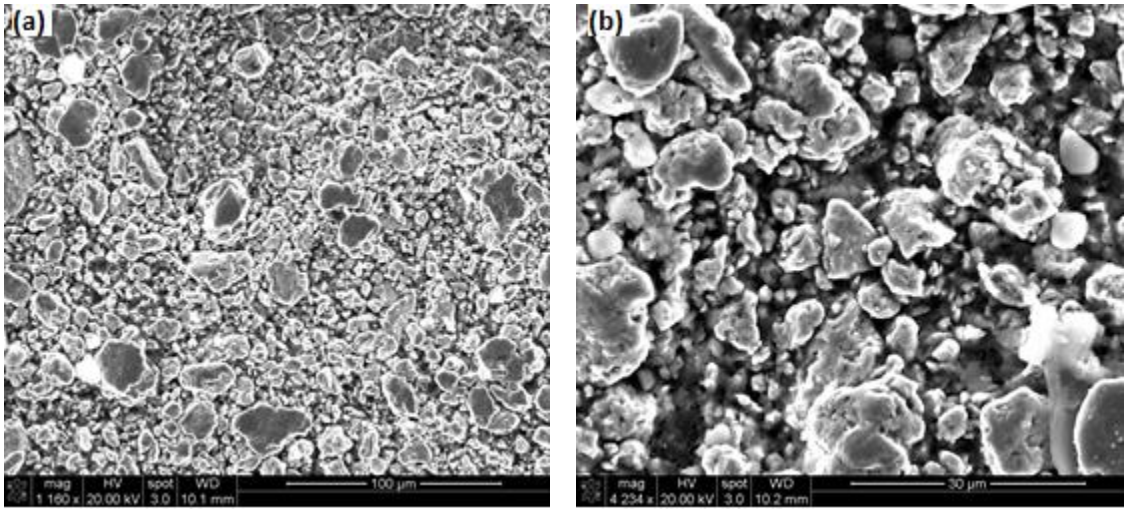

Figure 3.18 SEM images of the samples sintered at 500ºC for 10 min.

The particles in this sample are more deformed and flattened in shape than the sample held for 5 min. Zhang *et al.* [61] reported 89% relative density of the ball milled Fe-0.8 C alloy powder sintered at 500ºC and 70 MPa pressure for 10 min. The high value of density mentioned in their work corresponds to the low melting temperature (~1000ºC) of this alloy.

3.3.2.3 Samples sintered at 800ºC

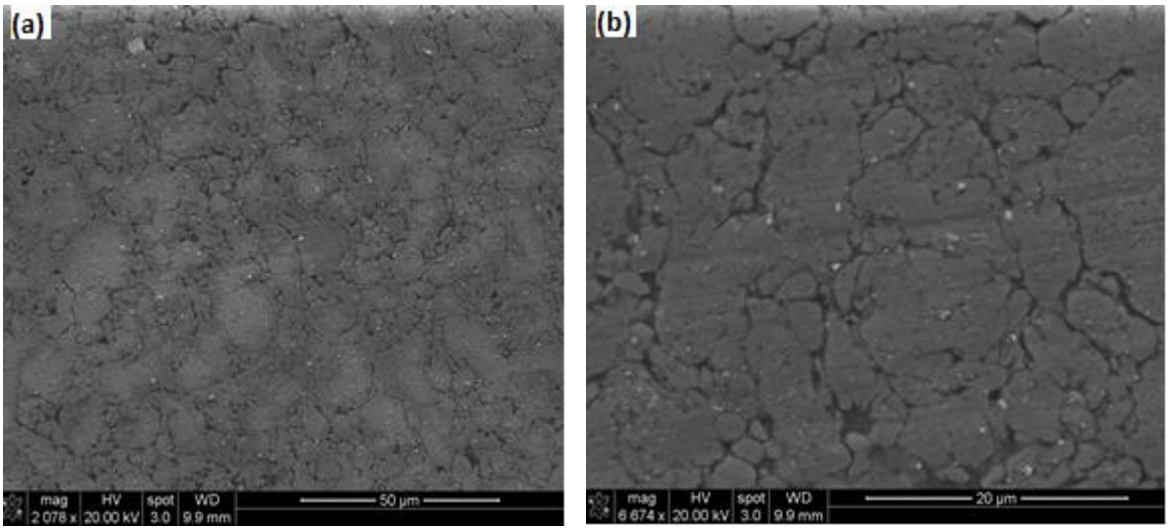

Figure 3.19 SEM images of the samples sintered at 800ºC for 5 min.

The relative densities of the samples sintered at 800ºC for 5 min. and 10 min. are 76.3% and 79%, respectively. For the samples sintered at 800ºC, the relative density increased by 3.3% by doubling the holding time. Fig. 3.19 shows the microstructure of the sample sintered at 800ºC for 5 min. A typical grain structure is visible in the sample sintered at 800ºC. The mean grain size of the sample calculated by a line intercept method is 4.7 µm. At the sintering temperature of 800ºC for 5 min. of the holding time, there is still not clear evidence of necking at the particle contact points. Hong-wei *et al.* [15] reported the relative density as 83% for Fe-16Cr ball milled powder sintered at 800ºC for 5 min. The carbides can be observed in the form of black spots in the grains (Fig. 3.19 (b)). Fig. 3.20 shows the microstructure of a sample sintered at 800ºC for 10 min. In this microsturcture the necking is observed because of the prolonged holding at 800ºC during sintering. The arrows in Fig. 3.20 (b) shows the spots where necks are formed between the particles. Because of the necking occurring at a particle contact points the porosity in the sample decreases. This results in the increase in relative density.

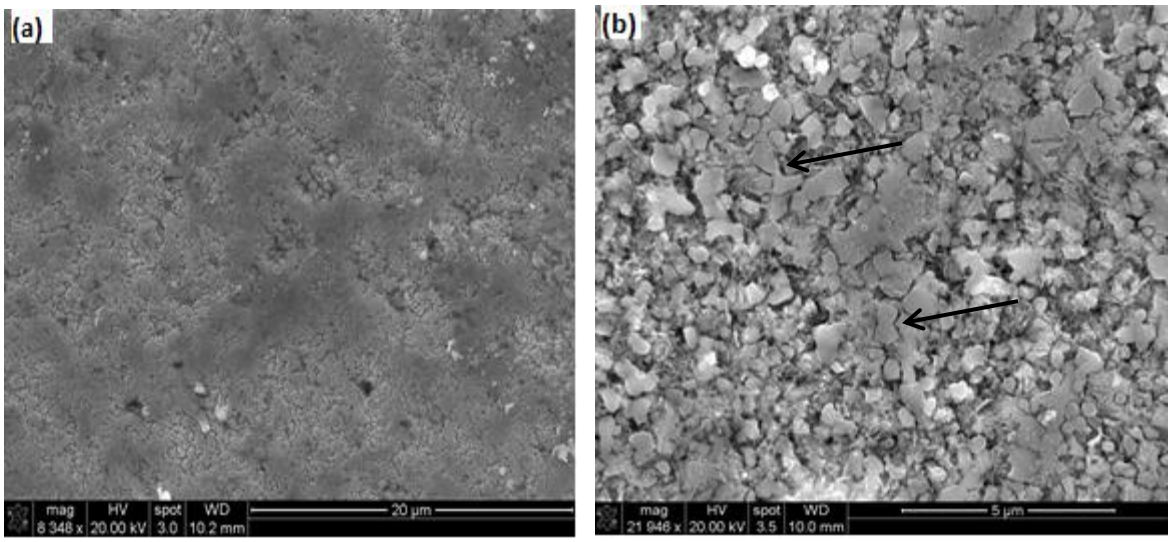

Figure 3.20 SEM images of the samples sintered at 800ºC and 10 min.

3.3.2.5 Sample sintered at 1100ºC

The relative densities of the samples sintered at 1100ºC for 5 min. and 10 min. are 96.3% and 97.3%, respectively. Fig. 3.21 shows the microstructure of the sample sintered at 1100ºC for 5 min. From figure, the microstructure appears to be fully dense with the negligible apparent porosity. Due to high temperatue sintering, the necks can be observed at the particle contact point as shown by arrows in Fig. 3.21. Fig. 3.22 shows the microstructure of a sample sintered at 1100ºC for 10 min. The sample appears to be fully dense with almost no appearance of porosity. The black spots observed on the sample surface are the artifacts due to the overetching of the sample with 2% nital. Because of high temperature and long holding time a necking between the particles is clearly evident. Some evidence of melting was observed due to the prolonged holding at 1100ºC which was absent in the previous samples. Fig 3.22 (d) shows the occurrence of melting at a submicron level. This melting of particles below the melting temperature of an alloy can be attributed to the very high temperatures generated momentarily at the particle contact points.

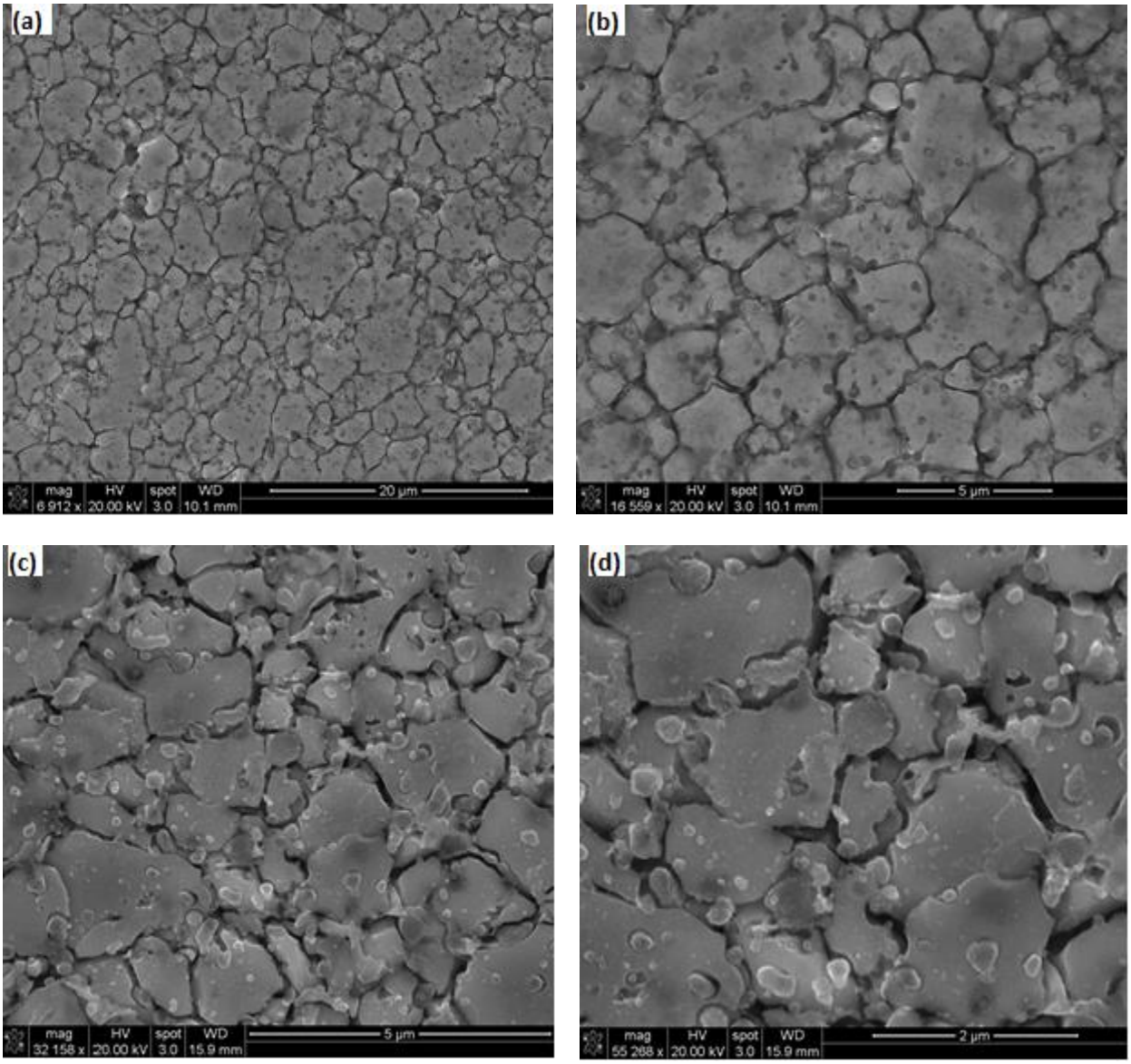

Figure 3.21 SEM images of the samples sintered at 1100ºC for 5 min.

This high temperature is capable of melting the submicron size particles which leads to the localized melting. To characterize the black spots in the microstructure, an EDS scan was performed on the sample that revealed the presence of no unexpected elements. Fig. 3.23 shows the EDS mapping of the sample. After the scan, only Fe, Cr, Mo, and Al were detected which are the elements present in the steel.

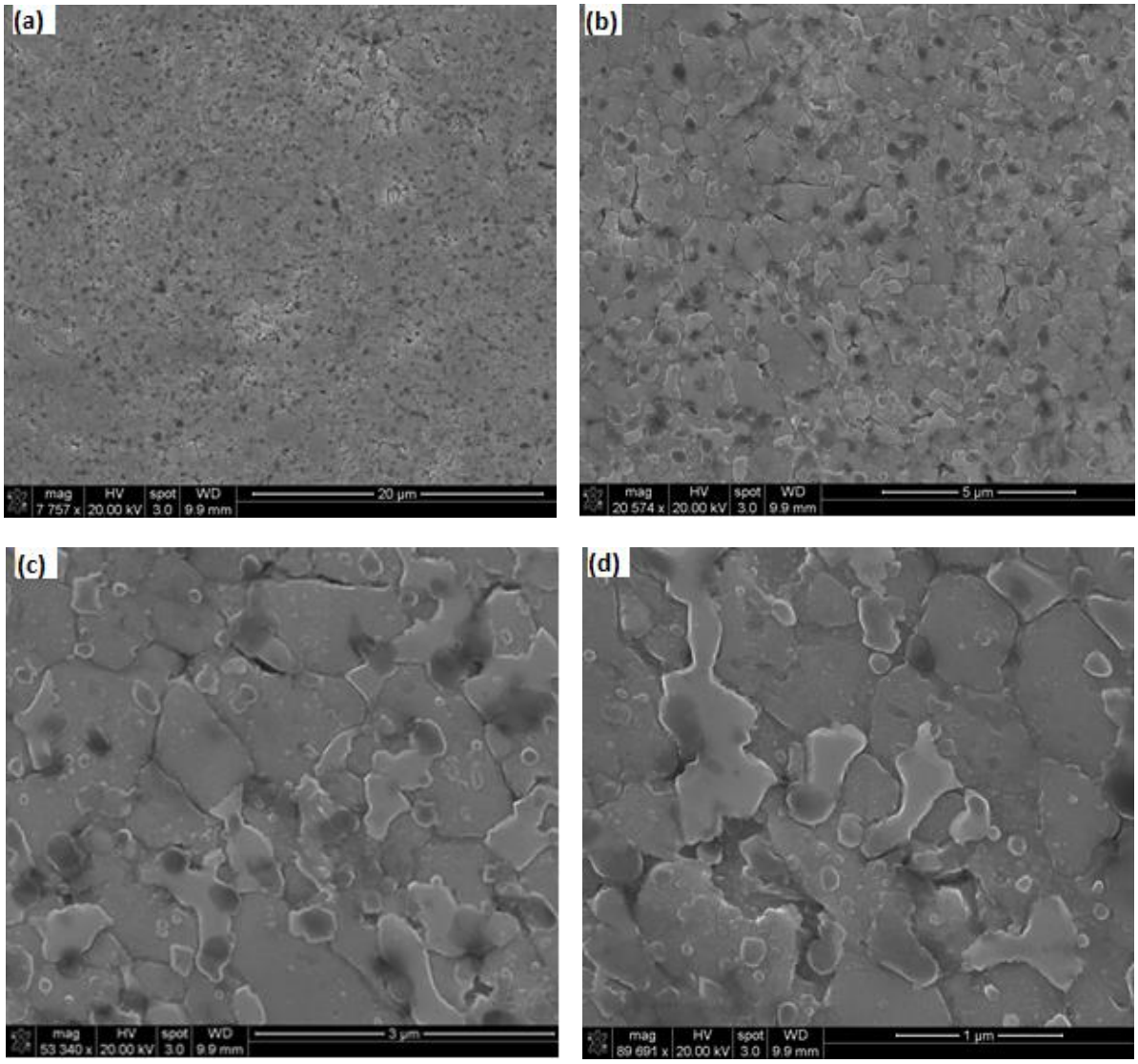

Figure 3.22 SEM images of the samples sintered at 1100ºC for 10 min.

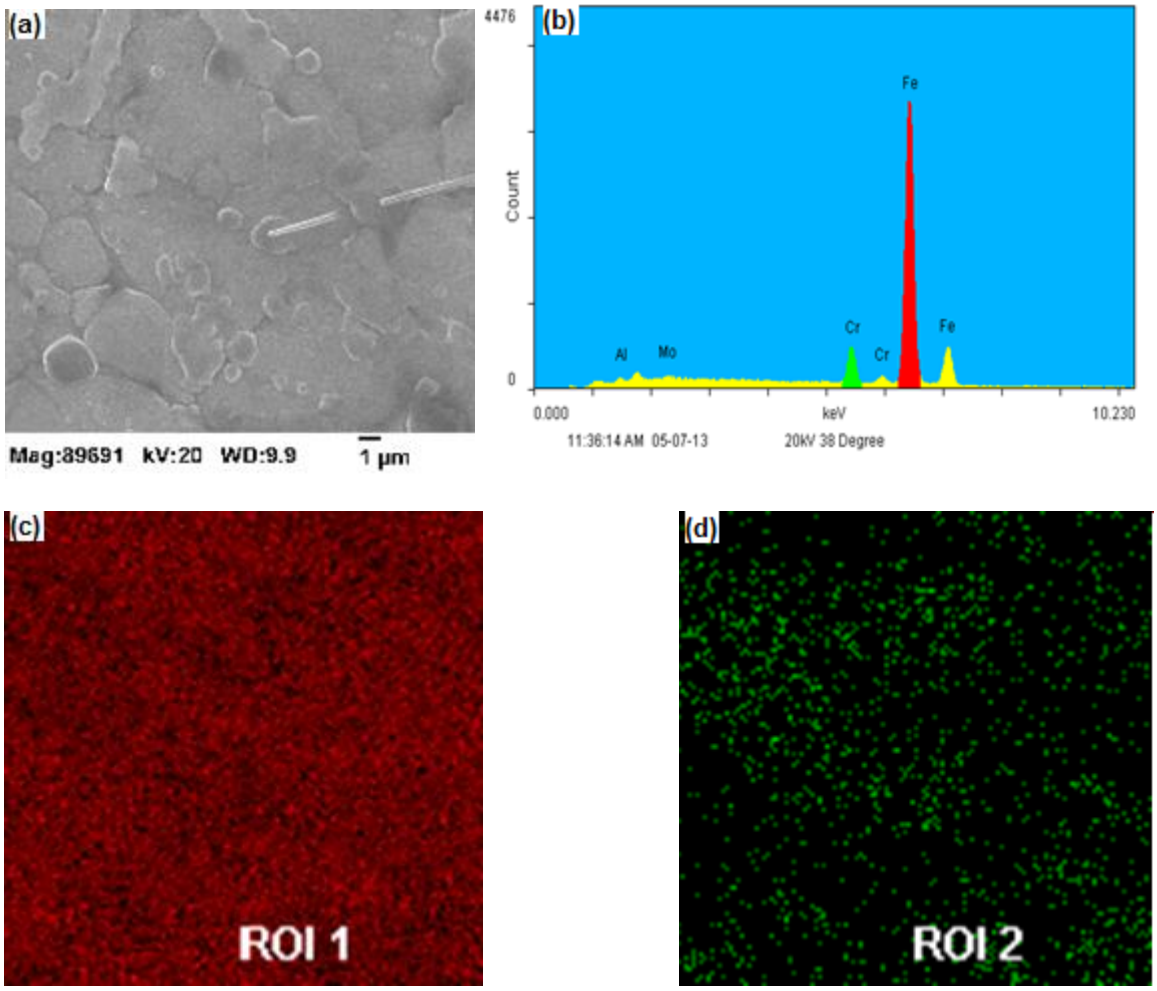

Figure 3.23 EDS analysis of the sample sintered at 1100ºC for 10 min.: (a) SEM image, (b) EDS elemental count, (c) iron mapping, and (d) chromium mapping.

3.4 Microhardness of the spark plasma sintered samples

The microhardness of the spark plasma sintered samples at different sintering temperatures and the holding time is shown in Fig. 3.24. The microhardness value was found to be increasing with the increase in the sintering temperature as well as holding time for a particular temperature.

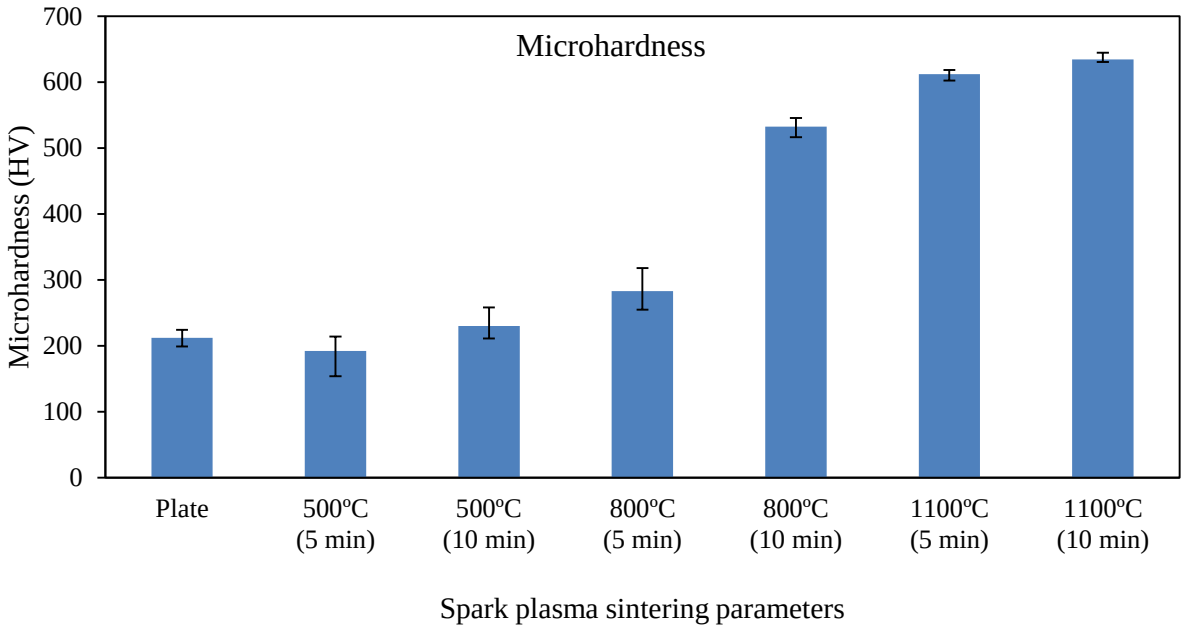

Figure 3.24 Microhardness of the spark plasma sintered samples.

With the increasing sintering temperature the microhardness value increased to about 634 HV at 1100ºC as compared to 212 HV of an as-received plate. The holding time at a particular temperature does not significantly affect the microhardness value except for the sample sintered at 800ºC. The sample sintered at 500ºC for 5 min. shows a lower microhardness value than the as-received plate. When the holding time is doubled at 500ºC, the microhardness value was found to be increased by 19.7%. The samples sintered at 800ºC for 5 min. and 10 min. have microhardness values higher than the microhardness of an as-received plate. The values are found to be 283 HV and 533 HV for 5 min. and 10 min. holding time, respectively. An increase of 88% in the microhardness value is observed by doubling the holding time at 800ºC. The samples sintered at 1100ºC for 5 min. and 10 min. have microhardness 612.25 HVand 634.52 HV respectively. At 1100ºC the microhardness value does not change significantly with doubling the holding time.

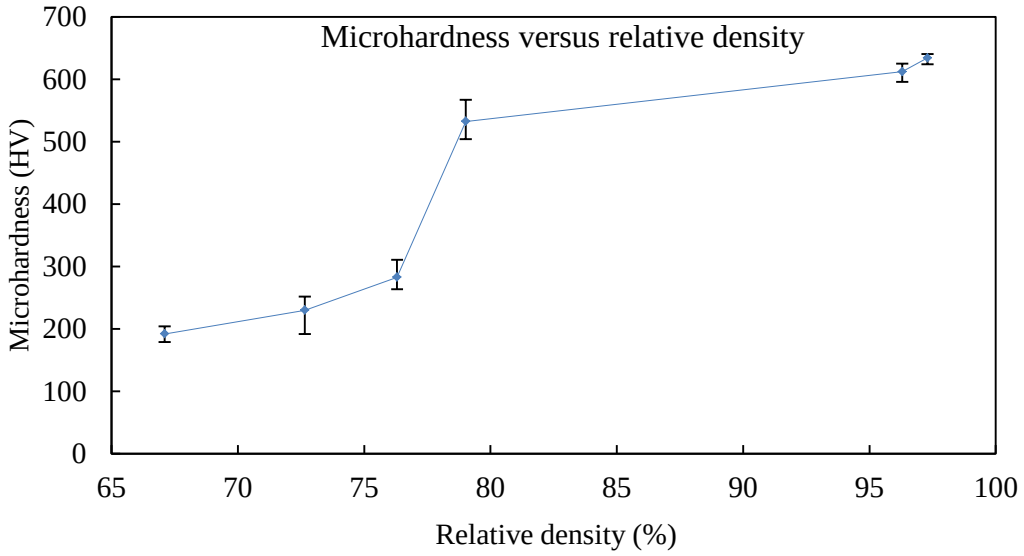

Figure 3.25 Microhardness versus relative density of spark plasma sintered samples.

Fig. 3.25 shows the variation of microhardness with the relative density of the sample. It can be clearly seen that the microhardness of a sample is dependent upon the relative density of the sample. As the relative density increases the particles are more densely packed and resist the plastic deformation. A sample with a smaller grain size contains more grain boundaries. The dislocation movement that causes the plastic deformation is hindered at the grain boundaries. This resistance to the dislocation motion is enhanced with increasing number of grain boundaries in a sample. Hence, the microhardness of the sample, which is a measure of resistance to plastic deformation, increases with the decrease in grain size. This resistance to the dislocation motion is also assisted by the precipitated carbides in the ferrite grains. These carbides pin the dislocations and hinder further dislocation movement.

3.5 Wear analysis

Before proceeding to the detailed wear analysis of the spark plasma sintered samples, wear weight loss experiments were performed. The samples along with the as-received plate were slid with an alumina ball for 60 min. at a 10 N load. The cumulative weight loss of the samples due to wear is plotted with the wear test time. Fig. 3.26 and 3.27 show the weight loss trend for the samples and plate. From Fig. 3.26, it can be seen that the weight loss of the as-received plate is negligible as compared to the weight loss of the samples sintered at 500°C. The sample with the holding time of 5 min. showed the highest weight loss due to wearing with the alumina ball. This high magnitude of weight loss in the samples sintered at 500°C can be attributed to the low relative density of the samples.

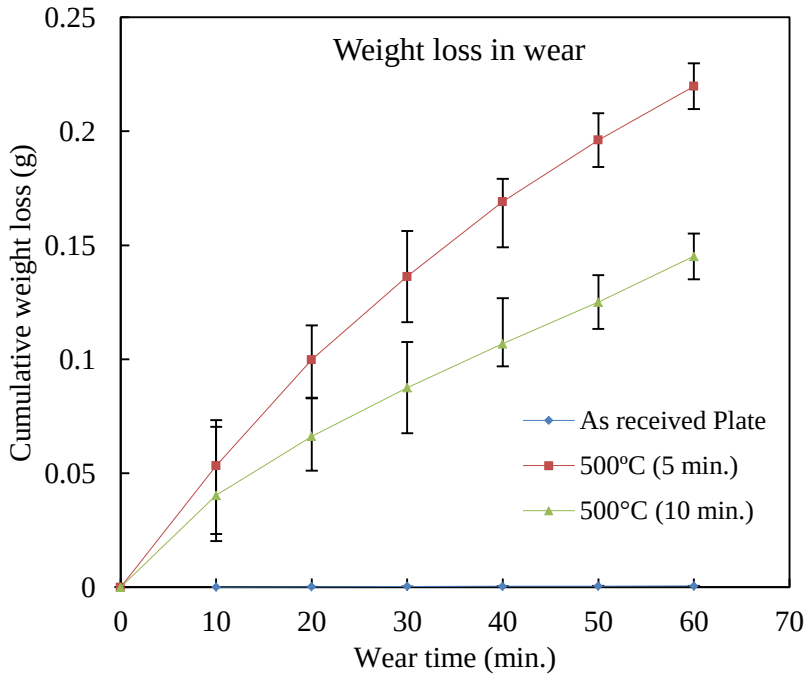

Figure 3.26 Cumulative weight loss of the as-received plate and the samples sintered at 500°C.

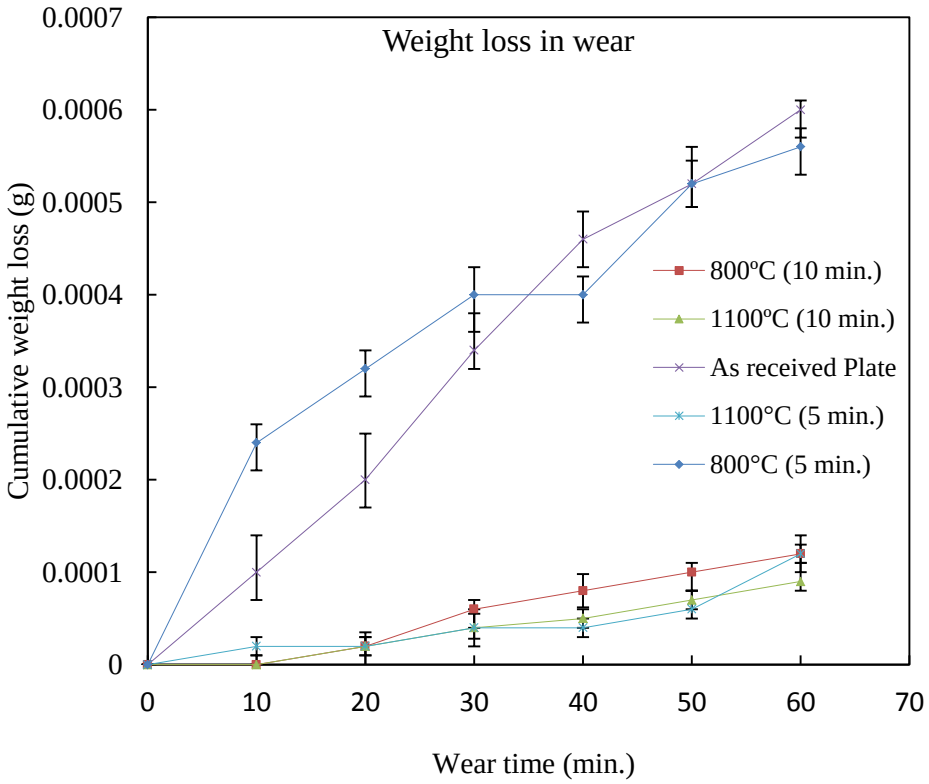

Figure 3.27 Cumulative weight loss of the as-received plate, the samples sintered at 800°C, and 1100°C.

From Fig. 3.27, it can be observed that the as-received plate sample shows the continuous and maximum weight loss while sliding with an alumina ball. The sample sintered at 1100ºC for 10 min. shows the lowest weight loss among all the sintered samples. This reduction in weight loss can be attributed to the highest relative density and high hardness of the sintered sample.

The sample sintered at 800°C for 5 min. shows a weight loss trend similar to the as-received plate. At the initial stage the slope of the weight loss line for this sample is higher than the as-received plate. The sample sintered at 800ºC for 10 min. showed negligible weight loss for the first 10 min. of sliding. This can be attributed to the time required for the coefficient of friction to reach its highest and stable value. After 10 min. the sample showed continuous wear weight loss. The samples sintered at high sintering temperatures undergo weight loss in an

alternate 10 min. time period. This can be explained as the 10 min. of sliding with alumina ball is not sufficient to cause a measurable weight loss in the samples. Hence the samples sintered at high temperature seem to have best wear resistance among tested samples. This can be attributed to the high compact density and hardness achieved by sintering at 1100º C.

For the detailed wear analysis only the samples that showed lower cumulative weight loss than the as-received plate were selected. Hence, further wear analysis the three processing conditions, 800°C (10 min.) and 1100°C (5 min. and 10 min.) were used. The wear behavior of these three samples is compared with behavior of the as-received plate. The wear analysis was carried out with alumina and silicon nitride balls.

3.5.1 Wear analysis with alumina (Al_2O_3) ball

The dry sliding of the alumina ball on the steel samples showed a typical abrasive wear mechanism. During the wear process, the alumina ball deeply grooves the steel samples and produces the highest wear rate. At the initial stage the alumina ball completely abrades the steel sample. At the later stage, a large amount of debris is formed with increasing wear. Because of no lubrication, the debris particles are not washed away and they remain on the wear track. These debris particles participate in further wearing of a steel plate creating a three body wear mechanism. Fig. 3.28 shows the load-velocity maps for the alumina sliding on steel. These debris particles produce microflakes on the steel sample. Fig. 3.29 shows the load-velocity map for wearing of an alumina ball sliding with steel. As per Gautier *et al.* [62] the wearing of an alumina ball for our load-velocity combination (15 N, 0.03 m/s) occurs by intergranular fracture.

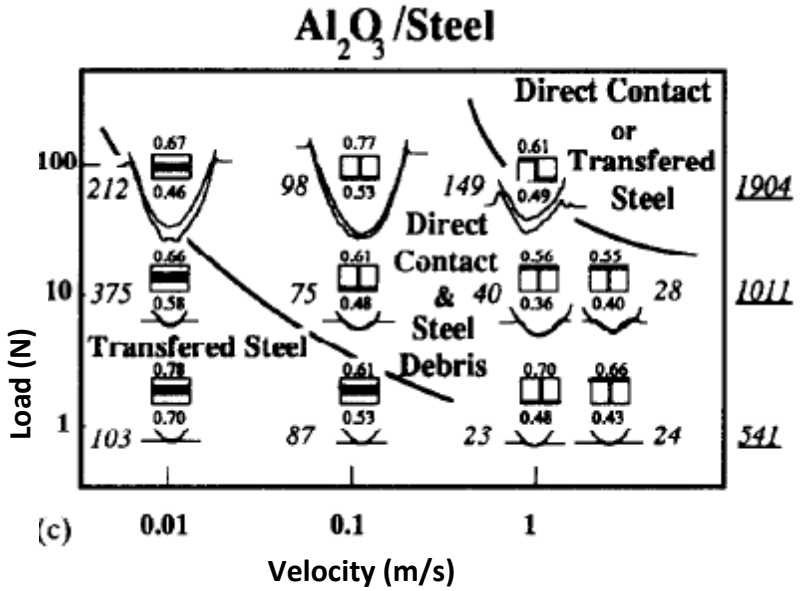

Figure 3.28 Load versus velocity maps for wear of steel by alumina ball (Reprinted from [63] with a permission of the publisher).

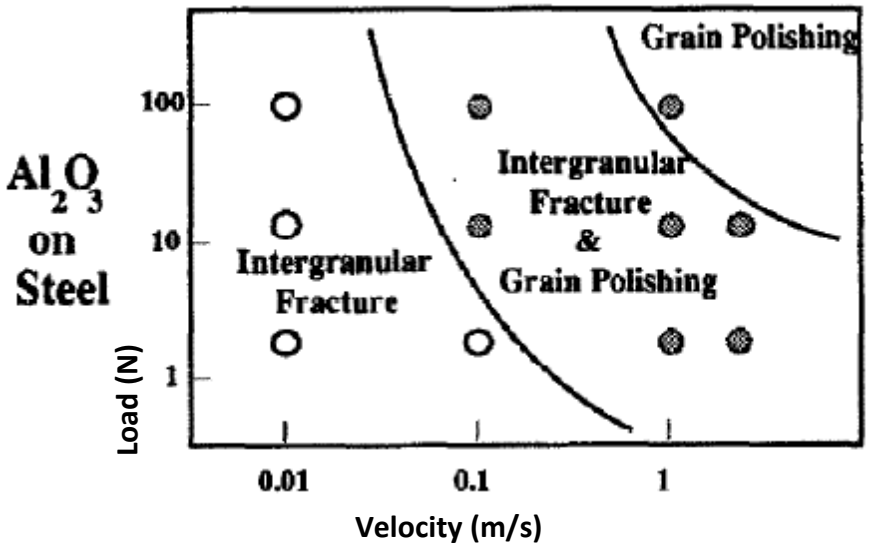

Figure 3.29 Load versus velocity map for wearing of an alumina ball sliding with steel (Reprinted from [62] with a permission of the publisher).

3.5.1.1 Coefficient of friction (COF)

The COF data was collected three times for each combination. One representative curve of the COF versus sliding time is plotted here for reference. A trend line in the form of a forth degree polynomial is fitted through each curve for the ease of analysis.

3.5.1.1.1 As-received plate

Fig. 3.30 shows the trend of a COF with the sliding time for the as-received steel plate. For all the three loads the COF jumped to the stable value in the first 2-3 min. of sliding.

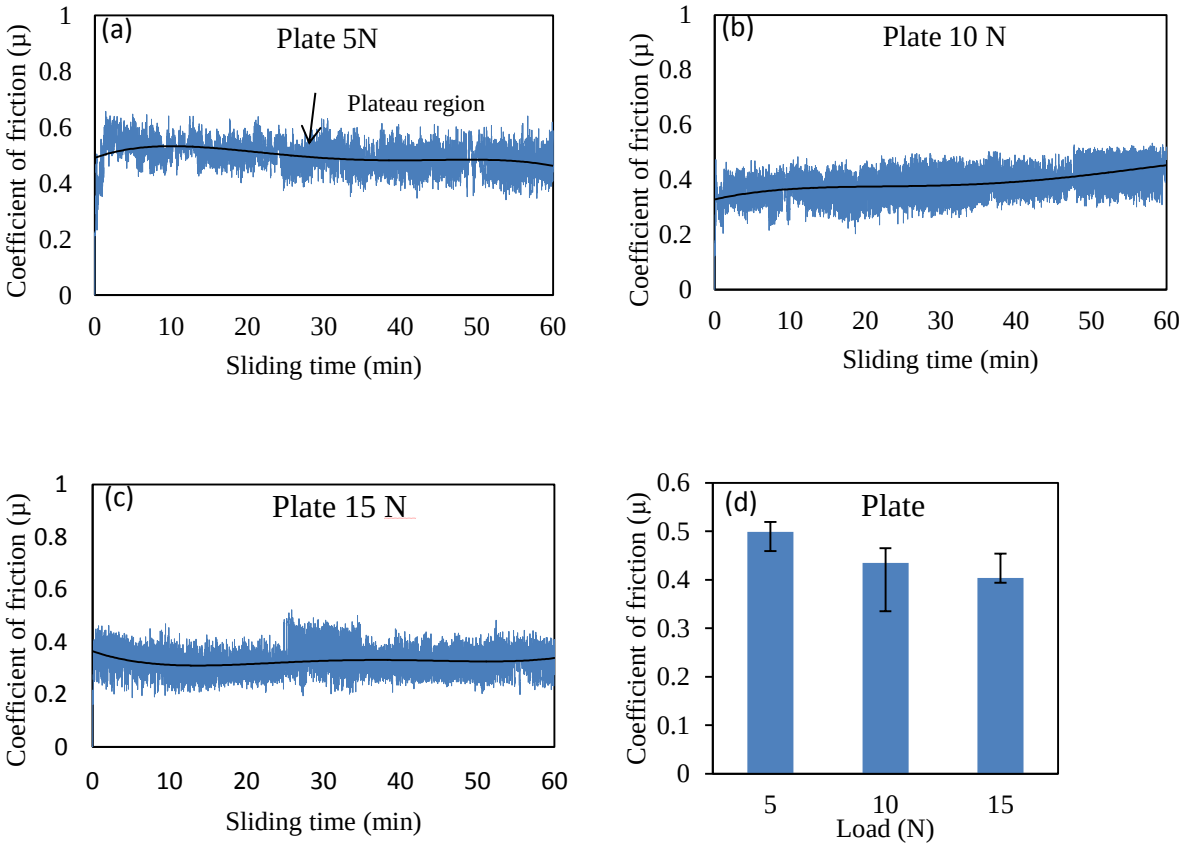

Figure 3.30 COF versus sliding time for as-received steel plate sliding with alumina ball for 60 min. at a: (a) 5 N load, (b) 10 N load, (c) 15 N load, and (d) comparison of COF.

At the later stage, the COF was constant for the remaining sliding on the steel plate. Also the mean value of the COF decreased with an increase in load. The decrease in the COF with an increasing load can be explained by the formation of a large amount of wear debris at the higher loads. At higher loads the steel surface is ploughed by the ceramic ball.

3.5.1.1.2 Sample sintered at 800ºC for 10 min.

Fig. 3.31 shows the trend of the COF for the sample sintered at 800ºC for 10 min. with the alumina ball at different loads. As compared to the as-received plate sample the time elapsed in reaching a stable value by COF is more. Typically 10-15 min. of sliding has occurred before the COF reached its plateau region.

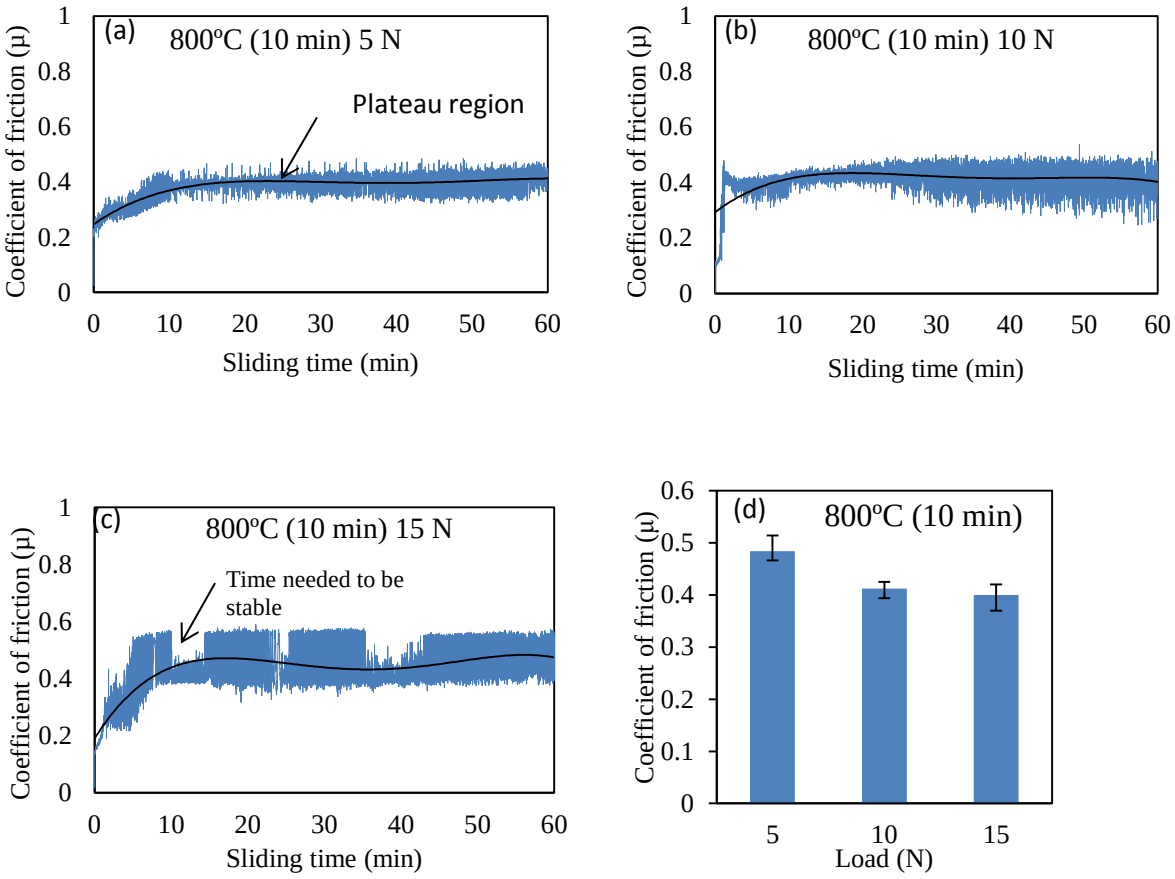

Figure 3.31 COF versus sliding time for sample sintered at 800ºC for 10 min. with alumina ball at a: (a) 5 N load, (b) 10 N load, (c) 15 N load, and (d) comparison of COF.

3.5.1.1.3 Samples sintered at 1100ºC

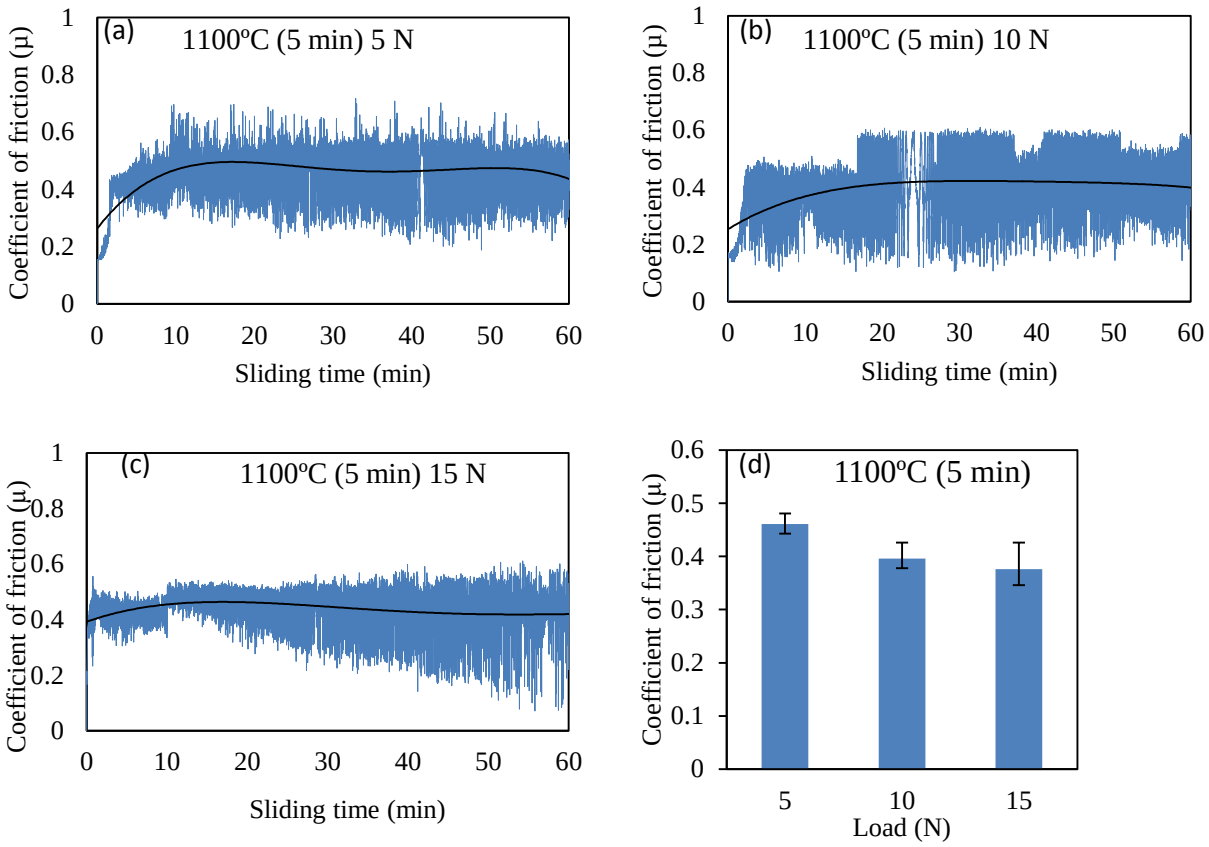

Figure 3.32 COF versus sliding time for sample sintered at 1100ºC for 5 min. with alumina ball at a: (a) 5 N load, (b) 10 N load, (c) 15 N load, and (d) comparison of COF.

The trend of the COF is similar to the trend observed for both the previous samples. For this sample the time required to stabilize the COF value is similar to the sample sintered at 800ºC. Under the action 15 N load the COF quickly increases indicating that severe rubbing action has occurred between the ceramic and the steel. However the time elapsed to reach the stable value is similar to the first two samples.

Fig. 3.33 shows the trend of the COF with the sliding time for the sample sintered at 1100ºC for 10 min. For this sample at a all three values of the loads the COF quickly increases to

the stable value and then remains constant for the remaining sliding time. This can be the effect of a high surface roughness value (1.297 µm) of the sample before the start of sliding.

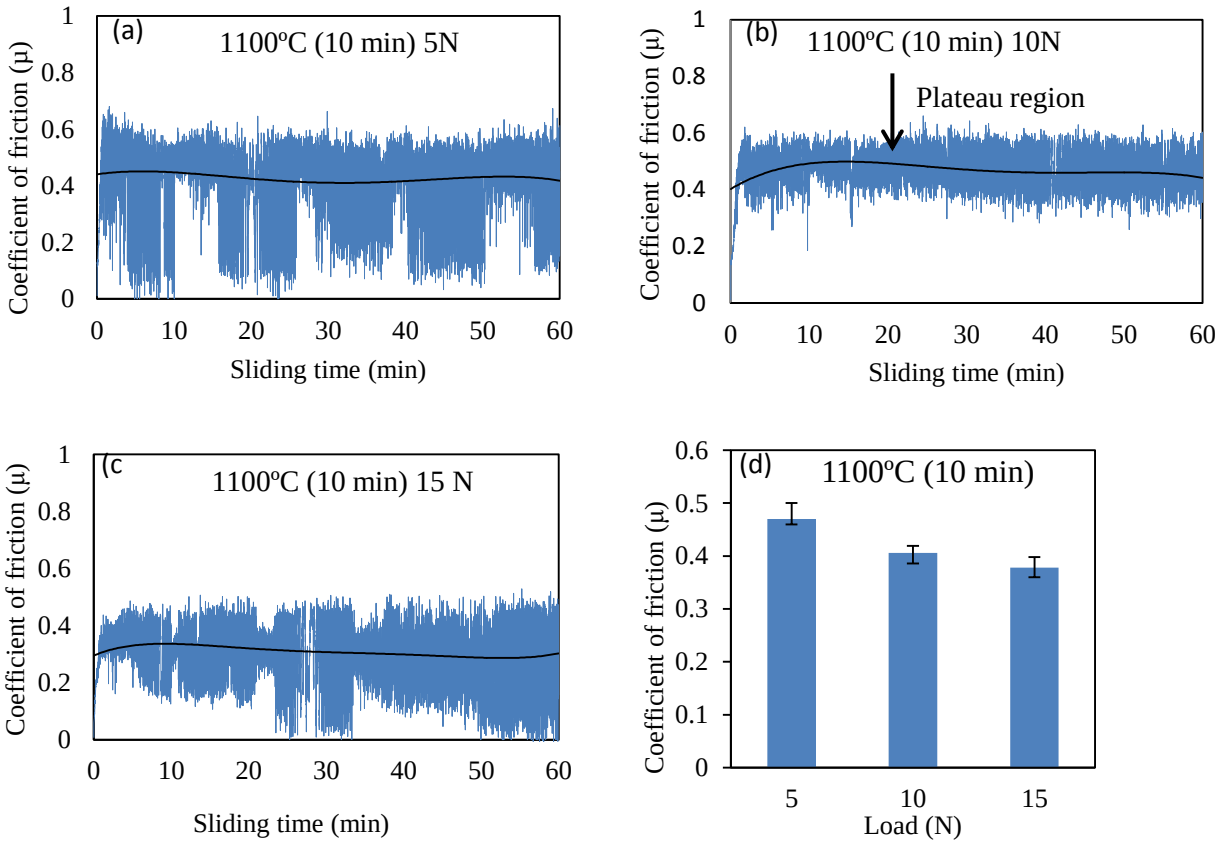

Figure 3.33 COF versus sliding time for sample sintered at 1100ºC for 10 min. with alumina ball at a: (a) 5 N load, (b) 10 N load, (c) 15 N load, and (d) comparison of COF.

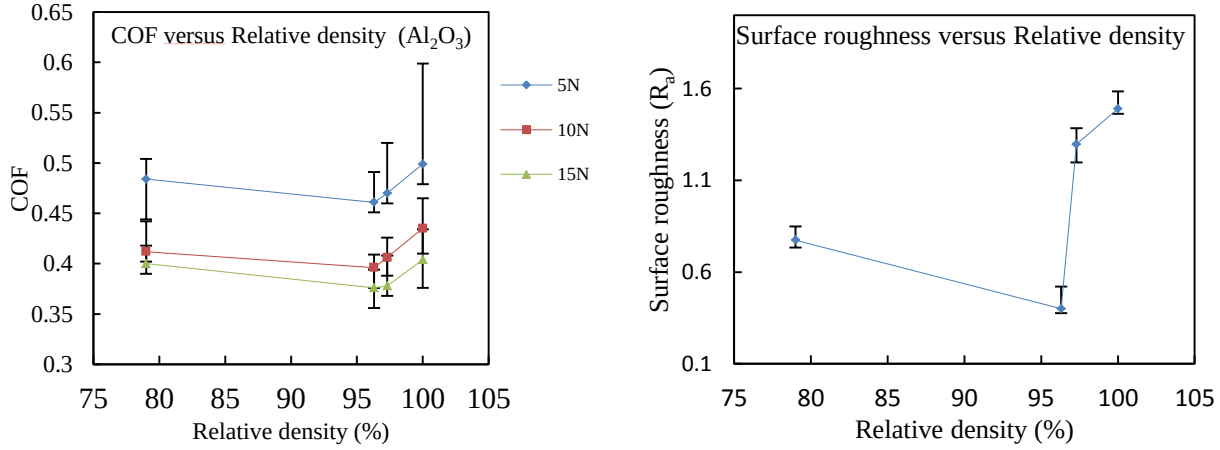

Figure 3.34 (a) COF versus relative density, and (b) Surface roughness versus relative density.

This creates more wear debris and results in less friction at the contact. The similar behavior was observed by Ajithkumar *et al.* [63] for wearing of Mg–Si alloys and Chaudhury *et al.* [64] for aluminum. The value of the COF for each sample can be explained by plotting the COF with the relative density of the sample. The trend followed by the COF with the relative density matches with the trend followed by the surface roughness with the relative density. For each value of the load, the lowest COF is observed for the sample sintered at 800ºC for 10 min. The reason for this phenomenon is the lowest surface roughness (0.4 μm) value for the sample. The highest COF is observed for the as-received plate sample for each load. This is because of the highest surface roughness value (1.49 μm) measured for the plate. The similar behavior of the surface roughness dependence of the COF was observed by Karak *et al.* [65] for ferritic steel.

3.5.1.2 Microstructural analysis of wear surface

3.5.1.2.1 As-received plate

At the initial stage of a wear process the alumina ball creates a severe scratching on the steel plate. This abrasion produces fine debris particles on the wear surface. Fig. 3.35 (c) shows the microflakes on the wear track due to debris particles. The plate material fails by forming short and discontinuous chips. These chips are typically 5-10 μm in size. Fig. 3.36 shows the widening process of the wear track by spallation. Fig. 3.36 (a) shows a chip getting separated from the edge of a wear track which will result in the widening of the track. This chip formation process is gradual and these chips can be overlapping on each other. Fig. 3.36 (b) shows the chips overlying on each other.

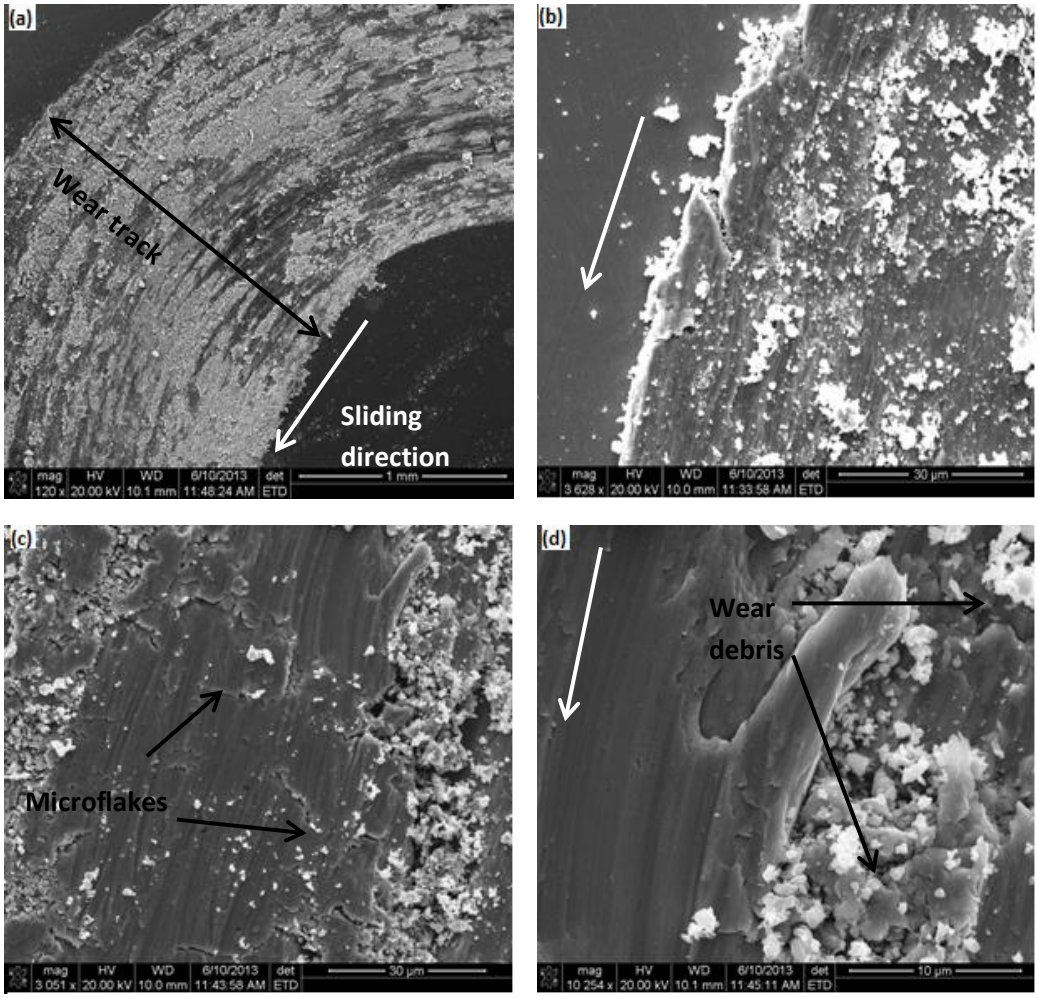

Figure 3.35 SEM images of wear track of as-received modified 9Cr-1Mo plate with alumina ball after 60 min. at a 15N load.

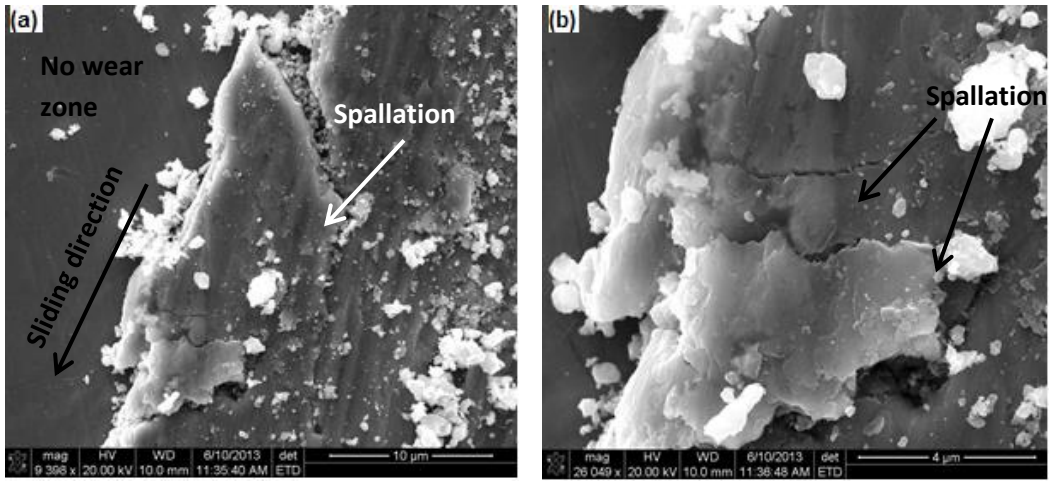

Figure 3.36 Spallation at the edge of a wear track.

3.5.1.2.2 Sample sintered at 800ºC for 10 min.

Fig. 3.37 shows the SEM images of a wear track on the sample sintered at 800ºC for 10 min. which slid with alumina ball for 60 min. at a 15 N load. Fig. 3.38 (a) shows the morphology and the size of a wear track. Fig. 3.37 shows the occurrence of microflakes on the wear track.

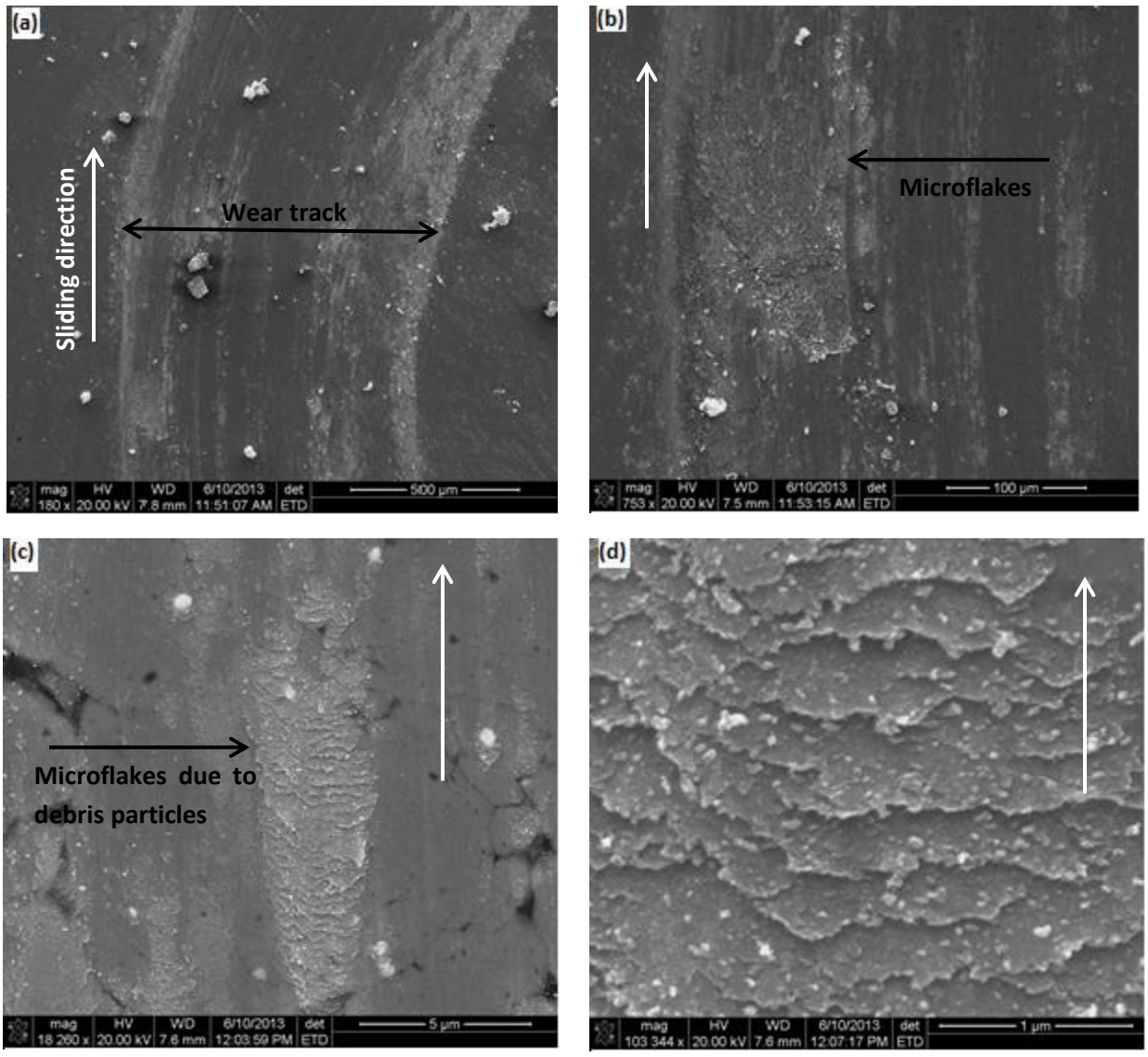

Figure 3.37 SEM images of wear track of a sample sintered at 800ºC for 10 min. with alumina ball after 60 min. at a 15N load.

Fig. 3.37 (d) is a high resolution image of the Fig. 3.37 (c) which shows the size of the chips formed due to spallation of the steel sample. Fig. 3.38 shows the worn surface of an alumina ball used with the sample. Figure shows the two types of debris accumulated on the ball. The chip-like features similar to the steel sample can be observed on the worn surface of the ball. These features are the debris on the wear track that got flattened and adhered to the ceramic ball during wear.

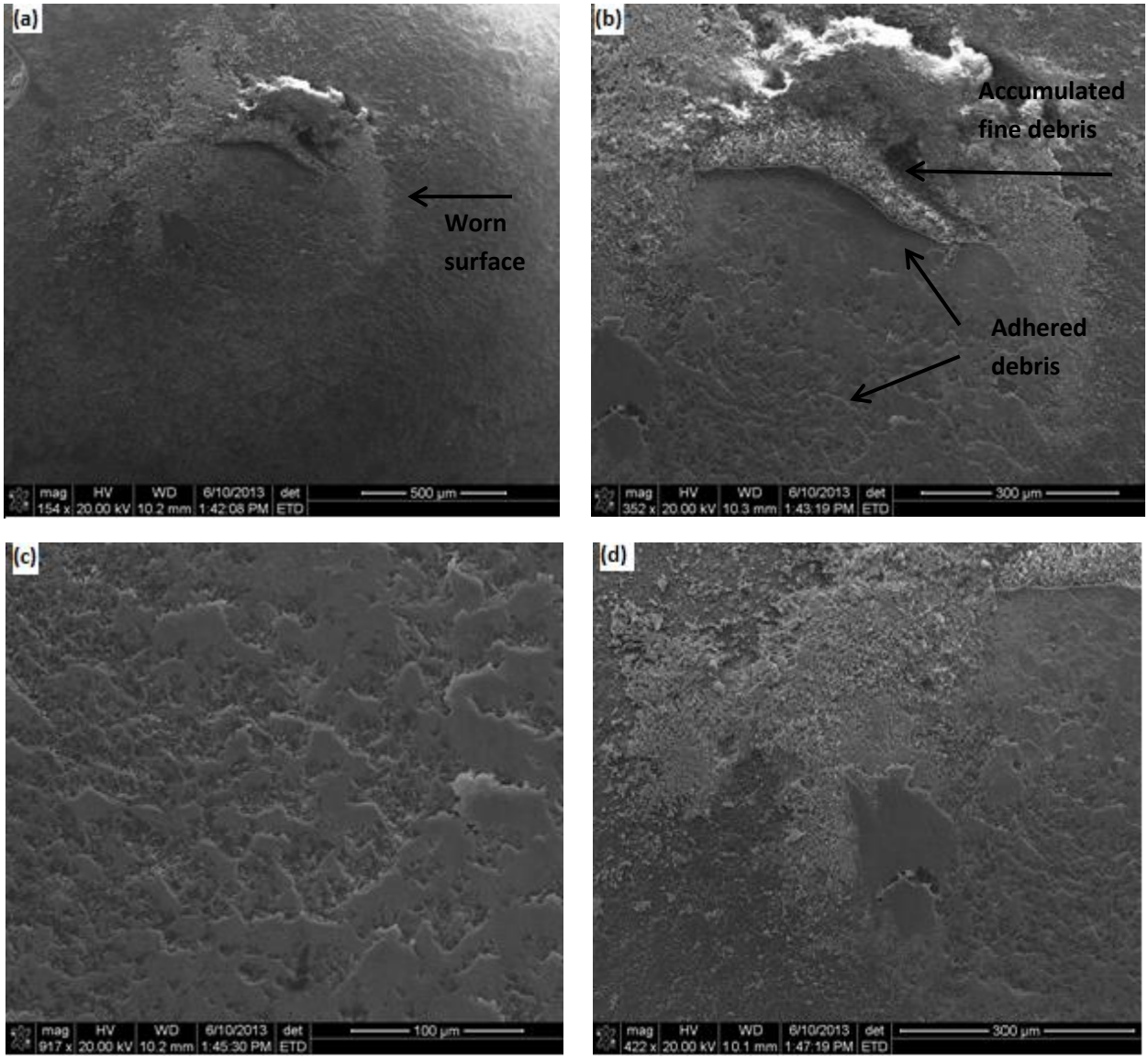

Figure 3.38 SEM image of a worn surface of an alumina ball with 800ºC 10 min. sample after 60 min. sliding at a 15 N load.

The fine debris accumulated outside the boundary of the worn surface are the aluminum particles which are separated during the wearing of the ball. The above explaination can be justified by the EDS scanning of the worn surface of an alumina ball. Fig. 3.39 shows the EDS analysis results of the above discussed worn surface of an alumina ball. Fig. 3.39 (b) shows the elements detected on the worn surface of an alumina ball. The peaks of palladium (Pd) and gold (Au) are attributed to the Au-Pd coating applied on the alumina ball for making it electrically conductive for SEM.

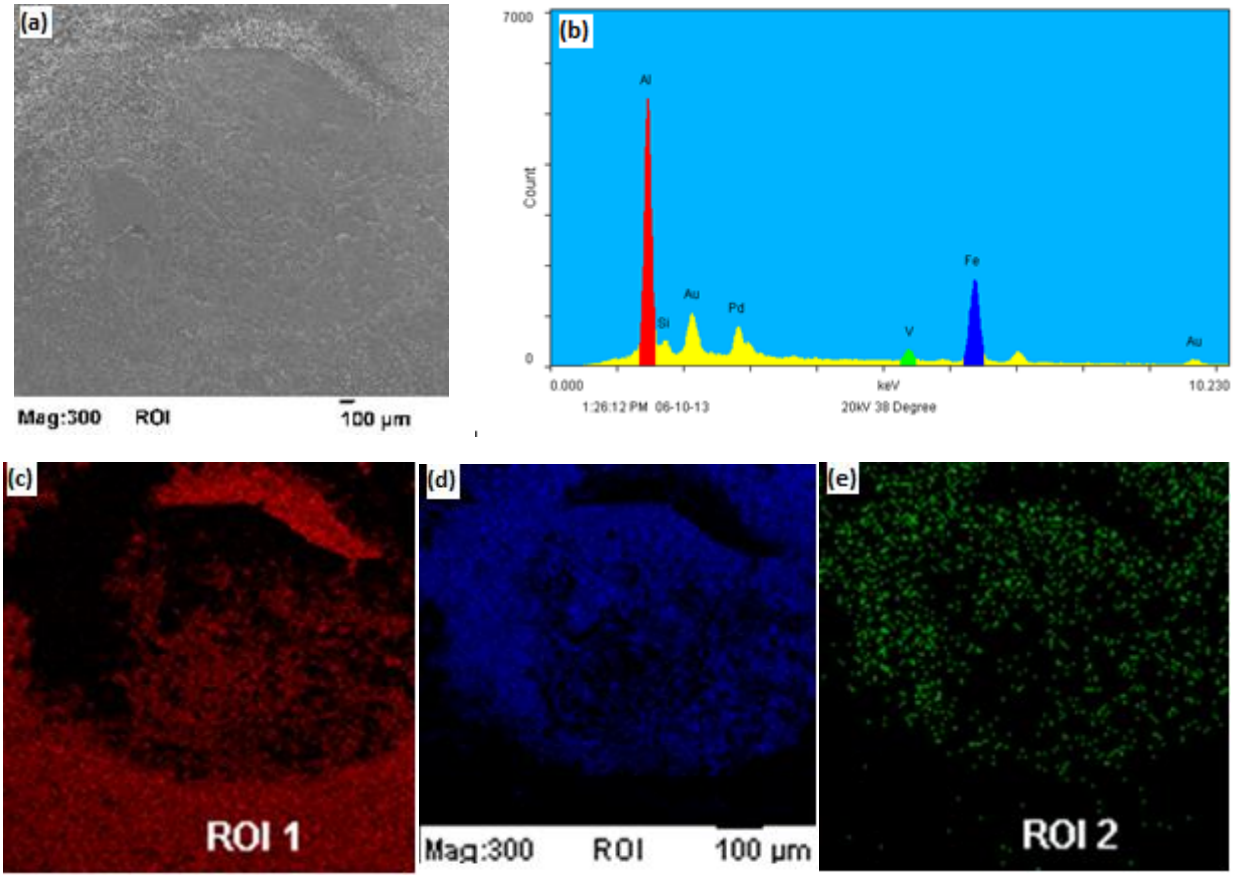

Figure 3.39 EDS scan results of an alumina ball used with 800ºC 10 min. sample after 60 min. at a 15 N load: (a) SEM image, (b) EDS elemental count, (c) aluminum mapping, (d) iron mapping, and (e) vanadium mapping.

From Fig. 3.39 (d) and (e), it can be observed that the chip-like features present on the worn surface contain Fe and V that has adhered from the steel sample. The fine debris observed around the circumference of the worn surface shows the presence of aluminum which can be attributed to the presence of aluminum particles separated from the alumina during wearing of the ball. The fine debris containing Fe and V is a result of the fine paricles separated during cracking and fracture of the microflakes. To trace the elements present on the wear track of the sample, an EDS scan of a wear track is performed. Fig. 3.40 shows the EDS scan results of the wear track on the steel sample sintered at 800ºC for 10 min. slid with alumina ball for 60 min. at a 15 N load. As can be seen from Fig. 3.40 (b) only Fe and Cr are detected on the wear track of the steel sample. This analysis confirms that there is no retransfer of the steel mass adhered to ball has occurred on the wear track. No traces of aluminum were detected on the wear track attributing to the absence of the aluminum particles in the wear debris on the track.

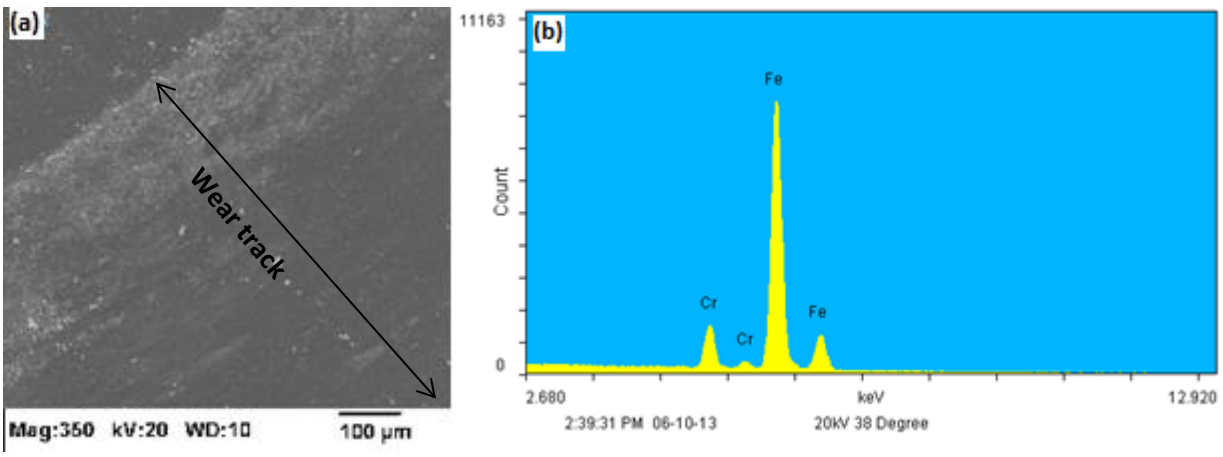

Figure 3.40 EDS scan results of a wear track of the sample sintered at 800ºC for 10 min.: (a) SEM image, and (b) EDS elemental count.

3.5.1.2.3 Samples sintered at 1100ºC

Fig. 3.41 shows the SEM images of a wear track of a sample sintered at 1100ºC for 5 min. which slid with alumina ball for 60 min. at a 15 N load. Similar scale-like features are observed on the wear track which are of the submicron size.

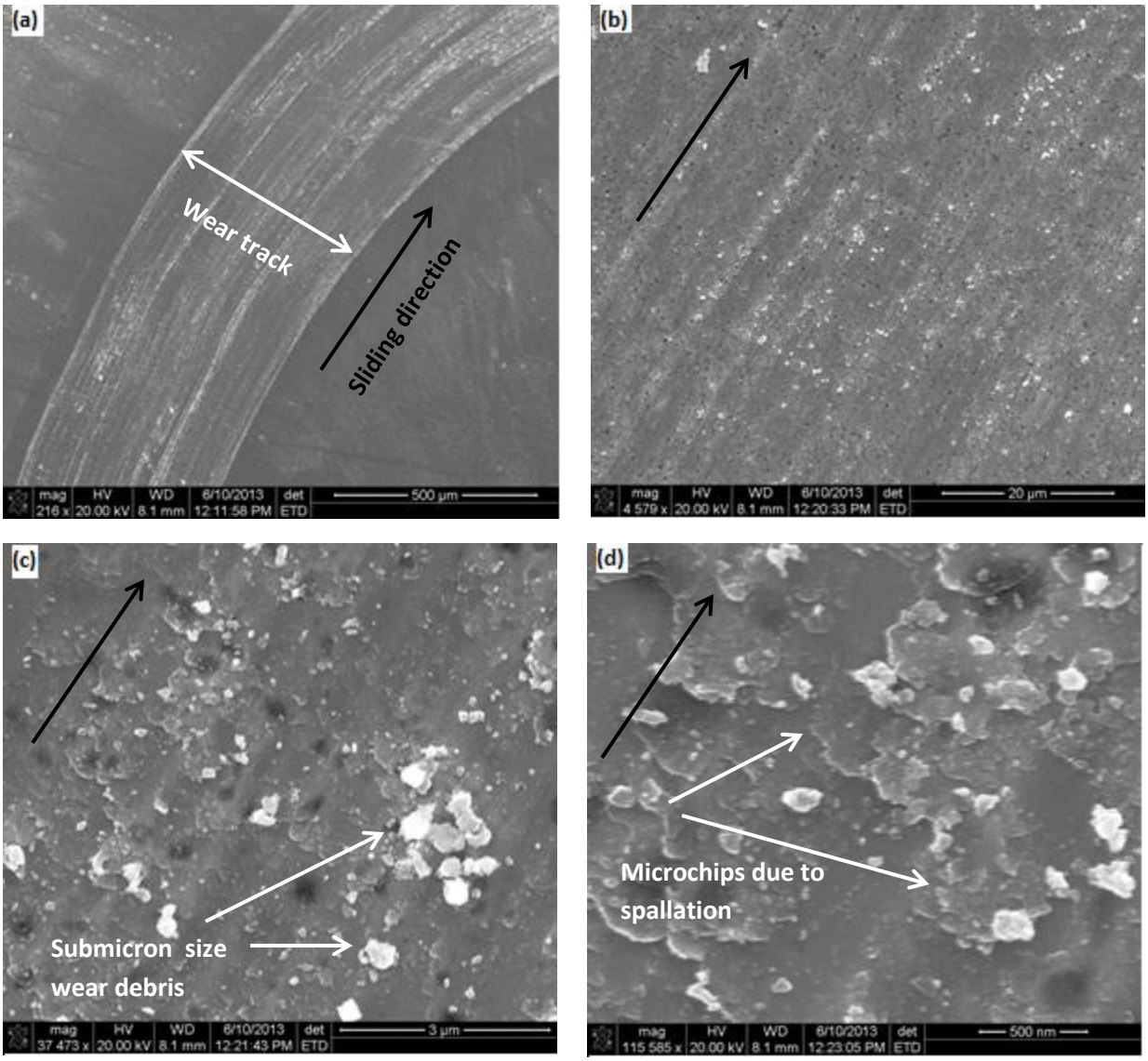

Figure 3.41 SEM images of a wear track of sample sintered at 1100ºC for 5 min. slid with alumina ball after 60 min. at a 15 N load.

This is indicative of the formation of microflakes during wear. In addition to this, few dark spots are observed on the wear track which can be seen in Fig. 3.41 (b). These dark areas appear due to the delamination of the steel sample at the later stage of wear. These dark spots can be the result of the oxidation of the steel surface. However the sliding velocity and load used in our testing are not enough to generate flash temperatures which can cause oxidation. Along with the spallation, few submicron size wear debris are also observed on the wear track. (Fig. 3.41 (c), (d)). To characterize these wear debris, an EDS scan was performed on the wear track.

Fig. 3.42 shows the elemental analysis of a wear track on the sample sintered at 1100ºC for 5 min. which slid with alumina ball for 60 min. at a 15 N load. Figure shows the presence of only Fe and Cr on the wear track. This indicates that the submicron sized wear debris particles are composed of only the elements present in the steel sample. No element separated from the alumina ball was observed on the track. The small debris particles must have been produced during the fracturing of the microflakes.

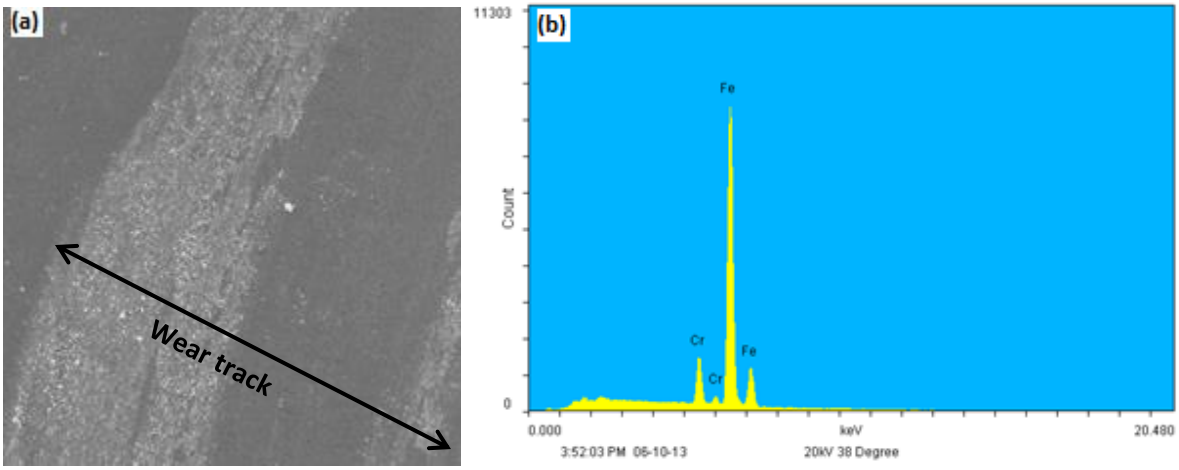

Figure 3.42 EDS scan results of a wear track of sample sintered at 1100ºC for 5 min.: (a) SEM image, and (b) EDS elemental counting.

Fig. 3.42 shows the SEM images of the wear track of the sample sintered at 1100ºC for 10 min. which slid with the alumina ball for 60 min. at a 15 N load. The white colored arrow in each image shows the sliding direction. The wear track shows the presence of both black spots along with the microflakes that formed due to the spallation action.

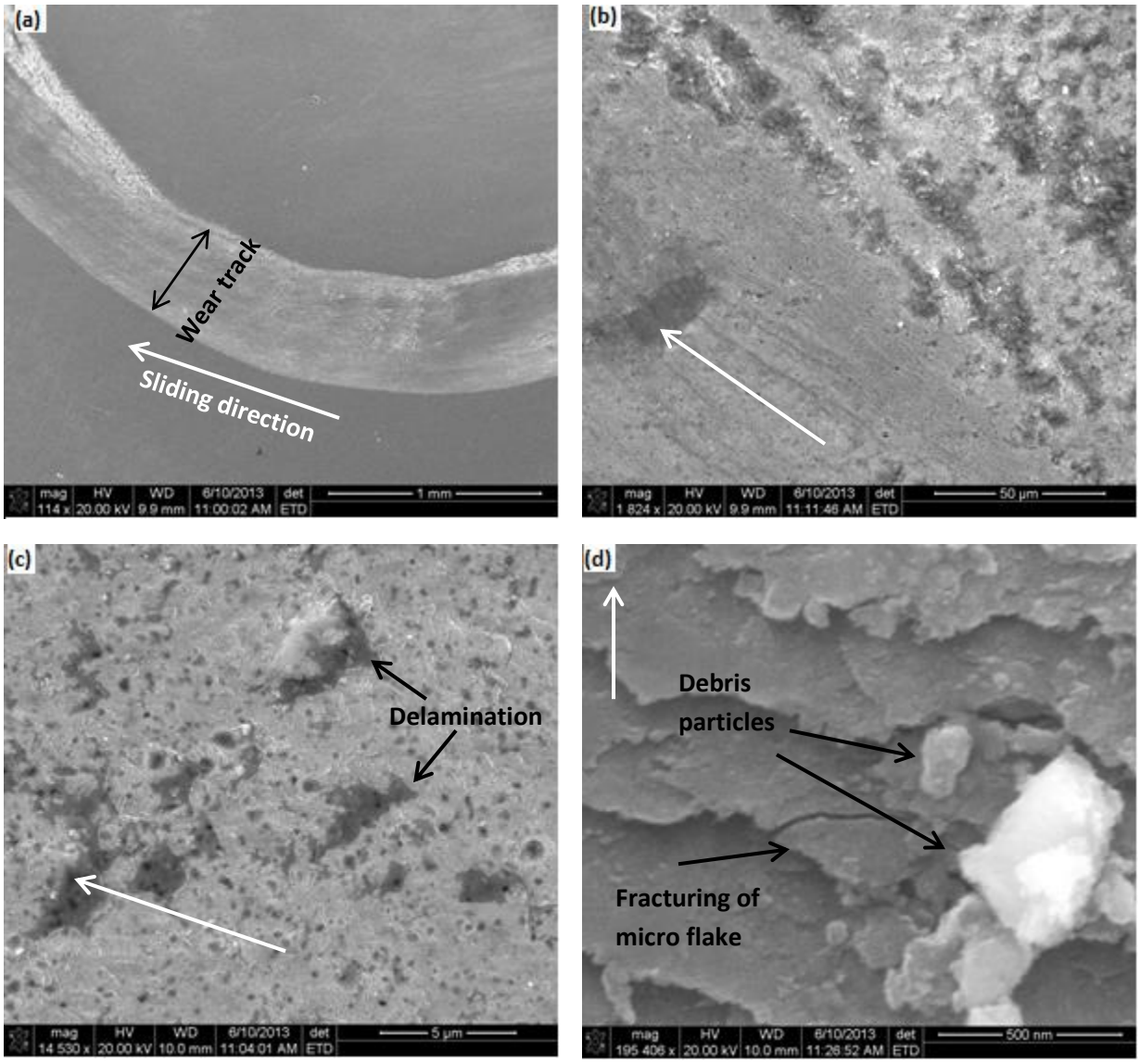

Figure 3.43 SEM images of wear track of a sample sintered at 1100ºC for 10 min. with alumina ball after 60 min. at a 15 N load.

The black areas on the wear track correspond to the delamination of the steel sample due to the increasing wear. Fig. 3.43 (d) shows the incidence of fracturing of the microflake. This phenomenon results in the formation of ultrafine fragments which remain on the track in the form of the wear debris. To verify if the abrasive wear still governs the wear process, the SEM imaging along with EDS scanning of an alumina ball used with the sample, sintered at 1100ºC for 10 min. is performed. Fig. 3.44 shows the SEM images of an alumina ball. Figure shows the worn surface on the alumina ball. Two types of wear debris are present on the worn surface of the ball. The scale-like features confirm the adhesion of the Fe and Cr on the ball. These adhered debris on the ball are less when compared to the adhered debris on the ball used for the sample sintered at 800ºC for 10 min. This indicates that less wear has occurred on the steel sample which can be attributed to the high hardness (634 HV) of the sample sintered at 1100ºC compared to the hardness of the sample sintered at 800ºC (532 HV). The debris lying around the circumference of a worn area of the ball are made up of submicron sized particles. These particles are composed of Fe, Cr and V separating out from the sample as well as Al wearing out from the alumina ball. To ensure above made claims, an EDS analysis was performed on the worn surface of the ball. Fig. 3.45 shows the EDS analysis results of an alumina ball used for the sample sintered at 1100ºC for 10 min.

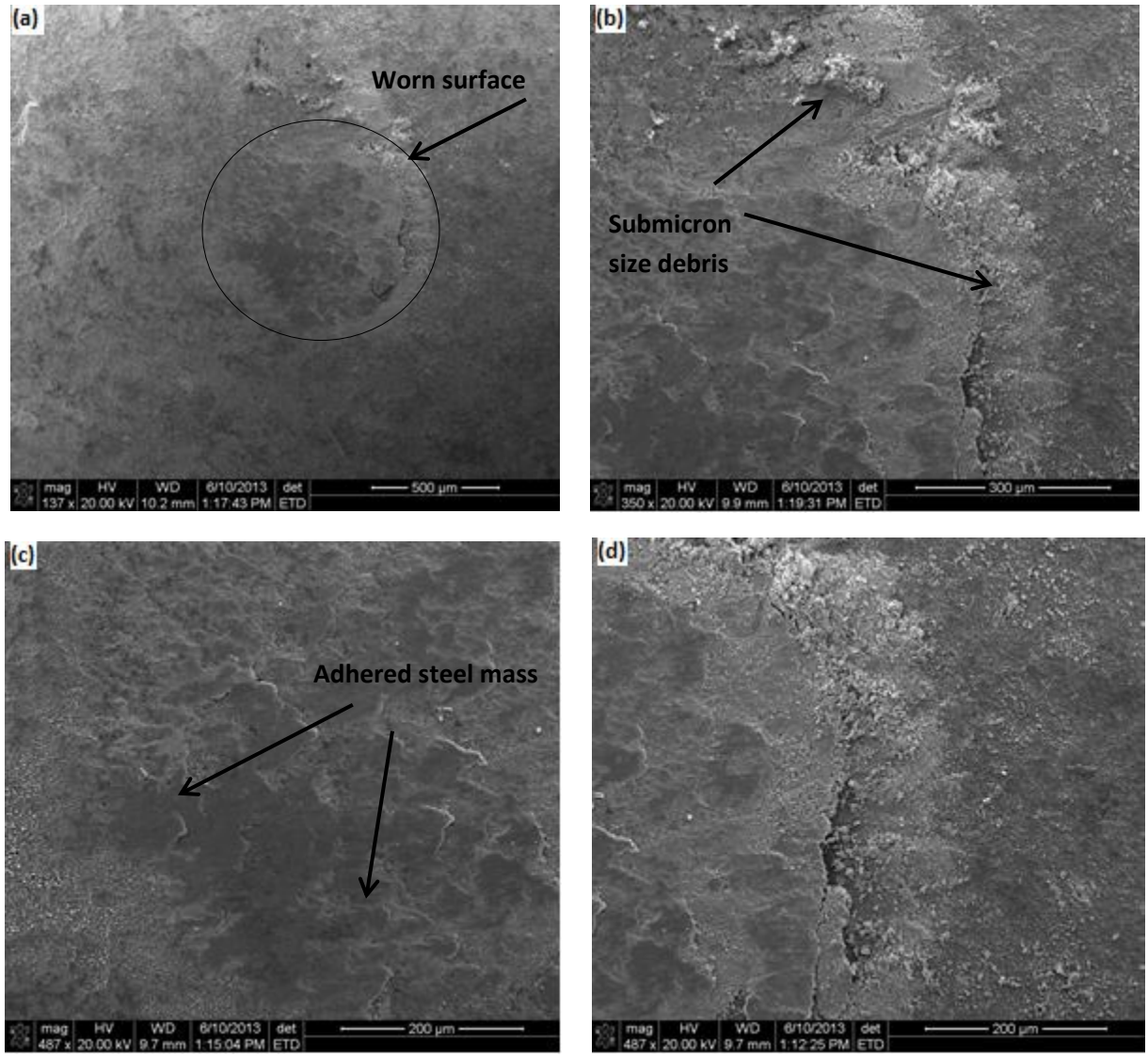

Figure 3.44 SEM images of worn surface of an alumina ball slid for 60 min. with the sample sintered at 1100ºC for 10 min. at a 15 N load.

Figure shows the peaks of Fe and Cr which are adhered to the ball surface in the form of scales like features. Al is a ball material and is also present in the form of small particles around the circumference of a worn surface area. The peaks of Au and Pd are observed due to the Au-Pd coating applied on the alumina ball to make it electrically conductive. It is confirmed that no unexpected element is found on the ball surface and hence no phase transformation or chemical reaction has occurred during the 60 min. of sliding.

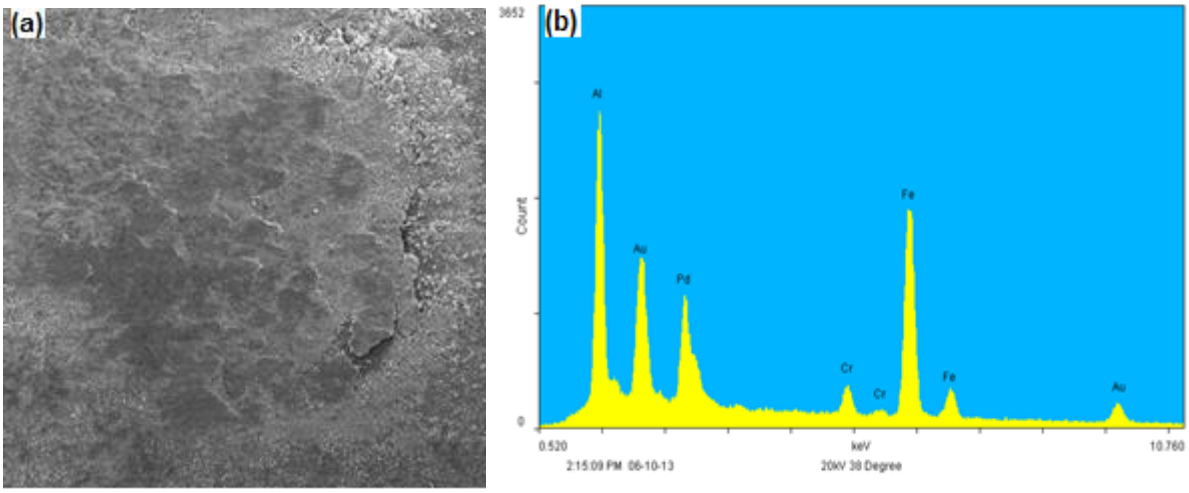

Figure 3.45 EDS analysis of an alumina ball used with the sample sintered at 1100ºC for 10 min.: (a) SEM image of a worn surface, and (b) EDS elemental count.

3.5.1.3 Wear rate

Wear rates of the steel samples worn with alumina balls are high. They are typically of the order of 10^{-4} to 10^{-5} mm^3/Nm. Fig. 3.46 shows the wear rate for each sample at each load calculated after 60 min. of wearing with an alumina ball. For a particular sample the wear rate increases with the increase in load. However, the wear rate is not a direct function of a load as its value is not doubling with the value of the load. The wear rate of the samples is of the order of 10^{-5} with the 10^{-4} for the as-received steel plate. This order of magnitude decrease in the wear rate can be attributed to the increase in the hardness of the sintered samples. Hence, indirectly the wear rate is dependant on the material grain size as well as relative density. The sample sintered at 1100ºC for 10 min. shows the lowest wear rate (1.7×10^{-5} mm^3 /Nm) at a 15 N load. For each sample the sharp increase in wear rate can be observed at a 15 N load which can be attributed to the increased delamination of the surface at a higher load.

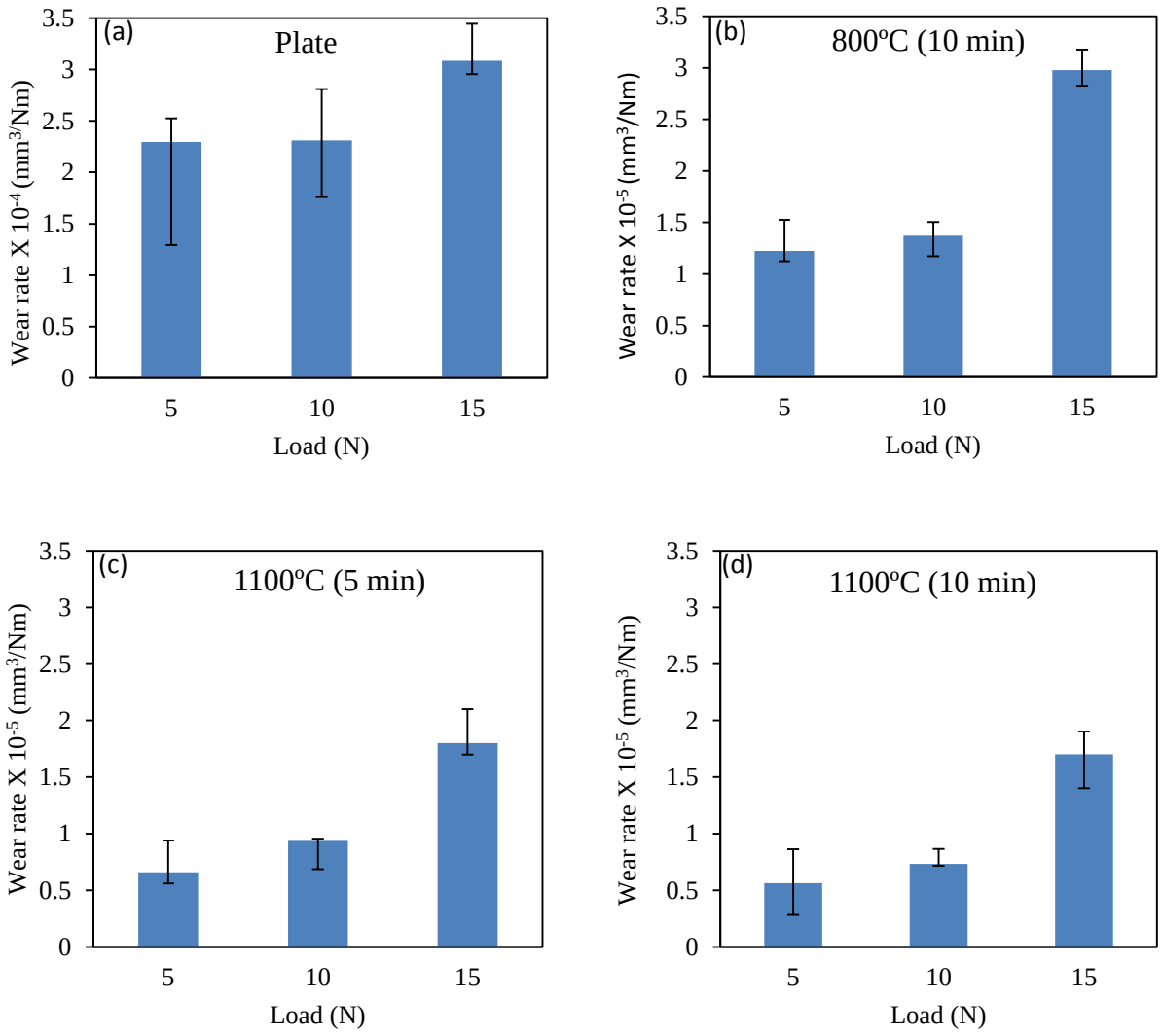

Figure 3.46 A comparison of wear rate for different loads with alumina ball for: (a) as-received plate, (b) sample sintered at 800ºC for 10 min., (c) sample sintered at 1100ºC for 5 min., and (d) sample sintered at 1100ºC for 10 min.

3.5.2 Wear analysis with the silicon nitride (Si_3N_4) ball

Dry sliding of silicon nitride ball on the steel surface presented an altogether different tribological behavior than the alumina on steel combination. A tribolayer composed of Fe-Si-Cr is formed at the interphase during first 10 min. of sliding [66].

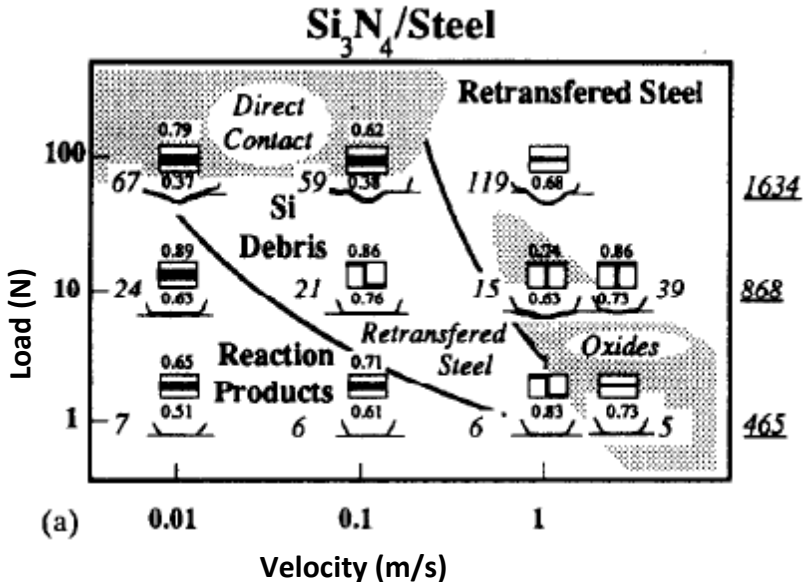

Figure 3.47 Load versus sliding velocity wear mechanism map of silicon nitride on steel (Reprinted from [62] with the permission of the publisher).

The wearing action proceeds with the breaking and again forming of a tribolayer. Gautier *et al.* [62] systematically carried out the wear analysis of ceramics on a steel disc and explained the wear maps for different load-velocity combinations. For our load-velocity combination (15 N, 0.03 m/s), Si debris are found on the wear track.

3.5.2.1 Coefficient of friction

3.5.2.1.1 As-received plate

Fig. 3.48 shows the COF versus sliding time for an as-received plate sample with the silicon nitride ball. A particular trend of COF is observed for each load with sliding time. There are three distinct regions present on the COF versus sliding time curve. In the first step, a tribolayer is generated at the interphase.

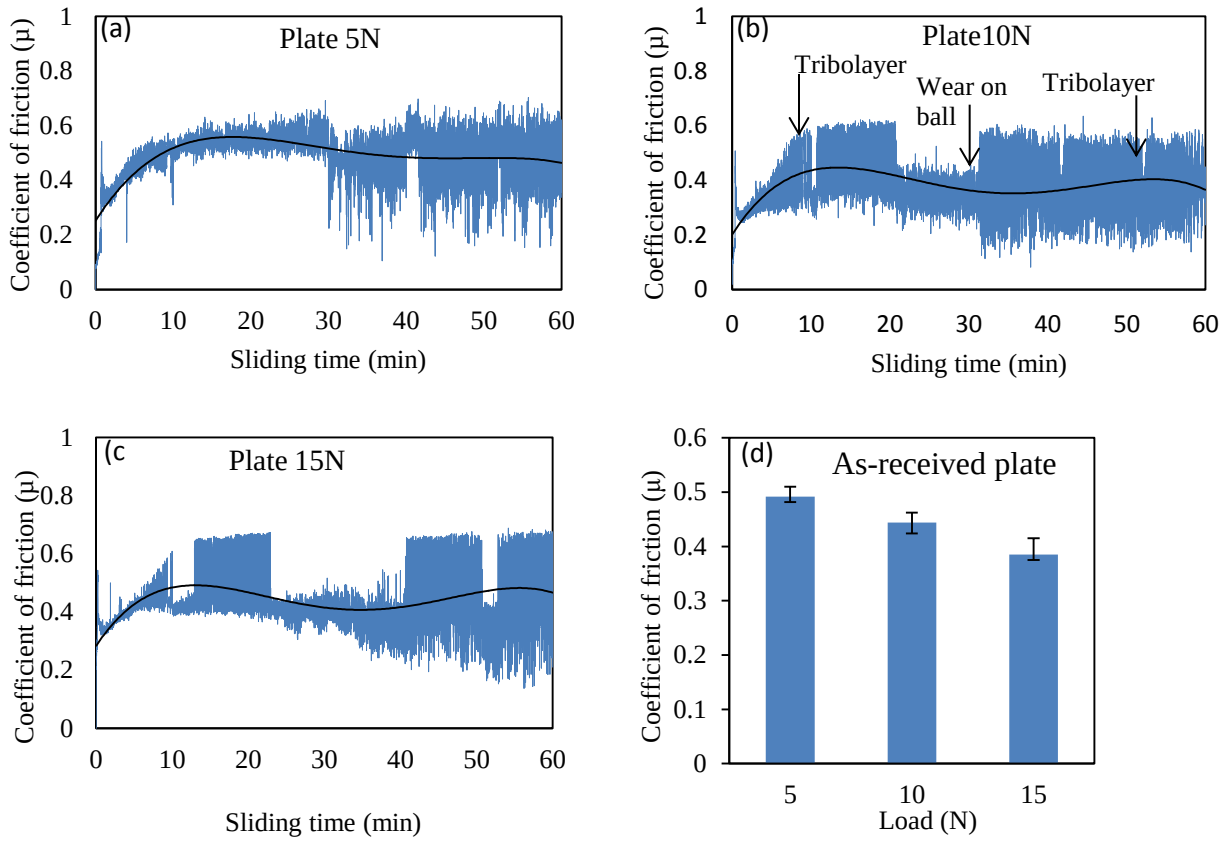

Figure 3.48 COF versus sliding time of as-received plate with silicon nitride ball at a: (a) 5 N load, (b) 10 N load, and (c) 15 N load.

The drop in the friction coefficient is observed due to the direct contact between the silicon particles and steel surface. At the later stage again the generation of the tribolayer increases the COF. This mass of steel gives higher COF and protects the steel from further damage.

3.5.2.1.2 Sample sintered at 800ºC for 10 min.

A similar trend of COF is observed for the sample sintered at 800ºC for 10 min. For the silicon nitride ball the time needed to reach the peak value of the COF is more than the time needed for the alumina ball.

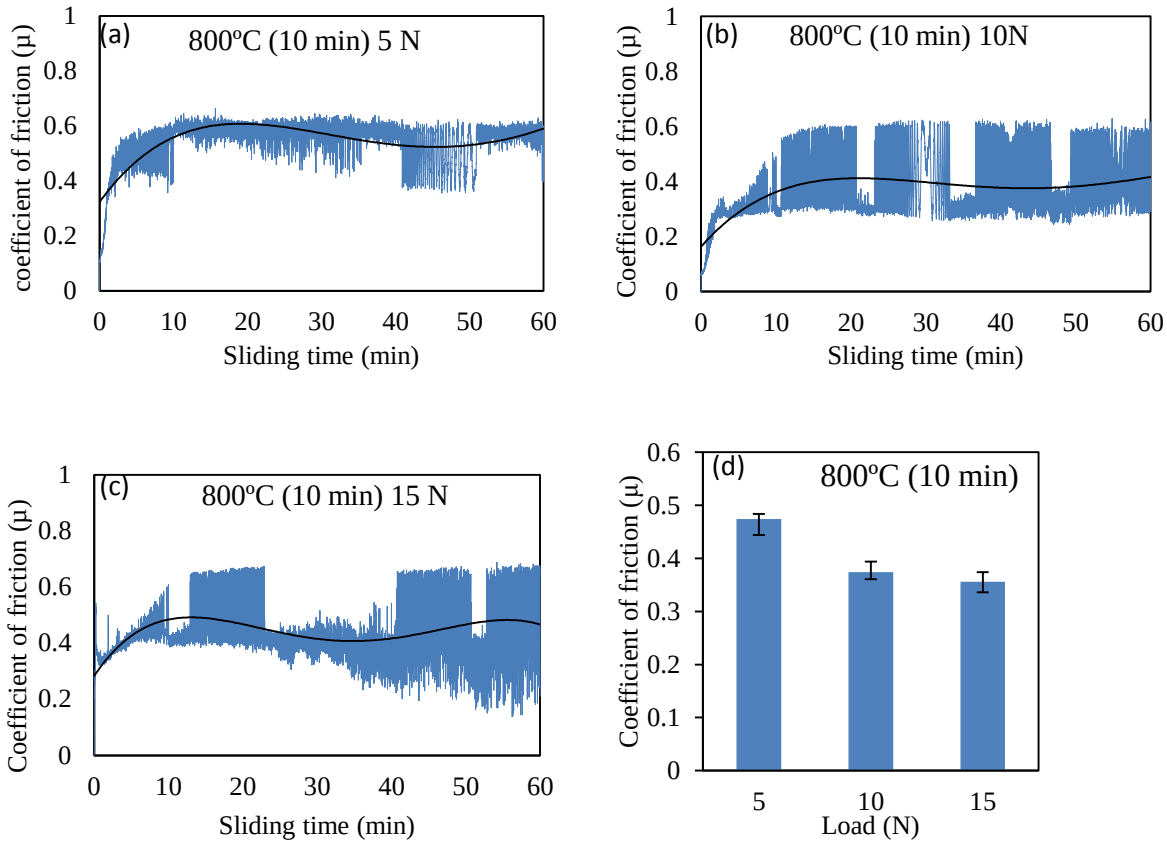

Figure 3.49 COF versus sliding time for alumina ball with the sample sintered at 800ºC for 10 min. at a: (a) 5 N load, (b) 10 N load, and (c) 15 N load.

This can be attributed to the lower hardness of the silicon nitride ball as compared to the alumina ball. In all three figures, the raising of the COF value can be observed at the final stage of the sliding.

3.5.2.1.3 Samples sintered at 1100ºC

A similar trend with the raising of the COF values at two events is observed. With the increasing load the curve can be observed shifting to the lower values. This is the effect of ploughing of the steel sample by a ceramic and the large amount of wear debris that is produced during the sliding action.

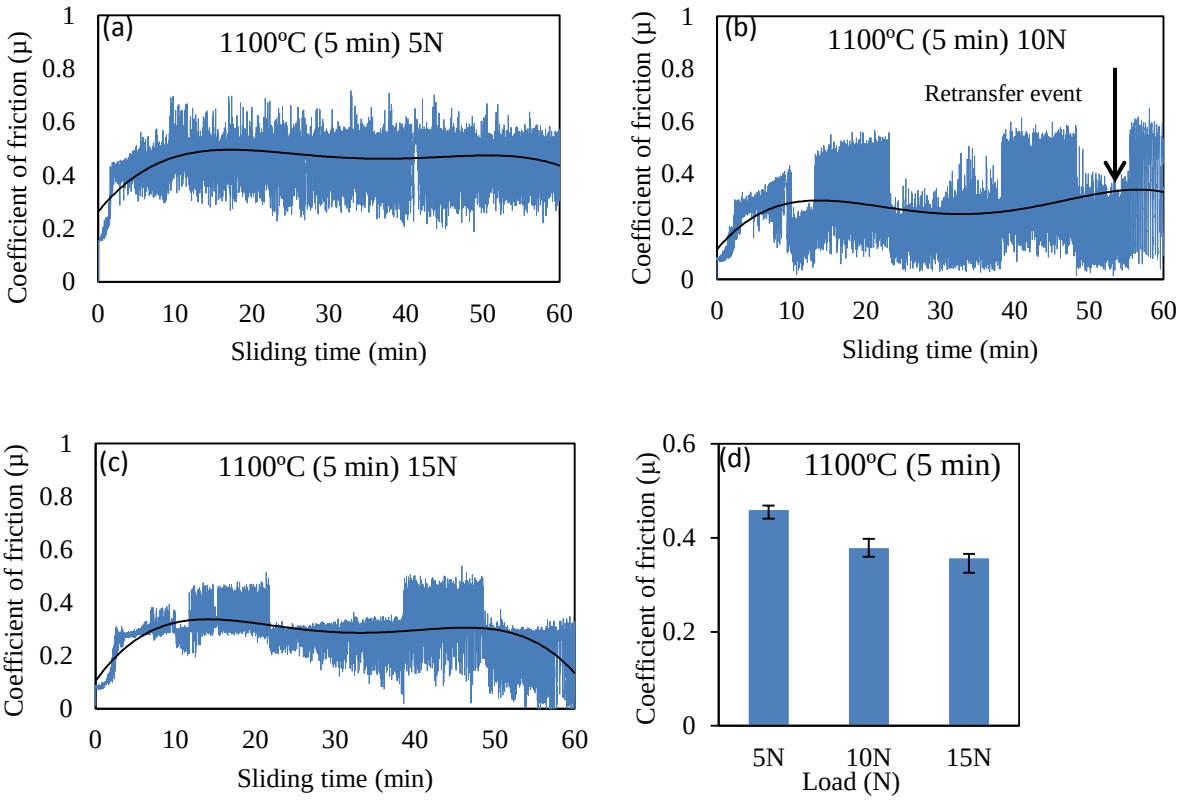

Figure 3.50 COF versus sliding time for alumina ball with the sample sintered at 1100ºC for 5 min. at a: (a) 5 N load, (b) 10 N load, and (c) 15 N load.

Fig. 3.51 shows the trend of the COF with the sliding time for the sample sintered at 1100ºC for 10 min. The fluctuation in COF is not clearly visible for this sample. This indicates that the COF values remained high and almost constant throughout the sliding time. This can be attributed to the higher surface roughness of the sample prior to sliding.

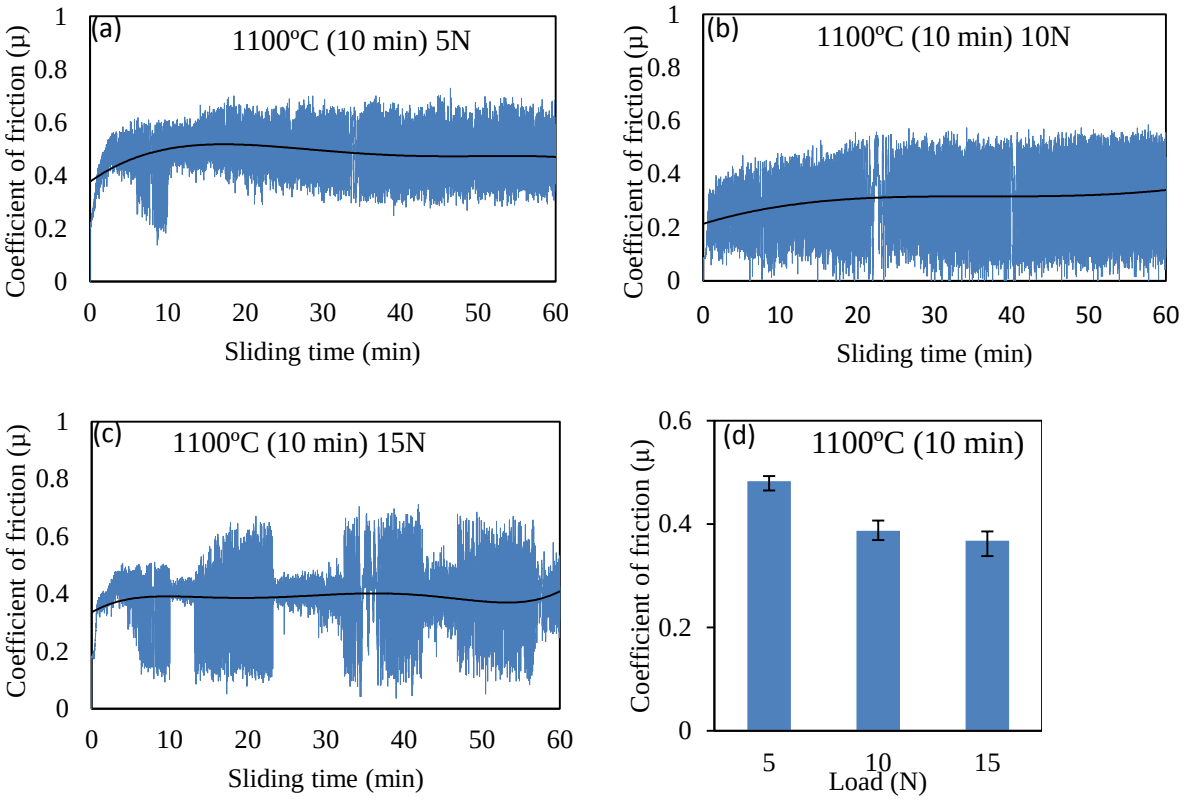

Figure 3.51 COF versus sliding time for alumina ball with the sample sintered at 1100ºC for 10 min. at a: (a) 5 N load, (b) 10 N load, and (c) 15 N load.

For all the samples the average value of the COF is lower than the value obtained for the alumina ball for the same configuration. This is due to the lower hardness of the silicon nitride ball. For a particular sample, the value of the COF decreased consistently with an increasing load. The value of the COF for each sample is dependent on the surface roughness of the sample before starting the wear test. Hence the sample sintered at 800ºC for 10 min. shows the lowest COF and the as-received plate shows the highest COF at any load.

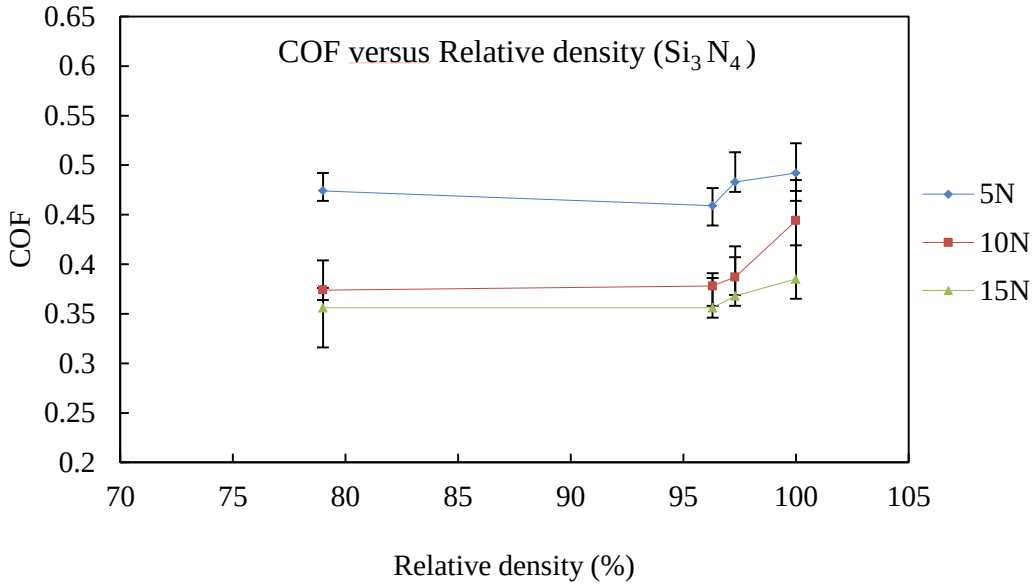

Figure 3.52 COF versus relative density.

3.5.2.2 Microstructural analysis of wear surface

3.5.2.2.1 As-received plate

The abrasive grooves can be seen on the wear track indicating severe abrasive wear has occurred on the plate. Figure shows the presence of debris which is predicted as silicon oxide. The abrasive grooves on the wear track are produced by the free silicon particles present on the track (Fig. 3.53 (c)). To confirm the elements present on the wear track, an EDS scan was performed. Fig. 3.54 shows the results of the EDS scan. The EDS scan confirms the presence of silicon on the wear track. The presence of silicon on the wear track is a result of the wear that has occurred on the silicon nitride ball. The region common for Fe-Cr-Si is a tribolayer.

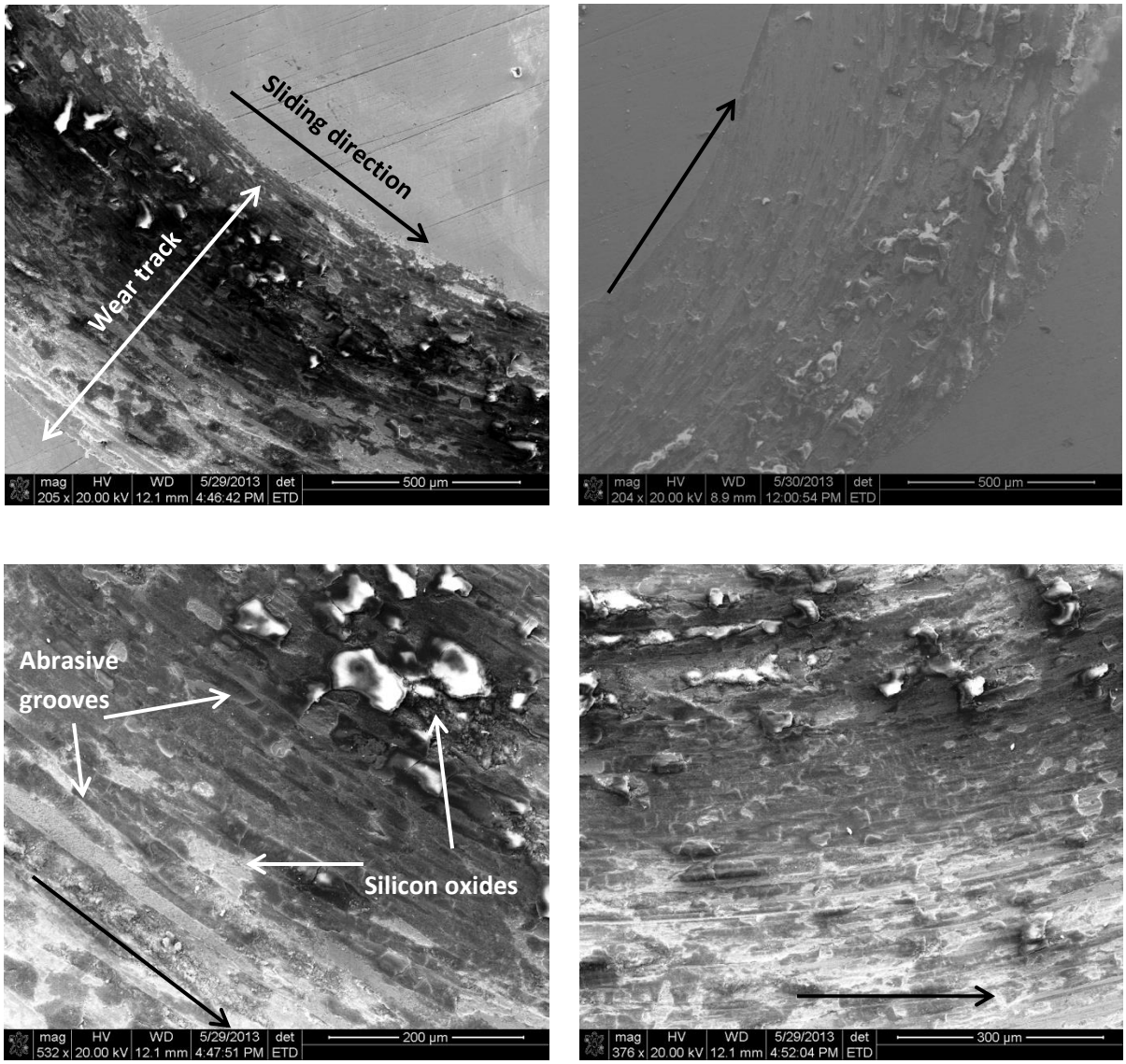

Figure 3.53 SEM images of wear track of a plate slid with silicon nitride ball after 60 min. at a 15N laod.

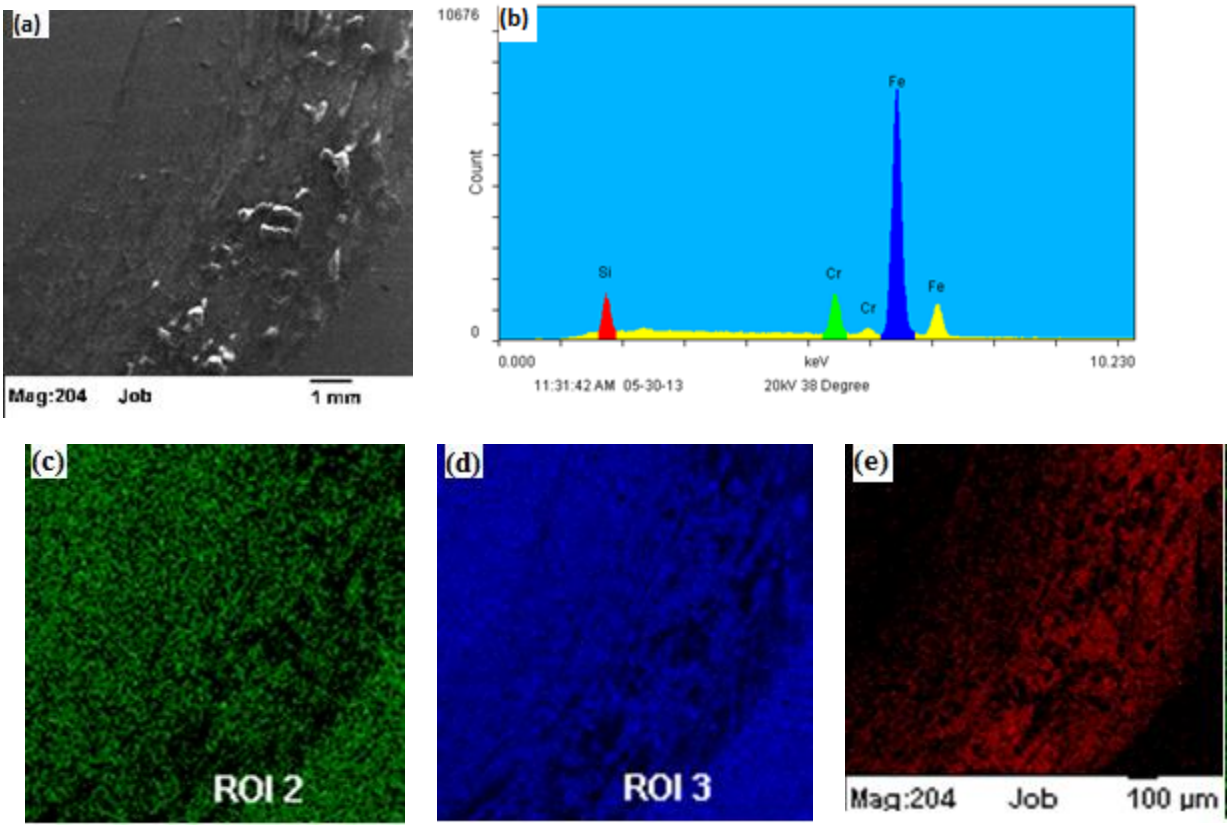

Figure 3.54 (a) SEM image of a wear track, (b) EDS scan results of a wear track of modified 9Cr-1Mo plate with silicon nitride ball at a 15N load, (c) Chromium mapping, (d) iron mapping, and (e) silicon mapping.

3.5.2.2.2 Sample sintered at 800ºC for 10 min.

Fig. 3.55 shows the SEM images of the wear track of the sample sintered at 800ºC for 10 min. which slid with a silicon nitride ball at a 15 N load. A white arrow in each figure indicates the direction of sliding. The tribolayer can be seen on the wear track. The remaining area is exposed to the silicon nitride ball. However, because of the wearing on the silicon nitride ball, some silicon particles become free and adhere to the light-colored, exposed area of the wear track. The further wear action is substantial in the light area and takes place due to the free silicon particles.

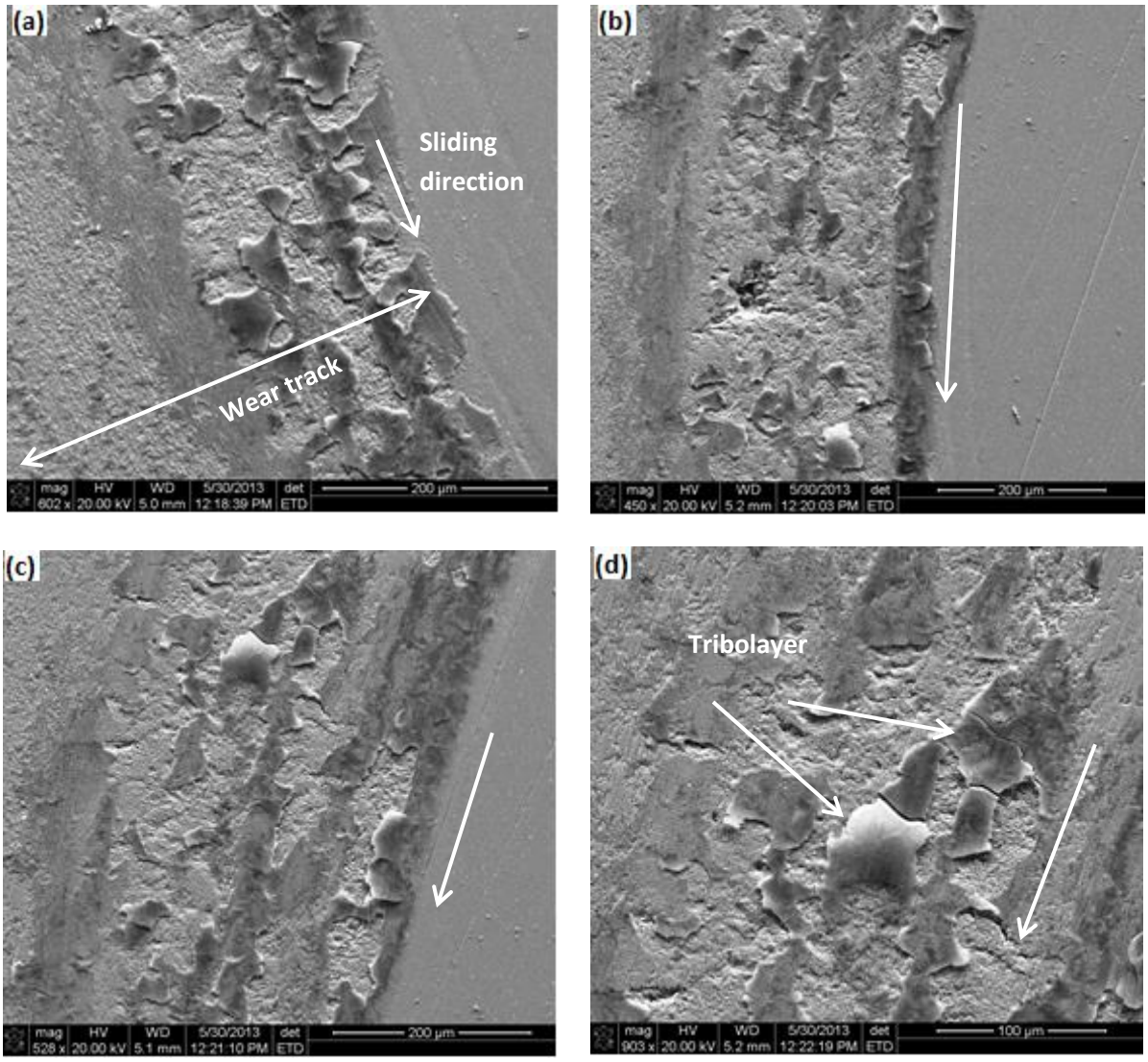

Figure 3.55 SEM images of wear track of sample sintered at 800ºC for 10 min. slid with silicon nitride ball at a 15N load.

3.5.2.2.3 Samples sintered at 1100ºC

Fig. 3.56 shows the SEM images of the wear track of the sample sintered at 1100ºC for 5 min. which slid with silicon nitride ball. The wear track shows two dark and light regions. As discussed earlier the white region is a mass of steel that is protected at the initial stage. The remaining dark region is exopsed to the silicon nitride ball. This dark region is a tribolayer.

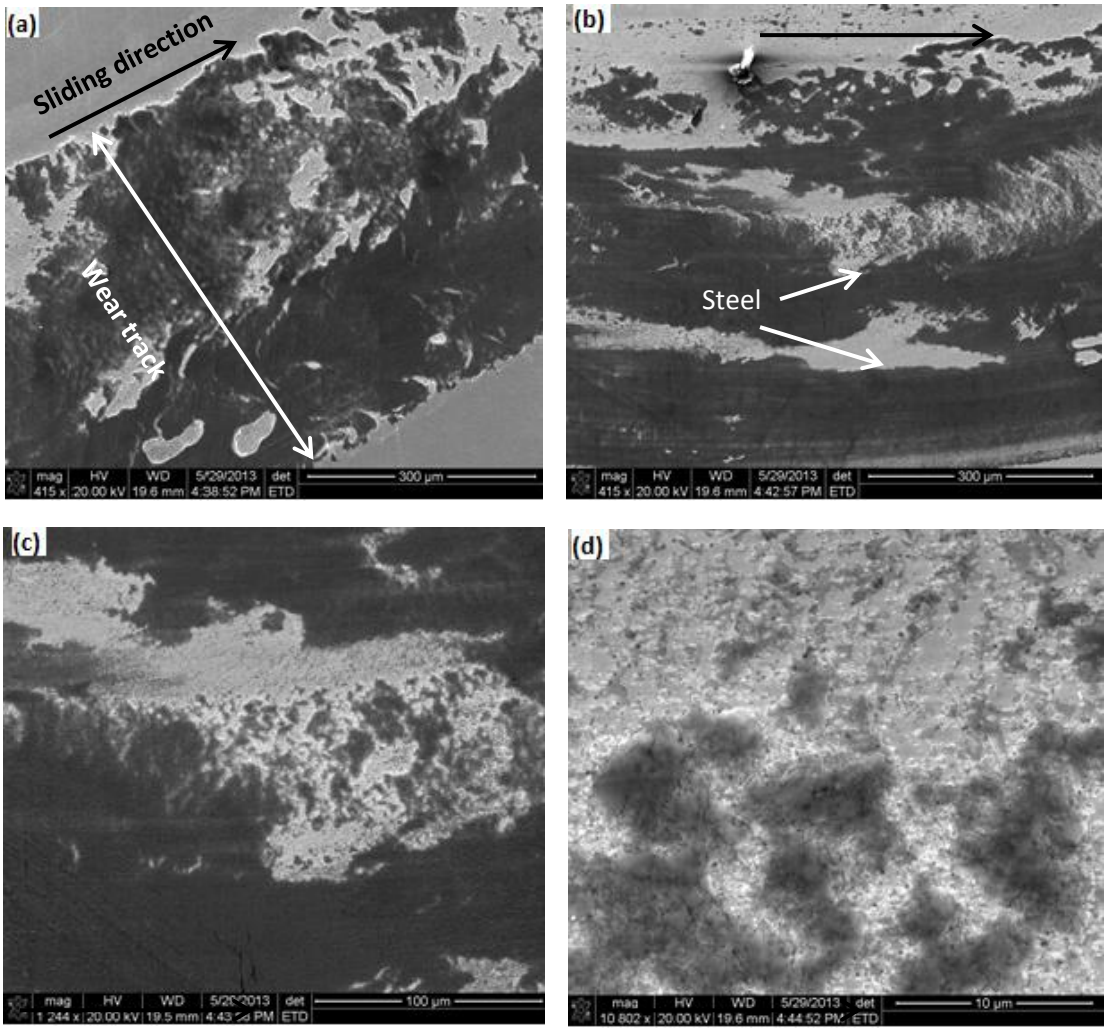

Figure 3.56 SEM images of wear track of the sample sintered at 1100ºC for 5 min. with silicon nitride ball at a 15N load.

Fig. 3.57 shows the SEM images of the wear track of the sample sintered at 1100ºC for 10 min. which slid with a silicon nitride ball at a 15 N load. The scratches on the tribolayer can be seen in the dark area which indicates the continuation of the process of wear. No such polishing marks are observed on the steel mass indicating no wear occured in that area. Similar to the sample sintered at 1100ºC for 5 min., this sample also shows two different regions on the wear track. Figure shows the presence of subsurface cracks in the dark region. In the wear process of the steel by ceramic the plastic deformation and cracking of the wearing surface occurs [63].

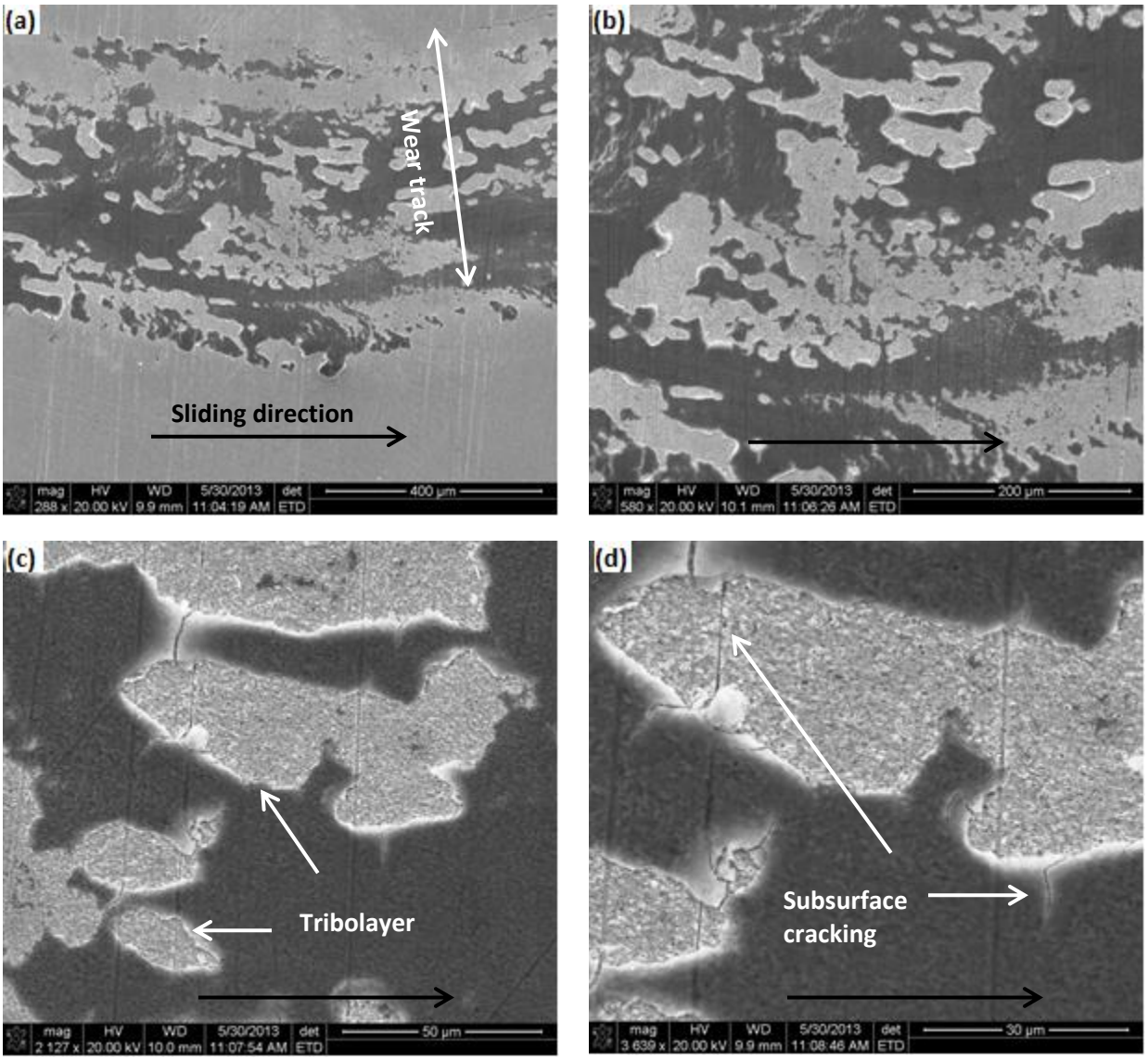

Figure 3.57 SEM images of wear track of sample sintered at 1100ºC for 10 min. with silicon nitride ball at a 15N load.

This cracking further results in the production of wear debris. To verify the elemental composition of the areas on the wear track, an EDS scan was performed on the sample sintered at 1100ºC for 10 min. Fig. 3.58 shows the results of an EDS scan performed on the wear track. It can be verified from Fig. 3.58 (c) that the dark areas on the wear track correspond to the presence of silicon whereas Fig. 3.58 (d) and (e) verify the presence of Fe and Cr throughout the track.

This confirms the presence of a tribolayer on the wear track. The light regions show absence of silicon and correspond to the mass of steel on the wear track. This tribolayer on the wear track results in the order of magnitude decrease of the wear rate compared to the as-received steel plate. To study the wear on the silicon nitride ball the SEM and EDS analyses were performed. Fig. 3.59 shows the SEM images of the worn surface of a silicon nitride ball which slid with as-received steel plate at a 15N load after 60 min. of sliding.

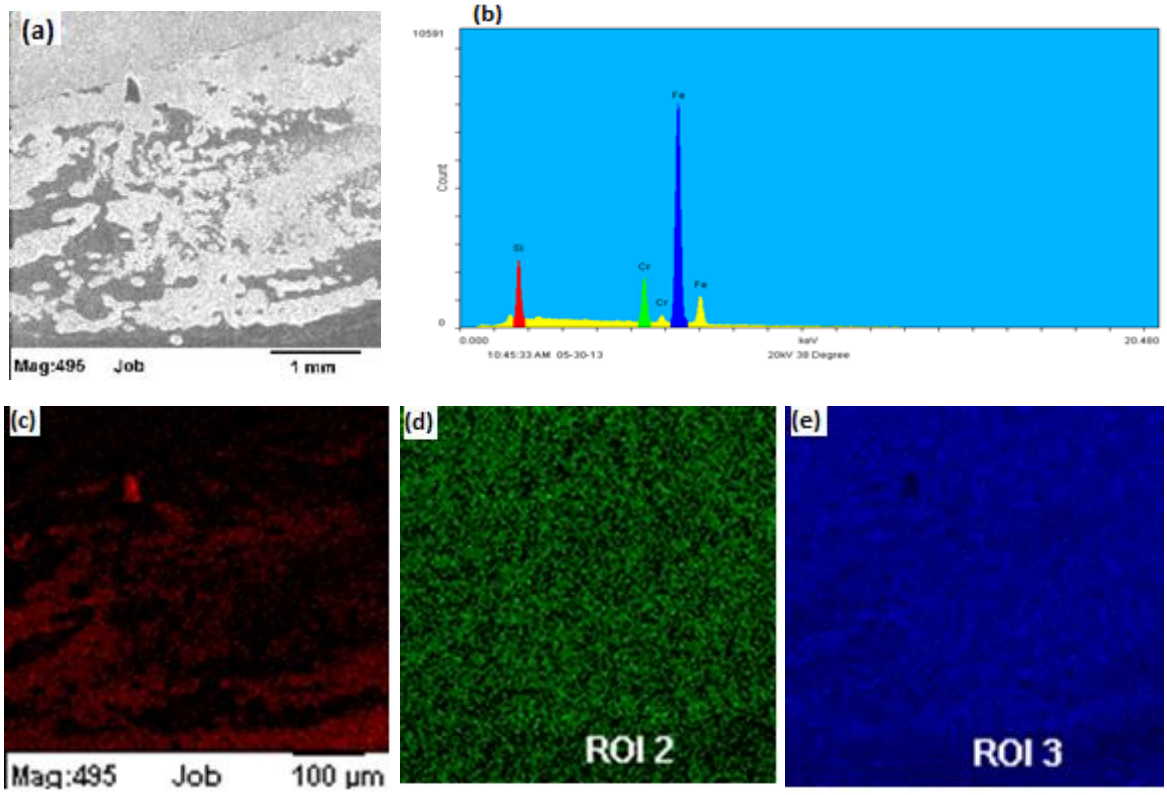

Figure 3.58 EDS analysis: (a) SEM image of a wear track of the sample sintered at 1100ºC for 10 min., (b) EDS counts of the elements on the wear track, (c) silicon mapping, (d) chromium mapping, and (e) iron mapping on the wear track.

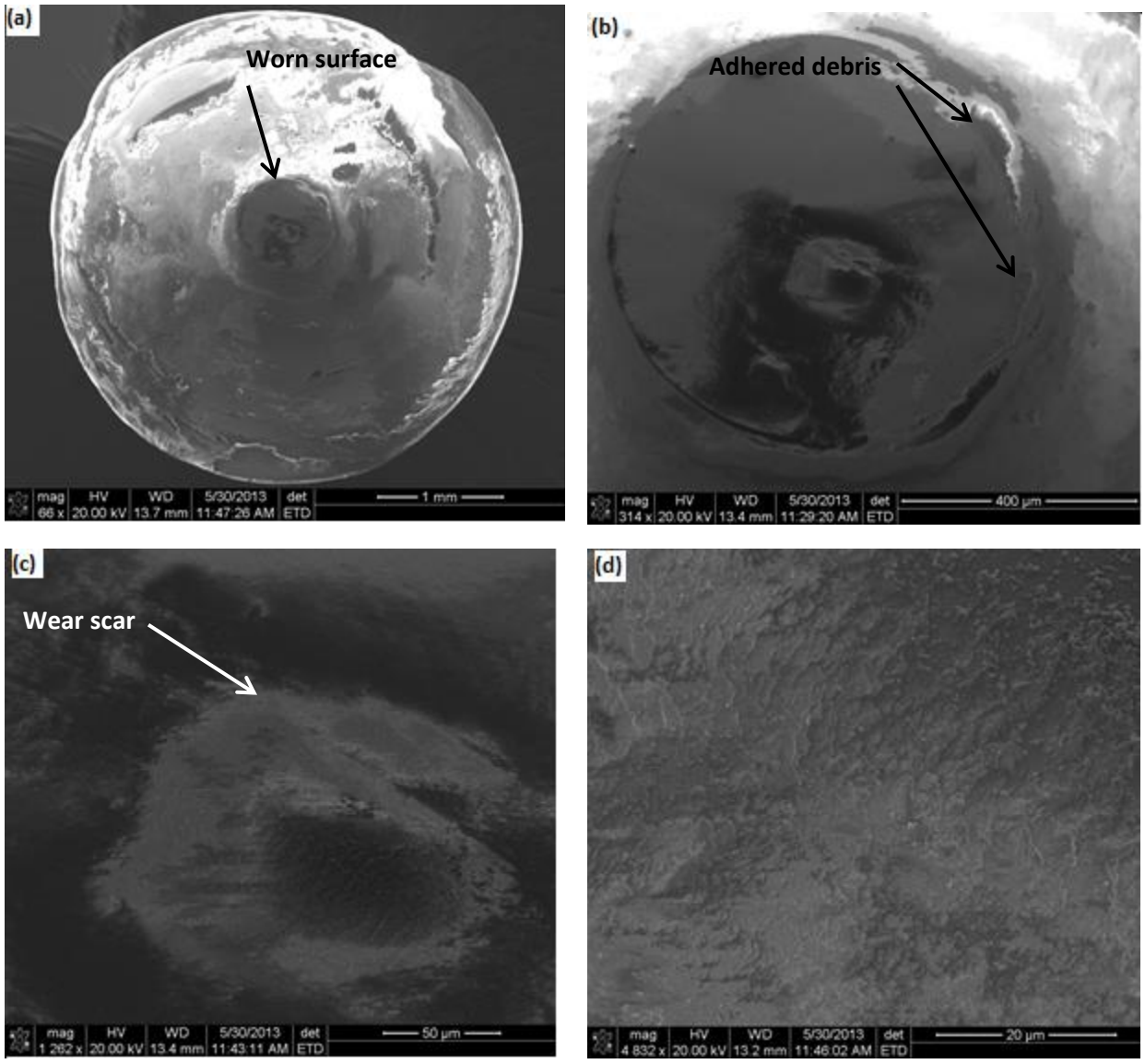

Figure 3.59 SEM images of worn surface of a silicon nitride ball with as-received steel plate at a 15N load.

Fig. 3.59 (a) shows the exact circular profile of the worn surface on the silicon nitride ball. The diameter of the scar is 729 μm. Fig. 3.59 (b) shows the debris adhered to the ball just outside the circumference of the worn surface. This debris is a mass of steel transferred during wear process on the ball. The elemental analysis of this wear debris is performed in Fig. 3.61. Fig. 3.61 (c) and (d) show the morphology of the wear scar. The scale-like features can be seen on the wear scar

indicative of the brittle transgranular fracture that has occurred on the silicon nitride ball. This type of fracture appearing on the ball is confirmed with the analysis performed by Gautier et al. [62]. Fig. 3.60 shows the possible wear mechanism on the silicon nitride ball for our parameters is transgranular fracture. For lower velocities the chemical reaction between steel and silicon nitride dominates the wear mechanism. At high and intermediate velocities the byproducts of the chemical reaction are thrown out of the wear track hence playing a negligible role in the wear mechanism. At high velocities at a high load the flash temperatures generated are large enough to carry out the phase transformation on the silicon nitride surface and cause wear.

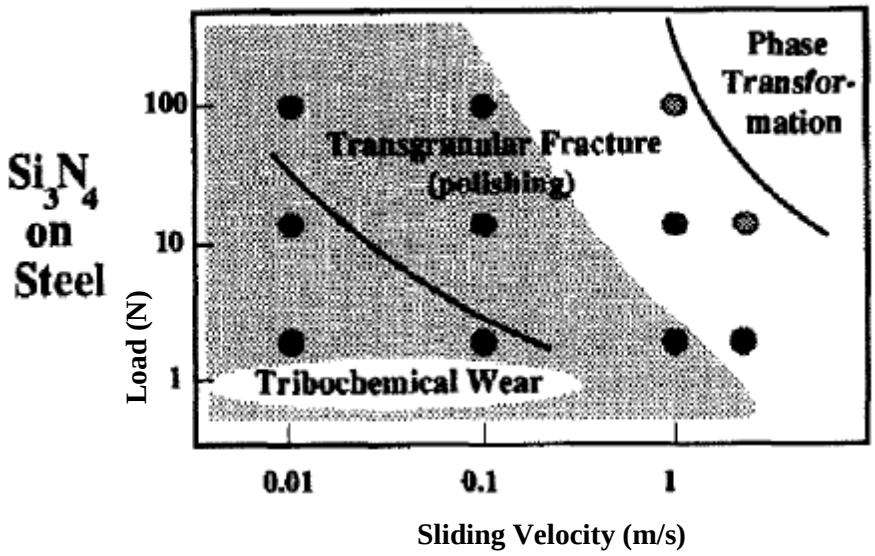

Figure 3.60 Load versus sliding velocity map for silicon nitride ball with steel (Reprinted from [62] with the permission of the publisher).

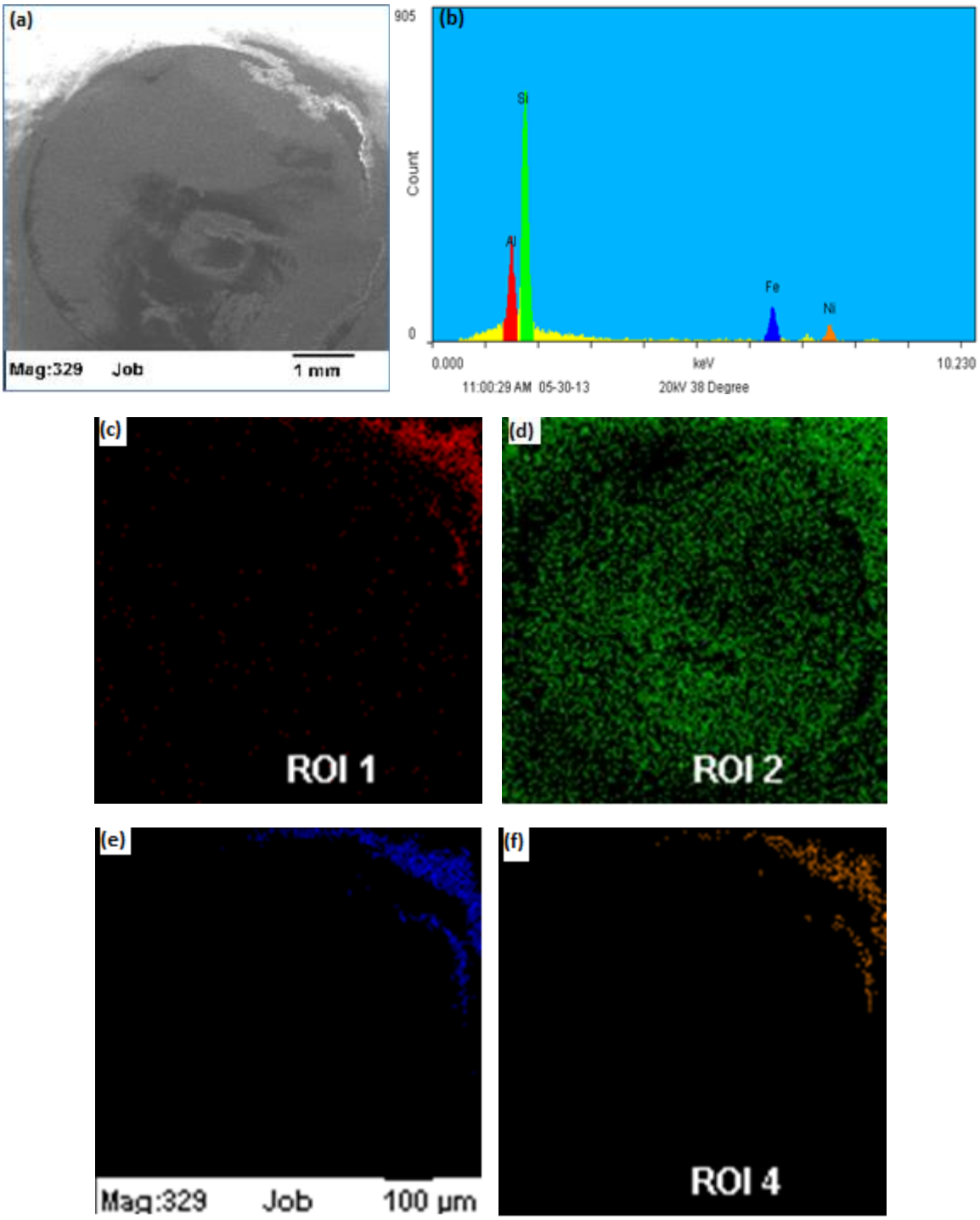

Figure 3.61 EDS analysis of silicon nitride ball with the sample 1100ºC for 10 min. at a 15 N load: (a) SEM image of a worn surface, (b) EDS elemental counts, (c) aluminum mapping, (d) silicon mapping, (e) iron mapping, and (f) nickel mapping.

Fig. 3.61 shows the presence of Fe, Al and Ni in the wear debris adhered to the silicon nitride ball. These elements are transferred from the steel sample on the ball during wearing. Al and Ni being the soft phases are predicted to be separated from the solid solution under the action of high temperature and load. Only Si is present on the wear scar confirming that no phase transformation or chemical reaction has occurred on the ball surface during the wear process. Hence the wearing mechanism of the silicon nitride ball is confirmed as a transgranular fracture. All the debris are present just outside the circumference of the wear track indicating that the sliding velocity is enough to push the debris out of the worn surface. No adhered mass is observed on the wear scar attributing to the retransfer of all the mass on the steel sample.

3.5.2.3 Wear rate

The wear rate of the steel samples slid with a silicon nitride ball is less when compared to the wear rate with an alumina ball. The reason for the low wear rate is the lower hardness of the silicon nitride ball (1668 HV) as compared to alumina ball (1914 HV). This phenomenon can also be supported by the formation of a tribolayer event occurring at the later stage of a wear process. Fig. 3.62 shows a comparison of the wear rate at different loads for each sample. The wear rate of the sintered samples is an order of magnitude less than the wear rate of an as-received steel plate. This is because of the high hardness of sintered samples. The sample sintered at 1100ºC for 10 min. shows the lowest wear rate of 0.4253×10^{-5} mm^3 /Nm for a 15 N load with the silicon nitride ball. No sharp increase in wear rate is observed at 15 N load for any sample. For the sample sintered at 1100ºC for 5 min. a decrease in wear rate can be observed at 10 N as compared to the wear rate at 5 N.

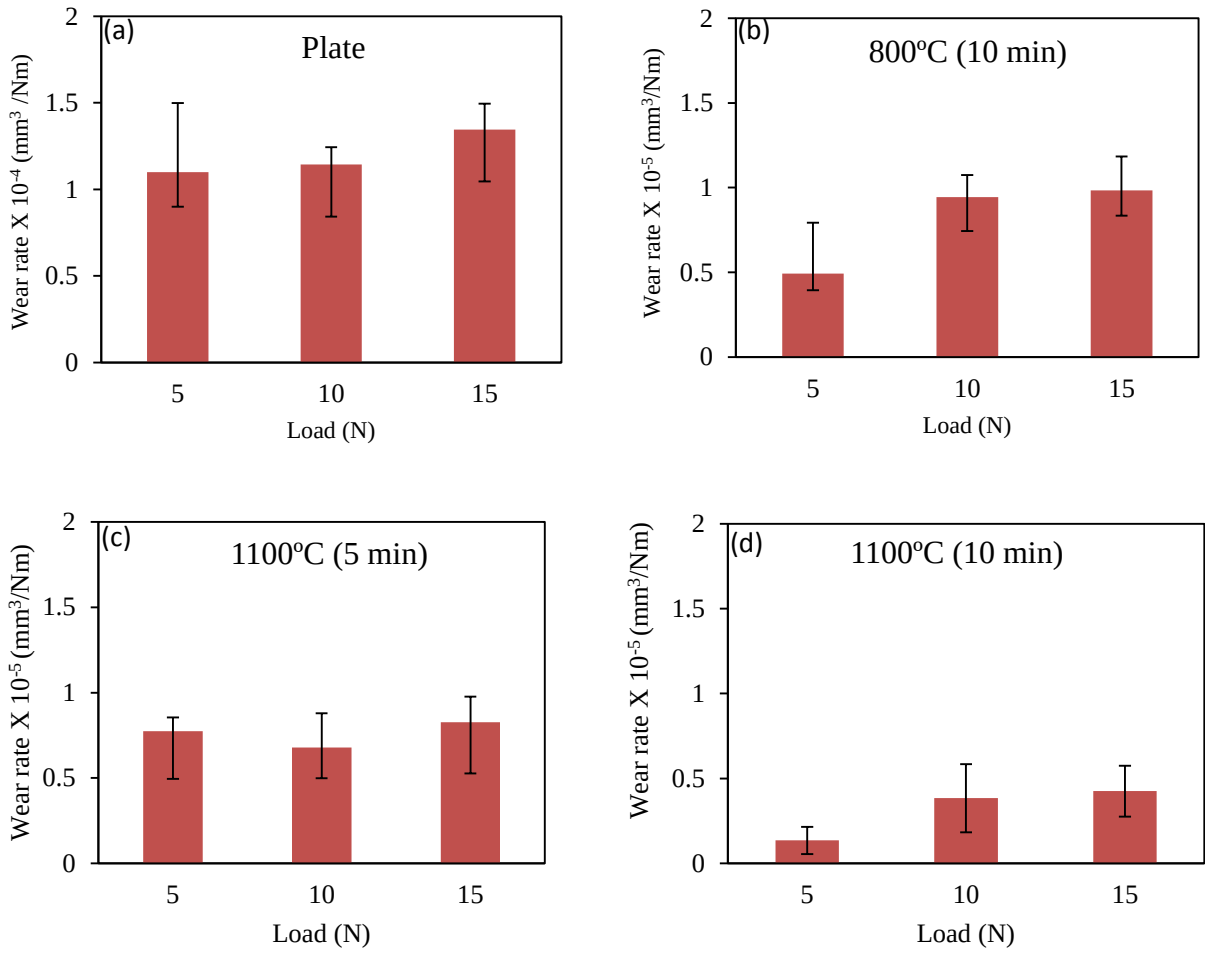

Figure 3.62 Wear rate comparison with load applied during wear for: (a) as-received plate, (b) sample sintered at 800ºC for 10 min., (c) sample sintered at 1100ºC for 5 min., and (d) sample sintered at 1100ºC for 10 min.

This can be attributed to the increase in the rate of formation of a tribolayer which has resulted in a decrease in the direct contact area of the ceramic ball and the steel plate. For all other samples the wear rate is observed increasing with the increase in load.

3.5.2.4 A comparison of a wear track profile

It can be observed that the groove of the wear track is deep as well as wide. The material removal process by an alumina ball appears to be uniform with no transfer of mass on the wear track. Fig. 3.66 shows the front view profile of the wear track on the same steel plate generated after sliding for 60 min. with the silicon nitride ball. The groove on the wear track is jagged. The depth of the wear track is less when compared with the alumina wear track. The width also appears to be smaller.

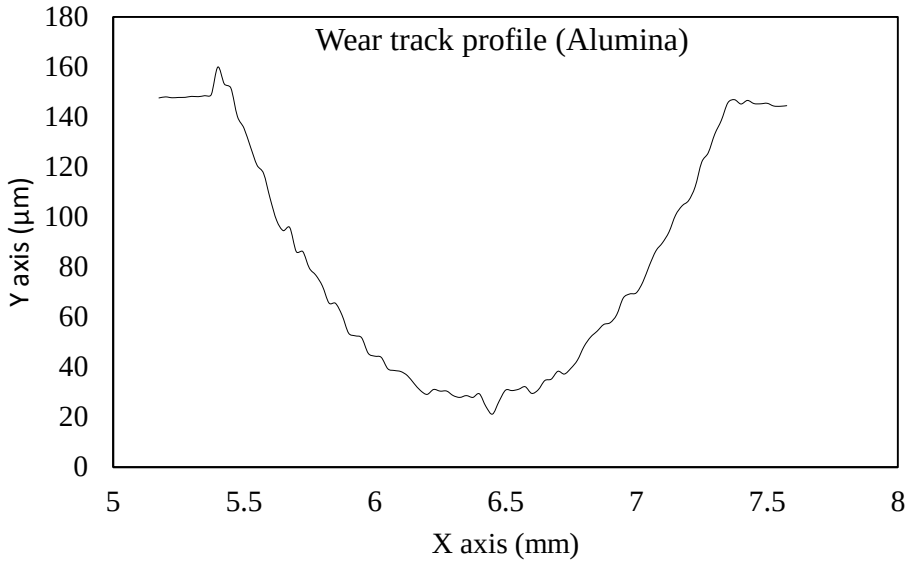

Figure 3.63 Front view of the wear track profile of the steel plate after 60 min. of sliding with alumina ball at a 10 N load.

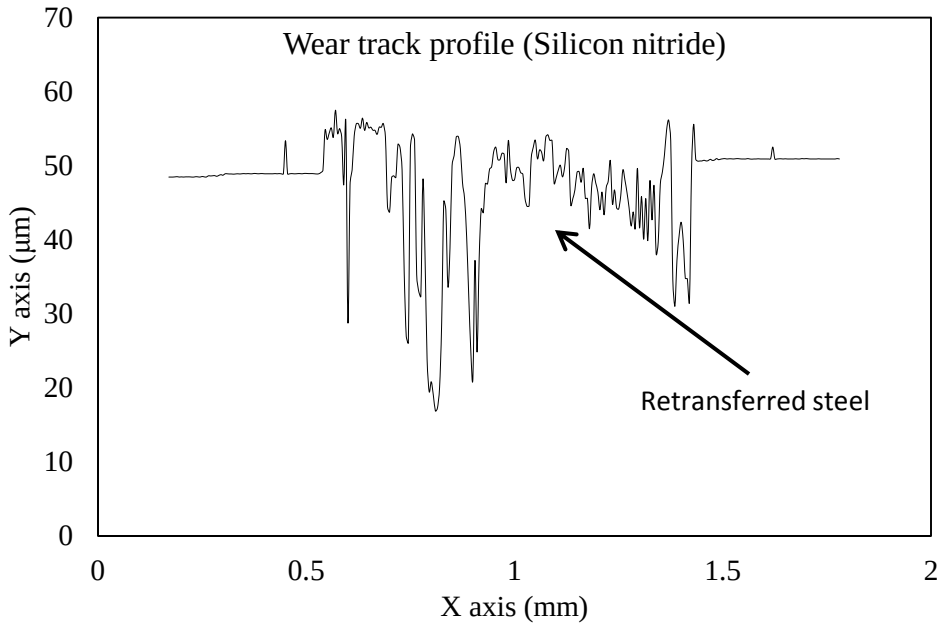

Figure 3.64 Front view of the wear track profile of the steel plate after 60 min. of sliding with the silicon nitride ball at a 10 N load.

This comparison of the geometry of the wear track justifies the lower values of the wear rate observed due to the sliding of the steel with the silicon nitride ball.

CHAPTER IV

CONCLUSIONS

- The present work demonstrated the processing of nanostructured modified 9Cr-1Mo steel using ball milling of normalized-tempered steel plate and subsequent SPS of milled powder. Ball milling resulted in the production of nanocrystalline powder of modified 9Cr-1Mo steel. No phase transformation was observed up to 6 h of ball milling.
- Spark plasma sintering was able to retain submicron grain size in bulk samples sintered at 500ºC, 800ºC, and 1100ºC for 5 min. and 10 min. The relative density of the spark plasma sintered samples is observed to be dependent on sintering temperature and holding time. The relative density of > 97% was achieved for the samples sintered at 1100°C.
- Microhardness of the sintered samples increases with the increase in relative density and the decrease in mean grain size. The sample sintered at 1100°C for 10 min. showed the highest microhardness about 635 HV. The hardness is improved by 200% as compared to the as-received modified 9Cr-1Mo steel plate.
- Modified 9Cr-1Mo steel undergoes severe abrasive wear with alumina ball. The wear is uniform and no retransfer of mass back to the sample is observed. The wear mechanism with silicon nitride ball is complicated and involves formation of a ‘Fe-Si-Cr’ tribolayer on the wear track. The samples sintered at 500°C show higher weight loss in wear as

compared to the as-received plate. For the samples sintered at 800°C and 1100°C, an order of magnitude decrease in the wear rate is achieved as compared to the as-received modified 9Cr-1Mo plate.

CHAPTER V

FUTURE WORK

- Oxide dispersion strengthening of modified 9Cr-1Mo steel with yttrium oxide (Y_2O_3) via ball milling.
- High temperature wear testing of spark plasma sintered samples to simulate the working environment conditions.
- Wear testing in the presence of lubrication that will take into account the corrosion of steel.
- Study of machinability of spark plasma sintered samples into the shapes required for application.

REFERENCES

1. L. Kahlman and I.M. Hutchings, Effect of Particulate Contamination in Grease-Lubricated Hybrid Rolling bearings. Tribology transactions, 1999. **42** (4): p. 842- 850.
2. B. Bhushan and L.B. Sibley, Silicon Nitride Rolling Bearings for Extreme Operating Conditions. ASLE transactions, 1981. **25**: p. 417- 428.
3. R. N. Katz and J.G. Hannoosh, Ceramics for High Performance Rolling Element Bearings: A Review and Assessment. International journal of high tech ceramics, 1985. **1**: p. 69- 79.
4. B.B. Bartha, J. Zawadzki, S. Chandrasekar, and T.N. Farris, Wear of Hard-Turned AISI 52100 Steel. Metallurgical And Materials Transactions A, 2005. **36A**: p. 1417- 1425.
5. L. Zhou, G.L., Z. Han, K. Lu, Grain size effect on wear resistance of a nanostructured AISI52100 steel. Scripta materialia, 2008 **58**: p. 445- 448.
6. Technical information Bearing Materials, AST Bearings.
7. X.Y. Wang and D.Y. Li, Mechanical, electrochemical and tribological properties of nano-crystalline surface of 304 stainless steel. Wear, 2003. **255**: p. 836- 845.
8. H. Dong and T. Bell, Tribological behavior of alumina sliding against Ti6A14V unlubricated contact. Wear, 1999. **225-229**: p. 874- 884.
9. Gahr, K.H.Z., Sliding wear of ceramic- ceramic, ceramic- steel and steel- steel pairs in lubricated and unlubricated contact. Wear 1989. **133**: p. 1- 22.
10. C. X. Li and T. Bell, Sliding wear properties of active screen plasma nitrided 316 austenitic stainless steel. Wear, 2004. **256**: p. 1144- 1152.
11. N. Hansen, Hall–Petch relation and boundary strengthening. Scripta materialia, 2004. **51**: p. 801-806.
12. T.D. Shen, R.B.S., S. Feng, J.G. Swadener, J.Y. Huang, M. Tang, J. Zhang, S.C. Vogel, Y. Zhao, Effect of solute segregation on the strength of nanocrystalline alloys: Inverse Hall–Petch relation. Acta Materialia, 2007. **55**: p. 5007-5013.
13. D.A. McClintock, M.A.S., D.T. Hoelzer, R.K. Nanstad, Mechanical properties of irradiated ODS-EUROFER and nanocluster strengthened 14YWT. Journal of Nuclear Materials, 2009. **392**(353-359).
14. S. Ukai, M.H., H. Okada, M. Inoue, T. Nishida, M. Fujiwara, Alloying design of oxide dispersion strengthened ferritic steel for long life FBRs core materials. Journal of Nuclear Materials, 1993. **204**: p. 65-73.
15. Ni Hong-wei, H.H., Li Guang-qiang , Liu Jing, Preparation of Nanocrystalline 430L Stainless Steel by HEBM and SPS. Journal of iron and steel research, international, 2008. **15**(4): p. 73-76.
16. A. Czyrska-Filemonowicz, A.Z.-L., P.J. Ennis Modified 9% Cr steels for advanced power generation: microstructure and properties. Journal of Achievements in Materials and Manufacturing Engineering, 2006. **19**(2): p. 43-48.

17. Pantip Ampornrat, G.S.W., Oxidation of ferritic–martensitic alloys T91, HCM12A and HT-9 in supercritical water. Jounal of Nuclear Materials, 2007. **371**: p. 1-17.
18. G. Gupta, B. Alexandreanu, and G.S. Was, Grain boundary engineering of ferritic-martensitis alloy T91. Metallurgical and Materials Transactions, 2004. **35A**(2).
19. Dalikova, K., Study of liquid metal embrittlement sensitivity of t91 in stagnant pb. 2009.
20. V. B. Singh and A. Gupta, Microstructure and corrosion studies of 9Cr- 1Mo steel in acidic methanol solutions. Indian journal of chemical technology, 2005. **12**: p. 347-355.
21. O.P. Modi, M.N.M., K.P.Singh, Potentiodynamic study of modified 9Cr- 1Mo ferritic steel in sulphuric acid and sea water. Corrosion Science, 1990. **30**: p. 941-947.
22. L. Falat, M. Svoboda, A. Výrostková, I. Petryshynets, and M. Sopko, Microstructure and creep characteristics of dissimilar T91/TP316H martensitic/austenitic welded joint with Ni-based weld metal. Materials Characterization, 2012. **72**: p. 15-23.
23. S. Ukai, Microstructure and High-Temperature Strength of 9CrODS Ferritic Steel. Metal, Ceramic and Polymeric Composites for Various Uses.
24. C. Heintze, M. Hernández-Mayoral, A. Ulbricht, F. Bergner, et al., Nanoscale characterization of ODS Fe–9%Cr model alloys compacted by spark plasma sintering. Journal of Nuclear Materials, 2012. **428**: p. 139-146.
25. S. Saroja, A. Dasgupta, R. Divakar, S. Raju, et al., Development and characterization of advanced 9Cr ferritic/martensitic steels for fission and fusion reactors. Journal of Nuclear Materials, 2011. **409**: p. 131-139.
26. Z.Q. Fan, T. Hao, S.X. Zhao, G.N. Luo, et al., The microstructure and mechanical properties of T91 steel processed by ECAP at room temperature. Journal of Nuclear Materials, 2013. **434**: p. 417-421.
27. Y. Li, B. Zhou, T. Feng, and J. Ren, Microsturcture and fracture morphology in the welding zone of T91 heat-resisting steel used in power station. Journal of Materials Science and Technology, 2002. **18**(5): p. 427-430.
28. S. Saroja, P.P., M. Vijayalakshmi, V. S. Raghunathan, Prediction of microstructural states in Cr-Mo Steels using phase evolution diagrams. Acta Metallurgica, 1994. **43**(8): p. 2985-3000.
29. K. Lu and J. Lu, Nanostructured surface layer on metallic materials induced by surface mechanical attrition treatment. Materials Science and Engineering, 2004. **A**(375-377): p. 38-45.
30. Y. Lin, J.L., L. Wang, T. Xu, Q. Xue, Surface nanocrystallization by surface mechanical attrition treatment and its effect on structure and properties of plasma nitrided AISI 321 stainless steel. Acta Materialia, 2006. **54**: p. 5599-5605.
31. Y. Iwahashi, Z. Horita, M. Nemoto, and T. Langdon, The process of grain refinement in equal channel angular pressing. Acta Metallurgica, 1998. **46**(9): p. 3317-3331.
32. C.X. Huang, Y.L.G., G. Yang, S.D. Wua, G.Y. Lia, S.X. Lia, Bulk nanocrystalline stainless steel fabricated by equal channel angular pressing. Journal of materials Research, 2006. **21**(7): p. 1687-1692.
33. H. Q. Bing, L. J. Enrique, and M.A. Farghalli, Mechanical properties of iron processed by severe plastic deformation. Metallurgical and Materials Transactions, 2003. **34**(1): p. 71-83.
34. Foley, D.C., Ferritic-martensitic steel subjected to equal channel angular extrusion, in *Mechanical Engineering*December 2007, Texas A&M.
35. Gleiter, H., Nanocrystalline materials. Progress in materials science, 1989. **33**(4): p. 223-315.
36. A.Djekoun, N.B., A.Chebli, A.Otmani, M.Benabdeslem, B.Bouzabata, J.M.Greneche, Characterization of Fe and Fe50Ni50 ultrafine nanoparticles synthesized by inert gas-condensation method. Physica B, 2009. **404**: p. 3824-3829.
37. I. E. Anderson, R.S.F., H. Morton, Flow mechanisms in high pressure gas atomization. Materials Science and Engineering, 1991. **A**(148): p. 101-114.

38. Y. Min, S. Chang-jiang, D. Yong-xiang, Z. Liang, et al., Microstructure evolution of gas atomized Fe-25Cr-3.2C alloy powders. Journal of Iron and steel research, 2011. **18**(2): p. 75-78.
39. McClintock, D.A., Mechanical Properties of an Irradiated Nanocluster Strengthened High-Chromium Ferritic Alloy, 2008, University of Texas at Austin.
40. Z. Oksiuta, P.O., Y. de Carlan, N. Baluc Development and characterisation of a new ODS ferritic steel for fusion reactor application. Jounal of Nuclear Materials, 2009. **393**: p. 114-119.
41. Stern, M., Method for treating aluminum or aluminum alloy scrap, U.p. office, Editor 1945: United States.
42. M. H. Enayati, M.R.B., S. Nosohian, Ball milling of stainless steel scrap chips to produce nanocrystalline powder. Journal of Materials Science, 2007. **42**: p. 2844-2888.
43. C. Suryanarayana, Mechanical alloying and milling. Progress in Materials Science, 2001. **46**: p. 1-184.
44. Kuhrt C, S.H., Schultz L, Artz E, Mechanical alloying for structural applications, ed. d. J.J.1993, Materials Park, OH: ASM International.
45. A. Ramar, Z.O., N. Baluc, R. Schäublin, Effect of mechanical alloying on the mechanical and microstructural properties of ODS EUROFER 97. Fusion Engineering and Design, 2007. **82**(15-24): p. 2543-2549.
46. S. Ukai, Microstructure and High-Temperature Strength of 9CrODS Ferritic Steel. Metal, Ceramic and Polymeric Composites for Various Uses, 2005.
47. F.B. Swinkles, D.S. Wilkinson, E. Artz, and M.F. Ashby, Mechanisms of hot-isostatic pressing. Acta Metallurgica, 1983. **31**(11): p. 1829-1840.
48. A.S. Helle, K. E. Easterling, and M.F. Ashby, Hot isostatic pressing diagrams: New developments. Acta Metallurgica, 1985. **33**(12): p. 2163-2174.
49. Tokita, M. *Mechanism of spark plasma sintering*.
50. Z. A. Munir, U.A.-T., M. Ohyanagi, The effect of electric field and pressure on the synthesis and consolidation of materials: A review of the spark plasma sintering method. Journal of Materials Science, 2006. **41**: p. 763-777.
51. J. E. Alanis, J.R.M., J. E. Garay, The current activated pressure assisted densification technique for producing nanocrystalline materials. JOM, Nanocomposite materials, 2010. **62**(2): p. 58-62.
52. R. B. Schwarz, P. Kasiraj, T. Vreeland Jr, and T.J. Ahrens, A theory for the shock wave consolidation of powders. Acta Metallurgica, 1984. **32**(8): p. 1243-1252.
53. N. M. Chikhradze, C. Politis, M. Chikhradze, and G. Oniashvili, Bulk nanostructured materials obtained by shock waves compaction of titanium and aluminum, in *2nd International Conference on Ultrafine Grained & Nanostructured Materials (UFGNSM)*2012, World Scientific Publishing Company.
54. Noé Alba-Baena, W.S., L. E. Murr, Shock-Wave-Compaction (SWC) of Al/CNT Two Phase Systems, in *Carbon nanotubes*2010, InTech: Jose Mauricio Marulanda.
55. Garay, J.E., Current activated, pressure assisted densification of materials. The Annual Review of Materials Research, 2010. **40** p. 445-468.
56. W. Chen, U. Anselmi-Tamburini, J.E. Garay, J.R. Groza, and Z.A. Munir, Fundamental investigations on the spark plasma sintering/synthesis process: I. Effect of dc pulsing on reactivity. Materials Science and Engineering, 2005. **A**(394): p. 132-138.
57. U. Anselmi-Tamburini, S. Gennari, J.E. Garaya, and Z.A. Munir, Fundamental investigations on the spark plasma sintering synthesis process II. Modeling of current and temperature distributions. Materials Science and Engineering, 2005. **A**(394): p. 139-148.
58. S. Spigarelli, E. Cerri, P. Bianchi, and E. Evangelista, Interpretation of creep behaviour of a 9Cr–Mo–Nb–V–N (T91) steel using threshold stress concept. Materials Science and Technology, 1999. **15**: p. 1433-1440.

59. H. Sakasegawa, T. Hirose, A. Kohyama, Y. Katoh, et al., Effects of precipitation morphology on toughness of reduced activation ferritic/ martensitic steels. Journal of Nuclear Materials, 2002. **307-311**: p. 490-494.
60. Z. Guo, K.G. Keong, and W. Sha, Crystallisation and phase transformation behaviour of electroless nickel phosphorus platings during continuous heating. Journal of Alloys and Compounds, 2003. **358**: p. 112-119.
61. H.W. Zhang, R. Gopalan, T. Mukai, and K. Hono, Fabrication of bulk nanocrystalline Fe–C alloy by spark plasma sintering of mechanically milled powder. Scripta materialia, 2005. **53**: p. 863-868.
62. P. Gautier, K.K., Wear mechanisms of silicon nitride, partially stabilized zirconia and alumina in unlubricated sliding against steel. Wear, 1993. **162-164**: p. 305-313.
63. K.K. AjithKumar, U.T.S.Pillai, B.C.Pai, and M.Chakraborty, Dry sliding wear behaviour of Mg–Si alloys. Wear, 2013. **303**: p. 56-64.
64. M. A. Chowdhury, M. K. Khalil, D. M. Nuruzzaman, and M.L. Rahaman, The effect of normal load and sliding speed on wear property of aluminum. International Journal of Mechanical & Mechatronics Engineering, 2012. **11**(45-49).
65. S.K. Karak, C.S.V., Z. Witczak,W. Lojkowski, J. D. Majumdar, I. Manna, Studies on wear behavior of nano-Y2O3 dispersed ferritic steel developed by mechanical alloying and hot isostatic pressing. Wear, 2010. **270**: p. 5-11.
66. Kalin, M., Wear mechanisms in oil- lubricated and dry fretting of silicon nitride against steel. Wear, 1997. **210**: p. 27- 38.

VITA

Aditya Deepak Dekhane

Candidate for the Degree of

Master of Science

Thesis: WEAR BEHAVIOR OF SPARK PLASMA SINTERED NANOSTRUCTURED MODIFIED 9Cr-1Mo STEEL

Major Field: Mechanical and Aerospace Engineering.

Biographical: Born on December 14th 1988, in Bhusawal, Maharashtra, India to Mr. Deepak Dekhane and Mrs. Charusheela Dekhane.

Education: Completed the requirements for the Master of Science inMechanical Engineering at Oklahoma State University, Stillwater, Oklahoma in July, 2013.

Completed the requirements for the Bachelor of Science in Mechanical Engineering at Pune University, Pune, Maharashtra, India in 2010.

Experience: Graduate Teaching Assistant
Course: Materials Science
Department of Mechanical and Aerospace Engineering, Oklahoma State University, OK

Graduate Engineer Trainee (Research and Development)
Danaher Portescap, Mumbai, India.

Professional Memberships: American Society of Mechanical Engineers (ASME).